UNITED NATIONS EDUCATIONAL, SCIENTIFIC AND CULTURAL ORGANIZATION
INTERNATIONAL ATOMIC ENERGY AGENCY
INTERNATIONAL CENTRE FOR THEORETICAL PHYSICS
I.C.T.P., P.O. BOX 586, 34100 TRIESTE, ITALY, CABLE: CENTRATOM TRIESTE

H4.SMR/1058-5

WINTER COLLEGE ON OPTICS

9 - 27 February 1998

Interferometry and Optical Shop Testing

D. Malacara

Centro de Investigaciones en Optica, León, México

HANDBOOK OF OPTICS

Volume II
Devices, Measurements, and Properties

Second Edition

Sponsored by the OPTICAL SOCIETY OF AMERICA

Michael Bass Editor in Chief

The Center for Research and Education in Optics and Lasers (CREOL)
University of Central Florida
Orlando, Florida

Eric W. Van Stryland Associate Editor

The Center for Research and Education in Optics and Lasers (CREOL)
University of Central Florida
Orlando, Florida

David R. Williams Associate Editor

Center for Visual Science
University of Rochester
Rochester, New York

William L. Wolfe Associate Editor

Optical Sciences Center
University of Arizona
Tucson, Arizona

McGRAW-HILL, INC.

New York San Francisco Washington, D.C. Auckland Bogotá
Caracas Lisbon London Madrid Mexico City Milan
Montreal New Delhi San Juan Singapore
Sydney Tokyo Toronto

CHAPTER 30
OPTICAL TESTING

Daniel Malacara
Centro de Investigaciones en Optica, A.C.
León, Gto, Mexico

30.1 GLOSSARY

$\mathbf{E}$	electric field strength
k	radian wave number
r	position
t	time
λ	wavelength
ϕ	phase
ω	radian frequency

30.2 INTRODUCTION

The requirements for high-quality optical surfaces are more demanding every day. Thus, they should be tested in an easier, faster, and more accurate manner. Optical surfaces usually have a flat or a spherical shape, but they also may be toroidal or generally aspheric. Frequently, an aspherical surface is a conic of revolution. An aspherical surface can only be made as good as it can be tested. Here, the field of optical testing will be reviewed. There are some references that the reader may consult for further details (Malacara, 1991).

30.3 CLASSICAL NONINTERFEROMETRIC TESTS

Some classical tests will never be obsolete, because they are cheap, simple, and provide almost instantly qualitative results about the shape of the optical surface or wavefront. These are the Foucault or knife-edge test, the Ronchi test, and the Hartmann test. They will be described next.

Foucault Test

The Foucault or knife-edge test was invented by Leon Foucault (1852) in France, to evaluate the quality of spherical surfaces. This test detects the presence of transverse aberrations by intercepting the reflected rays deviated from their ideal trajectory, as Fig. 1 shows. The observer is behind the knife, looking at the illuminated optical surface, with

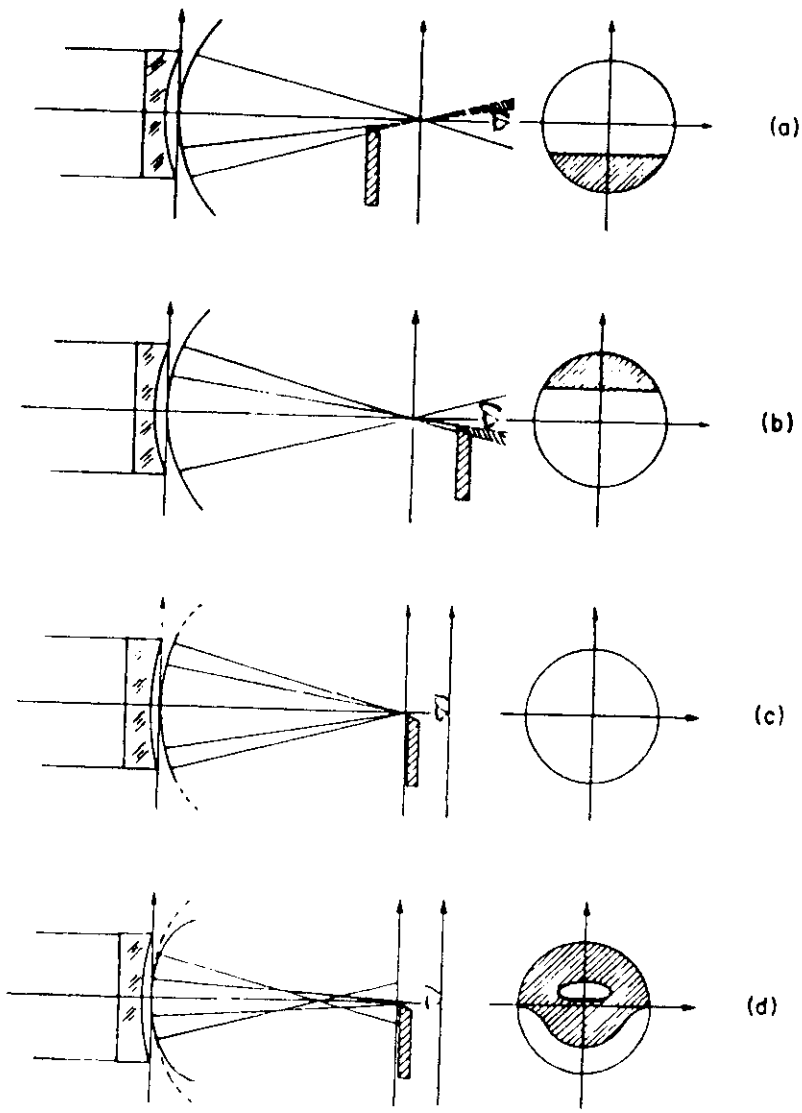

FIGURE 1 Optical schematics for the Foucault test of a spherical mirror, at several positions of the knife edge.

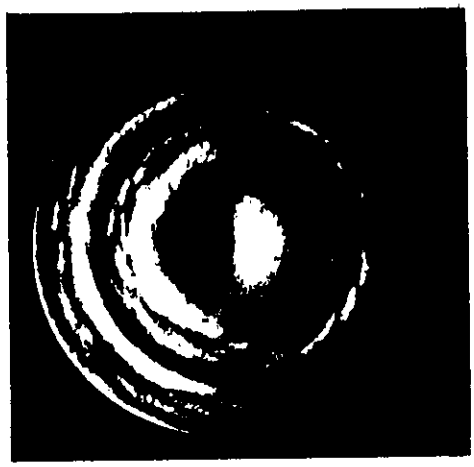

FIGURE 2 An optical surface being examined by the Foucault test. (*From Ojeda-Castañeda, 1978*.)

the reflected rays entering the eye. The regions corresponding to the intercepted rays will appear dark, as in Fig. 2.

This test is extremely sensitive. If the wavefront is nearly spherical, irregularities as small as a fraction of the wavelength of the light may be easily detected. This is the simplest and most powerful qualitative test for observing small irregularities and evaluating the general smoothness of the spherical surface under test. Any other surface or lens may be tested, as long as it produces an almost spherical wavefront, otherwise, an aberration compensator must be used, as will be described later. Very often a razor blade makes a good, straight, sharp edge that is large enough to cover the focal region.

Ronchi Test

Vasco Ronchi (1923) invented his famous test in Italy in 1923. A coarse ruling (50–100 lines per inch) is placed in the convergent light beam reflected from the surface under test, near its focus. The observer is behind the ruling, as Fig. 3 shows, with the light entering the eye. The dark bands in the ruling intercept light, forming shadows on the illuminated optical surface. These shadows will be straight and parallel only if the reflected wavefront is perfectly spherical. Otherwise, the fringes will be curves whose shape and separation depends on the wavefront deformations. The Ronchi test measures the transverse aberrations in the direction perpendicular to the slits on the grating. The wavefront deformations $W(x, y)$ are related to the transverse aberrations $\mathrm{TA}_x(x, y)$ and $\mathrm{TA}_y(x, y)$ by the following well-known relations:

$$\mathrm{TA}_x(x, y) = -r\frac{\partial W(x, y)}{\partial x} \tag{1}$$

and

$$\mathrm{TA}_y(x, y) = -r\frac{\partial W(x, y)}{\partial y} \tag{2}$$

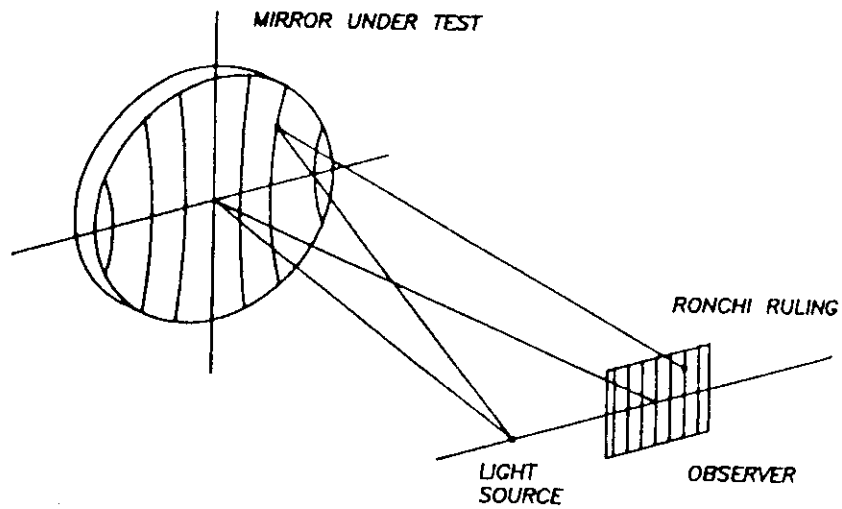

FIGURE 3 Testing a concave surface by means of the Ronchi test.

where r is the radius of curvature of the wavefront $W(x, y)$. Thus, if we assume a ruling with period d, the expression describing the mth fringe on the optical surface is given by

$$\frac{\partial W(x, y)}{\partial x} = -\frac{md}{r} \tag{3}$$

Each type of aberration wavefront has a characteristic Ronchi pattern, as shown in Fig. 4; thus, the aberrations in the optical system may be easily identified, and their magnitude estimated. We may interpret the Ronchi fringes not only as geometrical shadows, but also as interferometric fringes, identical with those produced by a lateral shear interferometer.

Hartmann Test

J. Hartmann (1900) invented his test in Germany. It is one of the most powerful methods to determine the figure of a concave spherical or aspherical mirror. Figure 5 shows the optical configuration used in this test, where a point light source illuminates the optical surface, with its Hartmann screen in front of it. The light beams reflected through each hole on the screen are intercepted on a photographic plate near the focus. Then, the position of the recorded spots is measured to find the value of the transverse aberration on each point. If the screen has a rectangular array of holes, the typical Hartmann plate image for a parabolic mirror looks like that in Fig. 6. The wavefront $W(x, y)$ may be obtained from integration of Eqs. (1) and (2) as follows:

$$W(x, y) = -\frac{1}{r}\int_0^x \mathrm{TA}_x(x, y)\, dx \tag{4}$$

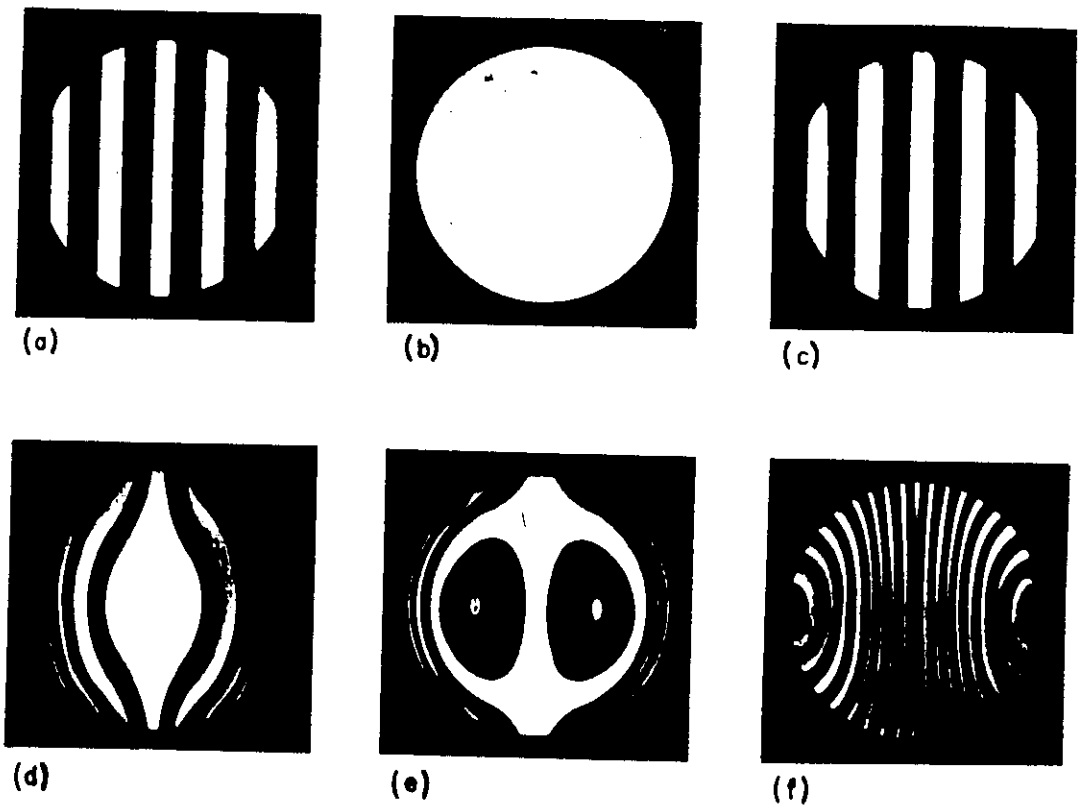

FIGURE 4 Typical Ronchi patterns for a spherical and a parabolic mirror for different positions of the Ronchi ruling.

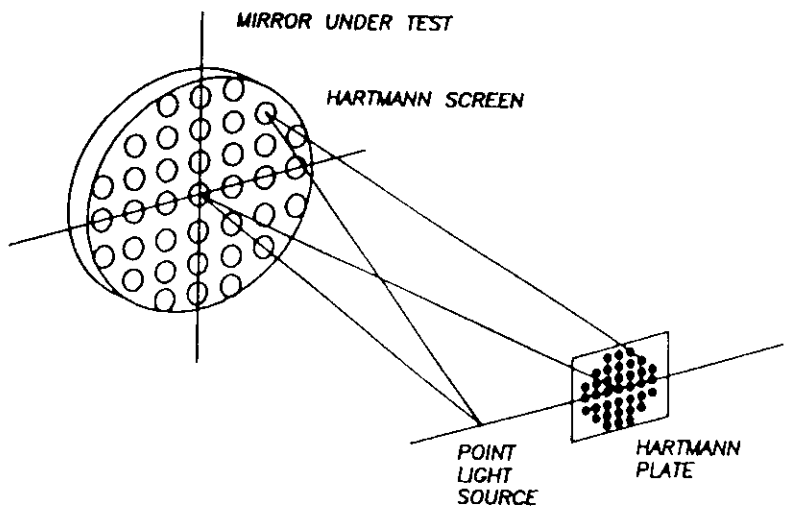

FIGURE 5 Optical arrangement to perform the Hartmann test.

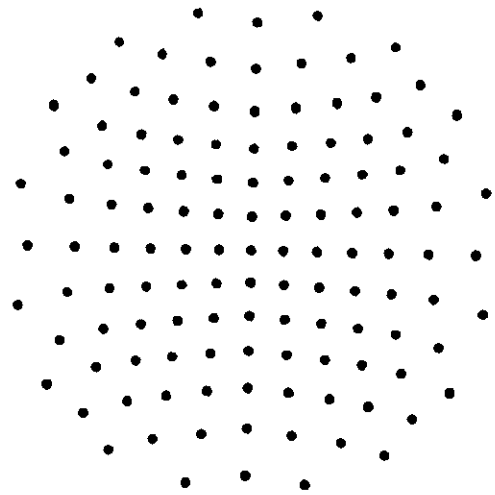

FIGURE 6 Array of spots in a Hartmann plate of a parabolic mirror.

and

$$W(x, y) = -\frac{1}{r}\int_0^r T\Delta_y(x, y)\, dy \tag{5}$$

After numerical integration of the values of the transverse aberrations, this test provides the concave surface shape with very high accuracy. If the surface is not spherical, the transverse aberrations to be integrated are the difference between the measured values and the ideal values for a perfect surface. Extended, localized errors, as well as asymmetric errors like astigmatism, are detected with this test. The two main problems of this test are that small, localized defects are not detected if they are not covered by the holes on the screen. Not only is this information lost, but the integration results will be false if the localized errors are large. The second important problem of the Hartmann test is that it is very time consuming, due to the time used in measuring all the data points on the Hartmann plate. These problems are avoided by complementing this test with the Foucault test, using an Offner compensator, in order to be sure about the smoothness of the surface (discussed under "Measuring Aspherical Wavefronts"). Various stratagems are available to speed the process. These include modulating the light at different frequencies at each of the holes. Variations also include measuring in front of, behind, or at the focus to get slope information. This technique can be considered an experimental ray trace.

30.4 INTERFEROMETRIC TESTS

Classical geometrical tests are very simple, but they do not provide the accuracy of the interferometric tests. Quite generally, an interferometric test produces an interferogram by producing the interference between two wavefronts. One of these two wavefronts is the

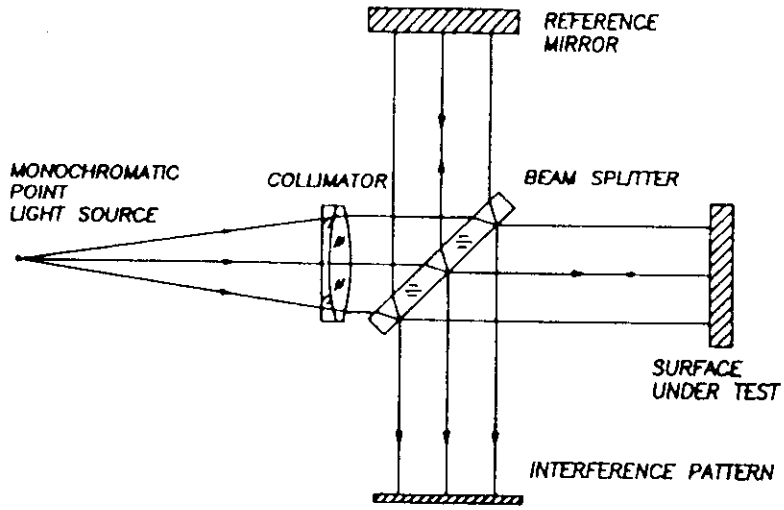

FIGURE 7 Twyman-Green interferometer.

wavefront under test. The other wavefront is either a perfectly spherical or flat wavefront, or a copy of the wavefront under test.

Interferometers with a Reference Wavefront

When the second wavefront is perfectly spherical or flat, this wavefront acts as a reference. The separation between the two wavefronts, or optical path difference OPD(x, y), is a direct indication of the deformations $W(x, y)$ of the wavefront under test. Then, we may simply write $W(x, y) = \text{OPD}(x, y)$. There are many types of interferometers producing interferograms of these types, for example, the Twyman-Green, Newton, Fizeau, Point Diffraction, Burch interferometers, and many others that will not be described. Two of these interferometers are in Figs. 7 and 8. Figure 9 shows some typical interferograms made with these interferometers (Malacara, 1991).

Shearing Interferometers

When the second wavefront is not perfectly flat or spherical, but a copy of the wavefront under test, its relative dimensions or orientation must be changed (sheared) in some way with respect to the wavefront under test. Otherwise, no information about the wavefront deformations is obtained, because the fringes will always be straight and parallel independent of any aberrations. There are several kinds of shearing interferometers, depending on the kind of transformation applied to the reference wavefront.

The most popular of these instruments is the lateral shearing interferometer, with the reference wavefront laterally displaced with respect to the other, as Fig. 10 shows. The optical path difference OPD(x, y) and the wavefront deformations $W(x, y)$ are related by

$$\text{OPD}(x, y) = W(x, y) - W(x - S, y) \tag{6}$$

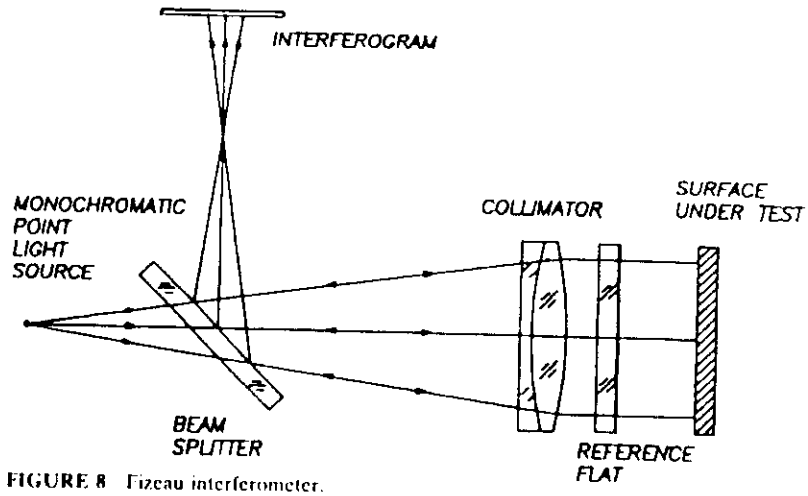

FIGURE 8 Fizeau interferometer.

where S is the lateral shear of one wavefront with respect to the other. If the shear is small with respect to the diameter of the wavefront, this expression may be approximated by

$$\mathrm{OPD}(x, y) = -S\frac{\partial W(x, y)}{\partial x} = -\frac{S}{r}\mathrm{TA}_x(x, y) \tag{7}$$

This relation suggests that the parameter being directly measured is the slope in the x direction of the wavefront (x component TA, of the transverse aberration). An example of a lateral shear interferometer is the Murty interferometer, illustrated in Fig. 11.

There are also radial, rotational, and reversal shearing interferometers, where the interfering wavefronts are as Fig. 12 shows. A radial shear interferometer with a large shear approaches an interferometer with a perfect reference wavefront.

30.5 INCREASING THE SENSITIVITY OF INTERFEROMETERS

The sensitivity of interferometers is a small fraction of the wavelength being used (about $\lambda/20$). There are several methods to increase this sensitivity, but the most common methods will now be described.

Multiple-reflection Interferometers

A method to increase the sensitivity of interferometric methods is to use multiple reflections, as in the Fabry-Perot interferometer. The Newton as well as the Fizeau interferometers can be made multiple-reflection interferometers by coating the reference surface and the surface under test with a high-reflection film. Then, the fringes are

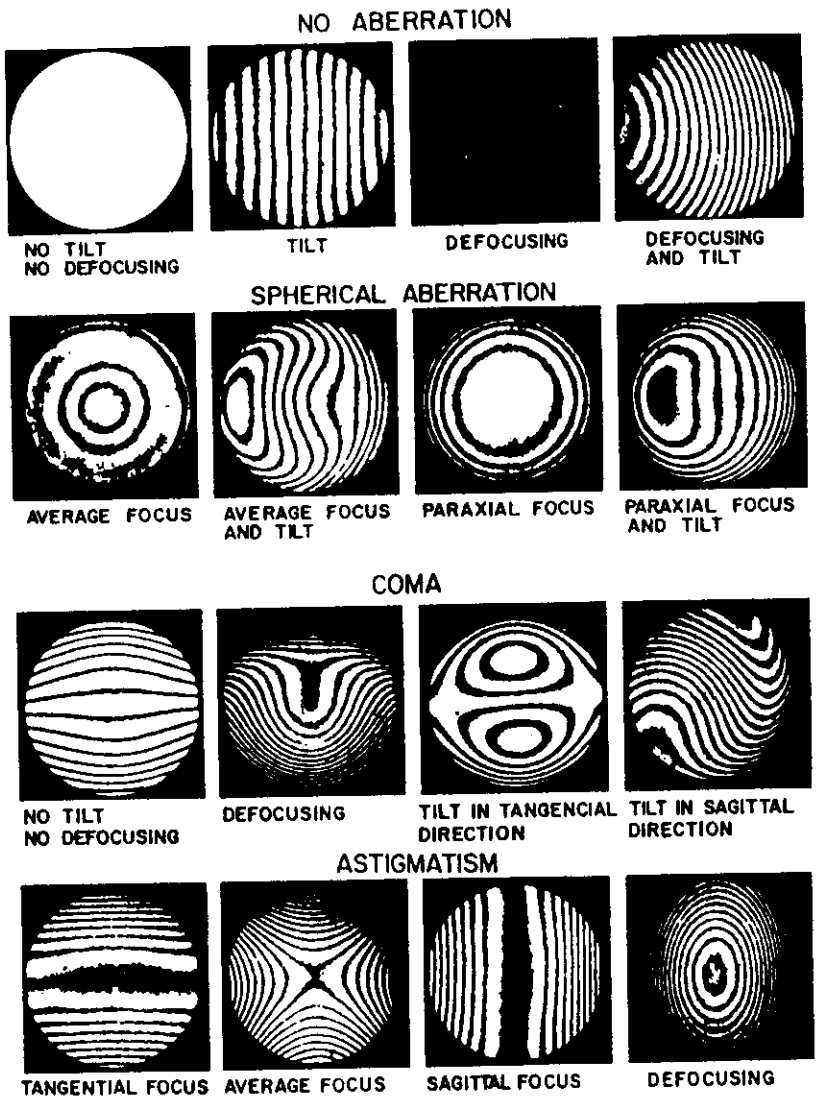

FIGURE 9 Twyman-Green interferograms. (*From D. Malacara, 1978.*)

greatly narrowed and their deviations from straightness are more accurately measured (Roychoudhuri, 1991).

Multiple-pass Interferometers

Another method to increase the sensitivity of interferometers is by double, or even multiple, pass. An additional advantage of double-pass interferometry is that the symmetrical and antisymmetrical parts of the wavefront aberration may be separated. This makes their identification easier, as Hariharan and Sen (1961) have proved. Several arrangements have been devised to use multiple pass (Hariharan, 1991).

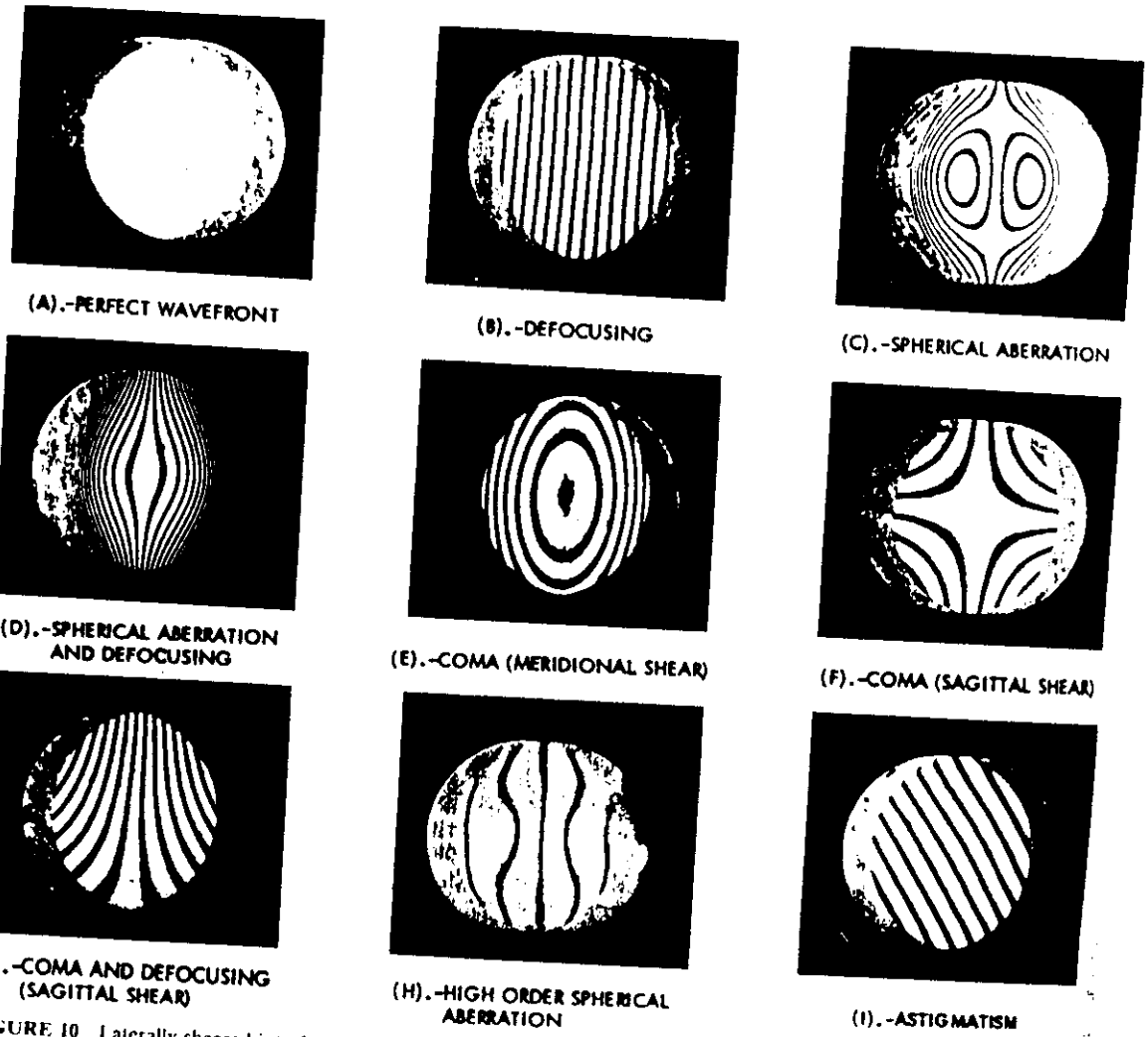

FIGURE 10 Laterally sheared interferograms. (*From D. Malacara, 1988.*)

Zernike Tests

The Zernike phase-contrast method is another way to improve the sensitivity of an interferometer to small aberrations. It was suggested by Zernike as a way to improve the knife-edge test (Zernike, 1934a). There are several versions of this test. The basic principle in all of them is the introduction of a phase difference equal to $\lambda/2$ between the wavefront under test and the reference wavefront. To understand why this phase difference is convenient, let us consider two interfering beams and irradiances $I_1(x, y)$ and $I_2(x, y)$ and a phase $\phi(x, y)$ between them. The final irradiance $I(x, y)$ in the interferogram is given by

$$I(x, y) = I_1(x, y) + I_2(x, y) + 2\sqrt{I_1(x, y)I_2(x, y)}\cos\phi(x, y) \tag{8}$$

Thus, the irradiance $I(x, y)$ of the combination would be a sinusoidal function of the phase, as illustrated in Fig. 13. If the phase difference is zero for a perfect wavefront

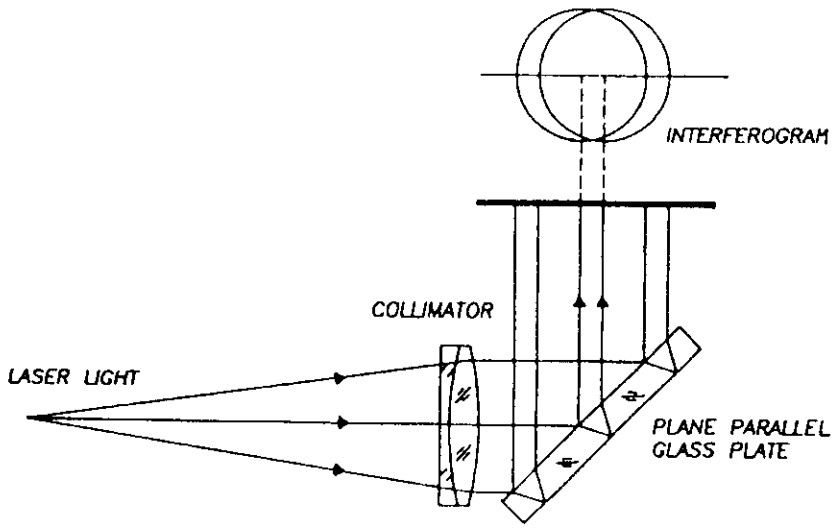

FIGURE 11 Murty's lateral shear interferometer.

deformations of the wavefront smaller than the wavelength of the light will not be easy to detect, because the slope of the function is zero for a phase near zero. The slope of this function is larger and linear for a phase value of 90°. Thus, the small wavefront deformations are more easily detected if the interferometer is adjusted, so that the wavefronts have a phase difference equal to 90° when the wavefront under test is perfect.

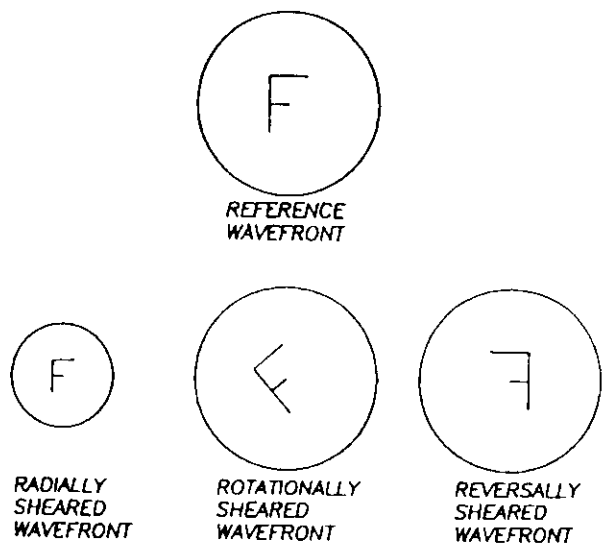

FIGURE 12 Wavefronts in radial, rotational, and reversal shear interferometers.

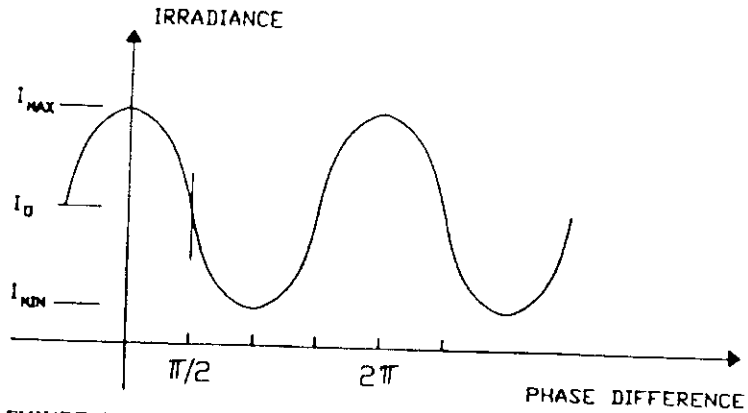

FIGURE 13 Irradiance in an interference pattern, as a function of the phase difference between the two interfering waves.

30.6 INTERFEROGRAM EVALUATION

An interferogram may be analyzed in several manners. One way begins by measuring several points on the interferogram, on top of the fringes. Then, the wavefront values between the fringes are interpolated. Another way uses a Fourier analysis of the interferogram. A third method interprets the fringe deformations as a phase modulation.

Fixed Interferogram Evaluation

Once the interferogram has been formed, a quantitative evaluation of it is a convenient method to find the wavefront deformations. The fixed interferogram evaluation by fringe measurements is done by measuring the position of several data points located on top of the fringes. These measurements are made in many ways, for example, with a measuring microscope, with a digitizing tablet, or with a video camera connected to a computer.

The fringe centers can be located either manually, using a digitizing tablet, or automatically, with the computer directly examining a single fringe image that has been captured using a digital frame grabber. After locating the fringe centers, fringe order numbers must be assigned to each point. The wavefront can then be characterized by direct analysis of the fringe centers. If desired, instead of global interpolation, a local interpolation procedure may be used.

To analyze the fringes by a computer, they must first be digitized by locating the fringe centers, and assigning fringe order numbers to them. The optical path difference (OPD) at the center of any fringe is a multiple m of the wavelength λ (OPD = $m\lambda$), where m is the fringe order. To obtain the wavefront deformation, only the relative values of the fringe order are important. So any value of the fringe order may be assigned to the first fringe being measured. However, for the second fringe, it may be increased or decreased by one. This choice affects only the sign of the OPD. An important disadvantage of the fixed interferogram analysis is that the sign of the OPD cannot be obtained from the interferogram alone. This information can be retrieved if the sign of any term in the wavefront deformation expression, like defocusing or tilt, is previously determined when taking the interferogram.

Fringes have been digitized using scanners (Rosenzweig and Alte, 1978), television cameras (Womack et al., 1979), photoelectric scanners, and digitizing tablets. Review

articles by Reid (1986, 1988) give useful references for fringe digitization using television cameras.

Global and Local Interpolation of Interferograms

After the measurements are made, the wavefront is computed with the measured points. The data density depends on the density of fringes in the interferogram. Given a wavefront deformation, the ratio of the fringe deviations from straightness to the separation between the fringes remains a constant, independently of the number of fringes introduced by tilting of the reference wavefront. If the number of fringes is large due to a large tilt, the fringes look more straight than if the number of fringes is small. Thus, the fringe deviations may more accurately be measured if there are few fringes in the interferogram. Thus, information about many large zones is lost. A way to overcome this problem is to interpolate intermediate values by any of several existing methods. One method is to fit the wavefront data to a two-dimensional polynomial with a least-squares fitting, as described by Loomis (1978) and Malacara et al. (1990) or by using splines as described by Hayslett and Swantner (1980) and Becker et al. (1982). Unfortunately, this procedure has many problems if the wavefront is very irregular. The values obtained with the polynomial may be wrong, especially near the edge, or between fringes if the wavefront is too irregular.

The main disadvantage of global fits is that they smooth the measured surface more than desired. Depending on the degree of the polynomial, there will be only a few degrees of freedom to fit many data points. It is even possible that the fitted surface will pass through none of the measured points. If the surface contains irregular features that are not well described by the chosen polynomial, such as steps or small bumps, the polynomial fit will smooth these features. Then, they will not be visible in the fitted surface.

Global interpolation is done by least-squares fitting the measured data to a two-dimensional polynomial in polar coordinates. The procedure to make the least-squares fitting begins by defining the variance σ of the discrete wavefront fitting as follows:

$$\sigma = \frac{1}{N}\sum_{i=1}^{N}[W_i' - W(\rho_i, \theta_i)]^2 \tag{9}$$

where N is the number of data points, W_i' is the measured wavefront deviation for data point i, and $W(\rho_i, \theta_i)$ is the functional wavefront deviation after the polynomial fitting. The only requirement is that this variance or fit error is minimized. It is well known that the normal least-squares procedure leads to the inversion of an almost singular matrix. Then, the round-off errors will be so large that the results will be useless. To avoid this problem, the normal approach is to fit the measured points to a linear combination of polynomials that are orthogonal over the discrete set of data points. Thus, the wavefront is represented by

$$W(\rho_i, \theta_i) = \sum_{n=1}^{I} B_n V_n(\rho_i, \theta_i) \tag{10}$$

$V(\rho, \theta)$ are polynomials of degree r and not the monomials x^r. These polynomials satisfy the orthogonality condition

$$\sum_{i=1}^{N} V_n(\rho_i, \theta_i) V_m(\rho_i, \theta_i) = E_n \delta_{nm} \tag{11}$$

where $E_n = \sum V_n^2$

The advantage of using these orthogonal polynomials is that the matrix of the system becomes diagonal and there is no need to invert it.

The only problem that remains is to obtain the orthogonal polynomials by means of the Gram-Schmidt orthogonalization procedure. It is important to notice that the set of orthogonal polynomials is different for every set of data points. If only one data point is removed or added, the orthogonal polynomials are modified. If the number of data points tends to infinity and they are uniformly distributed over a circular pupil with unit radius, these polynomials V_n approach the Zernike polynomials (Zernike, 1934b).

Several properties of orthogonal polynomials make them ideal for representing wavefronts, but the most important of them is that we may add or subtract one or more polynomial terms without affecting the fit coefficients of the other terms. Thus, we can subtract one or more fitted terms—defocus, for example—without having to recalculate the least-squares fit. In an interferometric optical testing procedure the main objective is to determine the shape of the wavefront measured with respect to a best-fit sphere. Nearly always it will be necessary to add or subtract some terms.

The only problem with these orthogonal polynomials over the discrete set of data points is that they are different for every set of data points. A better choice for the wavefront representation is the set of Zernike polynomials, which are orthogonal on the circle with unit radius, as follows.

$$\int_0^1 \int_0^{2\pi} U_n(\rho, \theta) U_m(\rho, \theta) \rho \, d\rho \, d\theta = F_{nm} \delta_{nm} \tag{12}$$

These polynomials are not exactly orthogonal on the set of data points, but they are close to satisfying this condition. Therefore, it is common to transform the wavefront representation in terms of the polynomials V_n to another similar representation in terms of Zernike polynomials U_n, as

$$W(\rho, \theta) = \sum_{n=1}^{J} A_n U_n(\rho, \theta) \tag{13}$$

Fourier Analysis of Interferograms

A completely different way to analyze an interferogram without having to make any interpolation between the fringes is by a Fourier analysis of the interferogram. An interpolation procedure is not needed because the irradiance at a fine two-dimensional array of points is measured and not only at the top of the fringes. The irradiance should be measured directly on the interferogram with a two-dimensional detector or television camera, and not on a photographic picture. Womack (1983, 1984), Macy (1983), Takeda et al. (1982), and Roddier and Roddier (1987) have studied in detail the Fourier analysis of interferograms to obtain the wavefront deformations.

Consider an interferogram produced by the interference of the wavefront under test and a flat reference wavefront, with a large tilt between them. The tilt is about the y axis, increasing the distance between the wavefronts in the x direction. The picture of this interferogram may be thought of as a hologram reconstructing the wavefront. Thus, three wavefronts (images) are generated when this hologram is illuminated with a flat wavefront. In order to have complete separation between these images, the tilt between the wavefronts must be large enough, so that the angle between them is not zero at any point over the interferogram. This is equivalent to saying that the fringes must be open, and never cross any line parallel to the x axis more than once. One image is the wavefront under test and another is the conjugate of this wavefront.

If the tilt between the wavefront is θ, and the wavefront shape is $W(x, y)$, the irradiance, from Eq. 5, is given by

$$I(x, y) = I_1(x, y) + I_2(x, y) + 2\sqrt{I_1(x, y)I_2(x, y)}\cos(\phi_0 + kx\sin\theta + kW(x, y)) \quad (14)$$

where $k = 2\pi/\lambda$. This expression may be rewritten as

$$I = [I_1 + I_2] + \sqrt{I_1}\sqrt{I_2}\,e^{i(kx\sin\theta + kW)} + \sqrt{I_1}\sqrt{I_2}\,e^{-i(kx\sin\theta + kW)} \quad (15)$$

The first term represents the zero order, the second is the real image, and the third is the virtual image. We also may say that the Fourier transform of the interferogram is formed by a Dirac impulse $\delta(f)$ at the origin and two terms shifted from the origin, at frequencies $+f_x$ and $-f_x$. The quantity f is the spatial frequency, defined by the tilt between the reference wavefront and the wavefront under test ($f = \sin\theta/\lambda$). These terms may be found by taking the Fourier transform of the interferogram. The term at $+f_x$ is due to the wavefront under test. This wavefront may be obtained by taking the Fourier transform of this term, mathematically isolated from the others. This method is performed in a computer by using the fast Fourier transform. The undesired terms are simply eliminated before taking the second fast Fourier transform in order to obtain the wavefront.

Direct Interferometry

This is another method to obtain the wavefront from an interferogram without the need of any interpolation. As in the Fourier method, the image of the interferogram is directly measured with a two-dimensional detector or television camera. The interferogram must have many fringes, produced with a large tilt between the wavefronts. The requirements for the magnitude of this tilt are the same as in the Fourier method.

Consider the irradiance in the interferogram along a line parallel to the x axis. This irradiance plotted versus the coordinate x is a perfectly sinusoidal function only if the wavefront is perfect, that is, if the fringes are straight, parallel, and equidistant. Otherwise, this function appears as a wave with a phase modulation. The phase-modulating function is the wavefront shape $W(x, y)$. If the tilt between the wavefronts is θ, the irradiance function is described by Eq. (14). If ϕ_0 is a multiple of 2π, this expression may be rewritten as

$$I = I_1 + I_2 + 2\sqrt{I_1 I_2}\cos(kx\sin\theta + kW) \quad (16)$$

Multiplying this phase-modulated function by a sinusoidal signal with the same frequency as the carrier $\sin(kx\sin\theta)$ a new signal S is obtained. Similarly, multiplying by a cosinusoidal signal $\cos(kx\sin\theta)$ a new signal C is obtained. If all terms in the signals S and C with frequencies equal to or greater than the carrier frequency are removed with a low pass filter, they become

$$S(x, y) = -\sqrt{I_1 I_2}\sin kW(x, y) \quad (17)$$

$$C(x, y) = \sqrt{I_1 I_2}\cos kW(x, y) \quad (18)$$

then, the wavefront $W(x, y)$ is given by

$$W(x, y) = -\frac{1}{k}\tan^{-1}\left[\frac{S(x, y)}{C(x, y)}\right] \quad (19)$$

which is our desired result.

30.7 PHASE-SHIFTING INTERFEROMETRY

All the methods just described are based on the analysis of a single static interferogram. Static fringe analysis is generally less precise than phase-shifting interferometry, by more than one order of magnitude. However, fringe analysis has the advantage that a single image of the fringes is needed. On the other hand, phase-shifting interferometry requires several images, acquired over a long time span during which the fringes must be stable. This is the main reason why phase-shifting interferometry has seldom been used for the testing of astronomical optics.

Phase-shifting interferometry (Bruning, 1974; Greivenkamp and Bruning, 1991) is possible, thanks to modern tools like array detectors and microprocessors. Figure 14 shows a Twyman-Green interferometer adapted to perform phase-shifting interferometry. Most conventional interferometers, like the Fizeau and the Twyman-Green, have been used to do phase shifting. A good review about these techniques may be found in the review article by Creath (1988).

In phase-shifting interferometers, the reference wavefront is moved along the direction of propagation, with respect to the wavefront under test, changing in this manner their phase difference. This phase shifting is made in steps or in a continuous manner. Of course this relative displacement of one wavefront with respect to the other may only be achieved through a momentary or continuous change in the frequency of one of the beams, for example, by Doppler shift, moving one of the mirrors in the interferometer. In other words, this change in the phase is accomplished when the frequency of one of the beams is modified in order to form beats.

By measuring the irradiance changes for different values of the phase shifts, it is possible to determine the initial difference in phase between the wavefront under test and

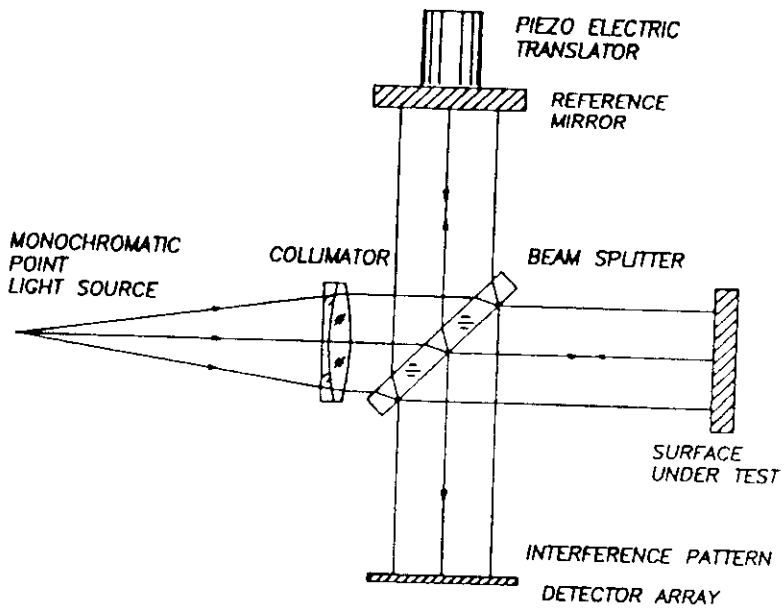

FIGURE 14 Twyman-Green interferogram adapted to do phase shifting.

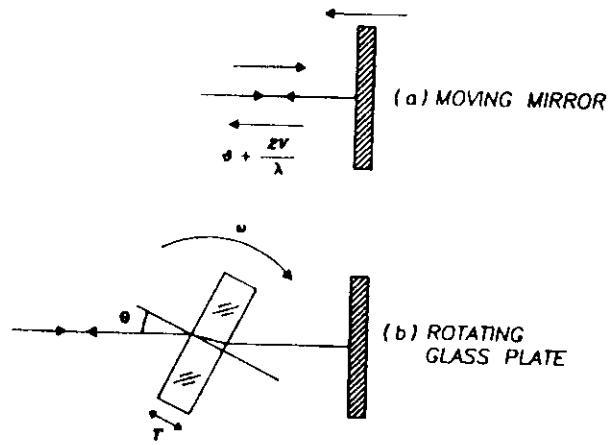

FIGURE 15 Obtaining the phase shift by means of a moving mirror or a rotating glass plate.

the reference wavefront, for that measured point over the wavefront. By obtaining this initial phase difference for many points over the wavefront, the complete wavefront shape is thus determined.

If we consider any fixed point in the interferogram, the initial phase difference between the two wavefronts has to be changed in order to make several measurements.

One method that can be used to shift this phase is by moving the mirror for the reference beam along the light trajectory, as in Fig. 15. This can be done in many ways, for example, with a piezoelectric crystal or with a coil in a magnetic field. If the mirror moves with a speed V, the frequency of the reflected light is shifted by an amount equal to $\Delta\nu = 2V/\lambda$.

Another method to shift the phase is by inserting a plane parallel glass plate in the light beam (see Fig. 15). Then the plate is rotated about an axis perpendicular to the optical axis.

The phase may also be shifted by means of the device shown in Fig. 16. The first

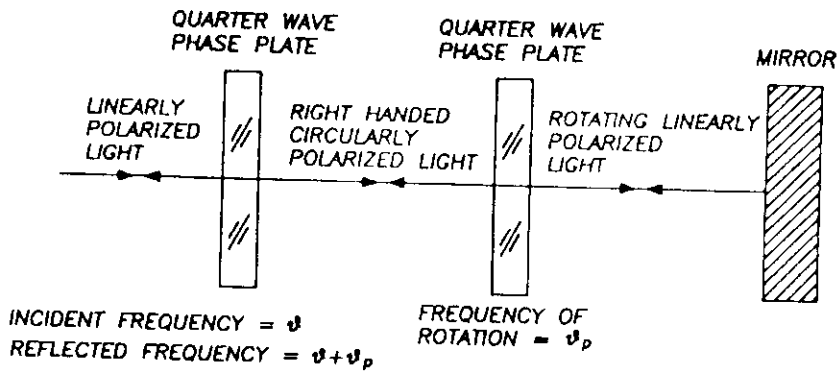

FIGURE 16 Obtaining the phase shift by means of phase plates and polarized light, with a double pass of the light beam.

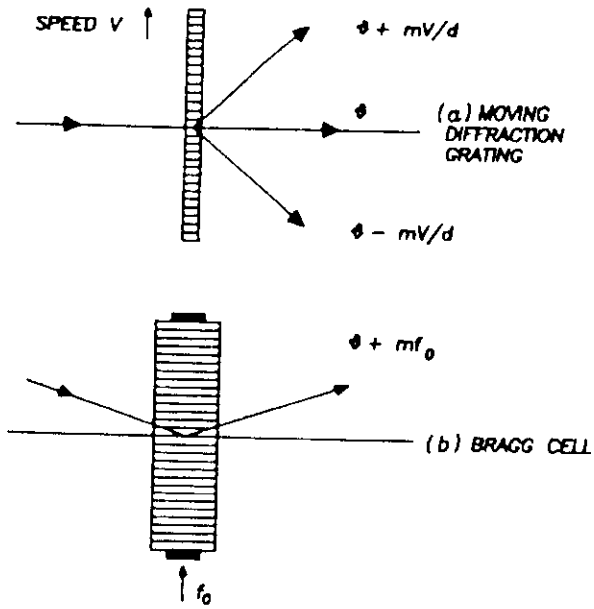

FIGURE 17 Obtaining the phase shift by means of diffraction: (*a*) with a diffraction grating; (*b*) with an acousto-optic Bragg cell.

quarter-wave retarding plate is stationary, with its slow axis at 45° with respect to the plane of polarization of the incident linearly polarized light. This plate also transforms the returning circularly polarized light back to linearly polarized. The second phase retarder is also a quarter-wave plate, it is rotating, and the light goes through it twice, therefore it is acting as a half-wave plate.

Still another manner to obtain the shift of the phase is by a diffraction grating moving perpendicularly to the light beam, as shown in Fig. 17*a*, or with an acousto-optic Bragg cell, as shown in Fig. 17*b*. The change in the frequency is equal to the frequency f of the ultrasonic wave times the order of diffraction m. Thus: $\Delta v = mf$.

The nonshifted relative phase of the two interfering wavefronts is found by measuring the irradiance with several predefined and known phase shifts. Let us assume that the irradiance of each of the two interfering light beams at the point x, y in the interference patterns are $I_1(x, y)$ and $I_2(x, y)$ and that their phase difference is $\phi(x, y)$. It was shown before, in Eq. (5), that the resultant irradiance $I(x, y)$ is a sinusoidal function describing the phase difference between the two waves. The basic problem is to determine the nonshifted phase difference between the two waves, with the highest possible precision. This may be done by any of several different procedures.

Phase Stepping

This method (Creath, 1988) consists of measuring the irradiance values for several known increments of the phase. There are several versions of this method, which will be described later. The measurement of the irradiance for any given phase takes some time, since there is a time response for the detector. Therefore, the phase has to be stationary during a

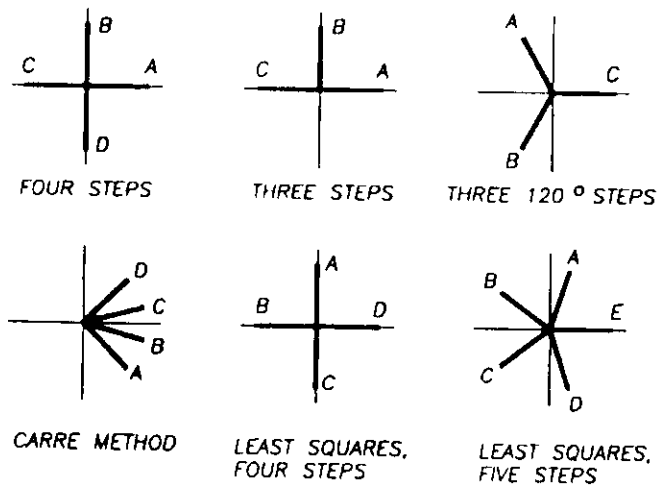

FIGURE 18 Six different ways to shift the phase using phase steps.

short time in order to take the measurement. Between two consecutive measurements, the phase is changed by an increment α_i. For those values of the phase, the irradiance becomes

$$I = I_1 + I_2 + 2\sqrt{I_1 I_2}\cos(\phi + \alpha_i) \tag{20}$$

There are six different algorithms, as shown in Fig. 18, with different numbers of measurements of the phase. As we see, the minimum number of steps needed to reconstruct this sinusoidal function is three. As an example with four steps,

$$I_A = I_1 + I_2 + 2\sqrt{I_1 I_2}\cos\phi \tag{21}$$

$$I_B = I_1 + I_2 - 2\sqrt{I_1 I_2}\sin\phi \tag{22}$$

$$I_C = I_1 + I_2 - 2\sqrt{I_1 I_2}\cos\phi \tag{23}$$

$$I_D = I_1 + I_2 + 2\sqrt{I_1 I_2}\sin\phi \tag{24}$$

From these relations the desired phase is

$$\phi(x, y) = \tan^{-1}\left\{\frac{I_D(x, y) - I_B(x, y)}{I_A(x, y) - I_C(x, y)}\right\} \tag{25}$$

Integrating Bucket

In the integrating phase-shifting method the detector continuously measures the irradiance during a fixed time interval, without stopping the phase. Since the phase changes continuously, the average value of the irradiance during the measuring time interval is measured. Thus, the integrating phase-stepping method may be mathematically considered a particular case of the phase-stepping method if the detector has an infinitely short time

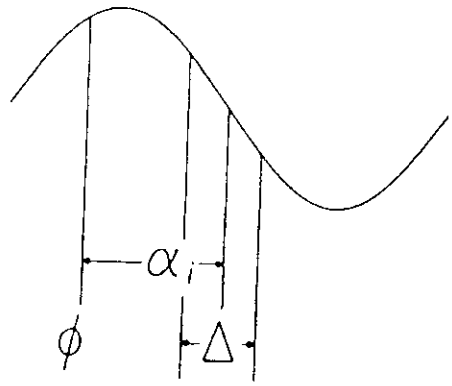

FIGURE 19 Averaged signal measurements with the integrating phase-shifting method.

response. Then, the measurement time interval is reduced to zero. If the measurement is taken as in Fig. 19, from $\alpha_i - \Delta/2$ to $\alpha_i + \Delta/2$ with center at α_i, then

$$I = \frac{1}{\Delta}\int_{\alpha_i - \Delta/2}^{\alpha_i + \Delta/2} [I_1 + I_2 + 2\sqrt{I_1 I_2}\cos(\phi + \alpha_i)]\, d\alpha \tag{26}$$

$$I = I_1 + I_2 + 2\sqrt{I_1 I_2}\,\text{sin c}(\Delta/2)\cos(\phi + \alpha_i) \tag{27}$$

In general, in the phase-stepping as well as in the integrating phase-shifting methods, the irradiance is measured at several different values of the phase α_i, and then the phase is calculated.

Two Steps Plus One Method

As pointed out before, phase-shifting interferometry is not useful for testing systems with vibrations or turbulence because the three or four interferograms are taken at different times. An attempt to reduce this time is the so-called two steps plus one method, in which only two measurements separated by 90° are taken (Wizinowich, 1989). A third reading is taken any time later, of the sum of the irradiance of the beams, independently of their relative phase. This last reading may be taken using an integrating interval $\Delta = 2\pi$. Thus

$$I_A = I_1 + I_2 + 2\sqrt{I_1 I_2}\cos\phi \tag{28}$$

$$I_B = I_1 + I_2 + 2\sqrt{I_1 I_2}\sin\phi \tag{29}$$

$$I_C = I_1 + I_2 \tag{30}$$

Therefore:

$$\phi = \tan^{-1}\left\{\frac{I_B - I_C}{I_A - I_C}\right\} \tag{31}.$$

Simultaneous Measurement

It has been said several times that the great disadvantage of phase-shifting interferometry is its great sensitivity to vibrations and atmospheric turbulence. To eliminate this problem, it has been proposed that the different interferograms corresponding to different phases be taken simultaneously (Bareket, 1985 and Koliopoulos, 1991). To obtain the phase-shifted

interferogram, they have used polarization-based interferometers. The great disadvantage of these interferometers is their complexity. To measure the images these interferometers have to use several television cameras.

Heterodyne Interferometer

When the phase shift is made in a continuous manner rather than in steps, the frequency of the shifting beam is permanently modified, and a beating between the two interferometer beams is formed (Massie, 1987).

The phase of the modulated or beating wave may be determined in many ways. One way is by electronic analog techniques, for example, using leading-edge detectors. Another way is by detecting when the irradiance passes through zero, that is, through the axis of symmetry of the irradiance function.

Phase Lock

The phase-lock method (Johnson et al., 1977, 1979; Moore, 1979) can be explained with the help of Fig. 20. Assume that an additional phase difference is added to the initial phase $\phi(x, y)$. The additional phase being added has two components, one of them with a fixed value and the other with a sinusoidal time shape. Both components can have any predetermined desired value. Thus:

$$\phi = \phi(x, y) + \delta(x, y) + a \sin \omega t \tag{32}$$

then, the irradiance $i(x, y)$ would be given by

$$I = I_1 + I_2 + 2\sqrt{I_1 I_2} \cos [\phi + \delta + a \sin \omega t] \tag{33}$$

The amplitude of the phase oscillations $a \sin \omega t$ is much smaller than π. We may now adjust the fixed phase δ to a value such that $\phi + \delta = \pi/2 + n\pi$. Then the value of $\cos(\phi + \delta)$ is zero. The curve is antisymmetric at this point; hence, only odd harmonics remain on the irradiance signal. This is done in practice by slowly changing the value of the phase δ, while maintaining the oscillation $a \sin \omega t$, until the maximum amplitude of the first harmonic, or fundamental frequency, is obtained. At this point, then, we have $\delta + \phi = \pi/2 + n\pi$, and since the value of δ is known, the value of ϕ has been determined.

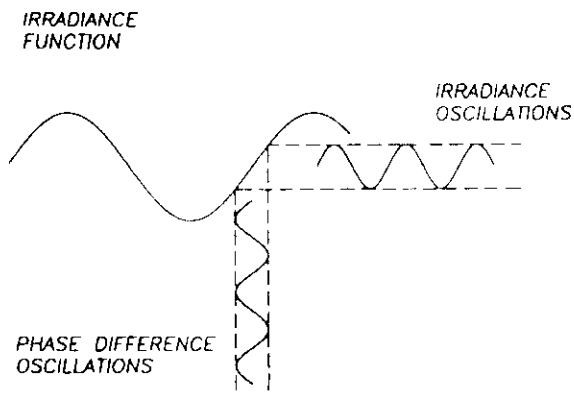

FIGURE 20 Phase-lock method to find the phase with a small sinusoidal modulation of the phase.

30.8 MEASURING ASPHERICAL WAVEFRONTS

The most common type of interferometer, with the exception of lateral or rotational shearing interferometers, produces interference patterns in which the fringes are straight, equidistant, and parallel, when the wavefront under test is perfect and spherical with the same radius of curvature as the reference wavefront.

If the surface under test does not have a perfect shape, the fringes will not be straight and their separations will be variable. The deformations of the wavefront may be determined by a mathematical examination of the shape of the fringes. By introducing a small spherical curvature on the reference wavefront (focus shift) or by changing its angle with respect to the wavefront under test (tilt), the number of fringes in the interferogram may by changed. This is done to reduce the number of fringes as much as possible, since the greater the number of fringes, the smaller the sensitivity of the test. However, for aspherical surfaces this number of fringes cannot be smaller than a certain minimum. The larger the asphericity is, the greater is this minimum number of fringes. Since the fringe separations are not constant, in some places the fringes will be widely spaced, but in some others the fringes will be too close together.

The sensitivity of the test depends on the separation between the fringes, because an error of one wavelength in the wavefront distorts the fringe shape by an amount equal to the separation between the fringes. Thus, the sensitivity is directly proportional to the fringe separation. When the fringes are widely separated, the sampled points will be quite separated from each other, leaving many zones without any information. On the other hand, where the fringes are very close to each other, there is a high density of sampled data points, but the sensitivity is low.

Then, it is desirable that the spherical aberration of the wavefront under test is compensated in some way, so that the fringes appear straight, parallel, and equidistant, for a perfect wavefront. This is called a null test and may be accomplished by means of some special configurations. These special configurations may be used to conduct a null test of a conic surface. These are described in several books (Malacara, 1991). Almost all of these surfaces have rotational symmetry.

If no testing configuration can be found to get rid of the spherical aberration, additional optical components, called null compensators, have to be used. Many different types of compensators have been invented. The compensators may be refractive (lenses), reflective (mirrors), or diffractive (real or computer-generated holograms).

Refractive or Reflective Compensators

The simplest way to compensate the spherical aberration of a paraboloid or a hyperboloid tested at the center of curvature is a single convergent lens placed near the point of convergence of the rays, as Fig. 21 shows. This lens is called a Dall compensator.

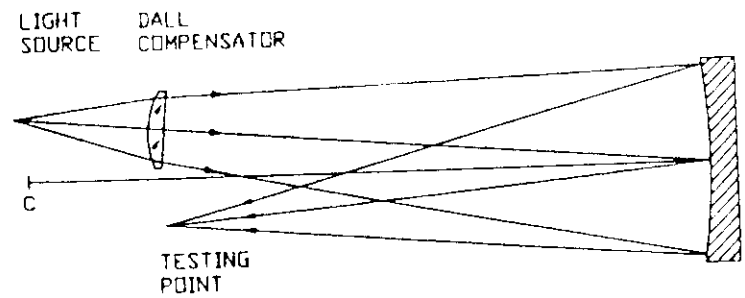

FIGURE 21 The Dall compensator.

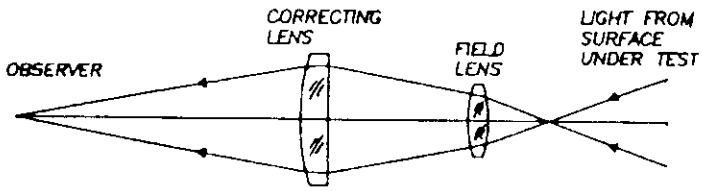

FIGURE 22 The Offner compensator. Only the reflected beam is shown.

Unfortunately, the correction due to a single lens is not complete, so a system of two lenses must be used to obtain a better compensation. This system is called an Offner compensator and is shown in Fig. 22. The field lens L is used to image the surface under test on the plane of the compensating lens L. Mirrors may also be used to design a null compensator.

As the sad experience of the Hubble space telescope proves, the construction parameters in a lens compensator have to be very carefully measured and adjusted, otherwise an imperfect correction is obtained either by undercorrection or overcorrection. The distance from the compensator to the surface under test is one of those parameters to be carefully measured. A way around this problem would be to assume that the compensator detects smoothness imperfections but not the exact degree of asphericity. This degree of asphericity may then be measured with some independent measurement like the Hartmann test.

Holographic Compensators

Diffractive holographic elements also may be used to compensate the spherical aberration of the system and to obtain a null test. The hologram may be real, produced by photographing an interferometric pattern. This pattern has to be formed by superimposing on the screen a wavefront like the one we have to test and a perfectly flat or spherical wavefront. The only problem with this procedure is that a perfect wavefront with the same shape as the wavefront to be tested has first to be produced. This is not always easy.

A better approach is to simulate the holographic interference pattern in a computer (Wyant, 1978) as in Fig. 23. Then this image is transferred to a small photographic plate, with the desired dimensions. There are many experimental arrangements to compensate the aspherical wavefront aberration with a hologram. One of these is illustrated in Fig. 24.

Infrared Interferometry

Another simple approach to reduce the number of fringes in the interferogram is to use a long infrared wavelength. Light from a CO_2 laser has been used with this purpose. It can also be used when the surface is still quite rough.

Two-wavelength Interferometry

In phase-shifting interferometry, each detector must have a phase difference smaller than π from the closest neighboring detector, in order to avoid 2π phase ambiguities and ensure phase continuity. In other words, there should be at least two detector elements for each fringe. If the slope of the wavefront is very large, the fringes will be too close together and the number of detector elements would be extremely large (Wyant et al., 1984).

A solution to this problem is to use two different wavelengths λ_1 and λ_2

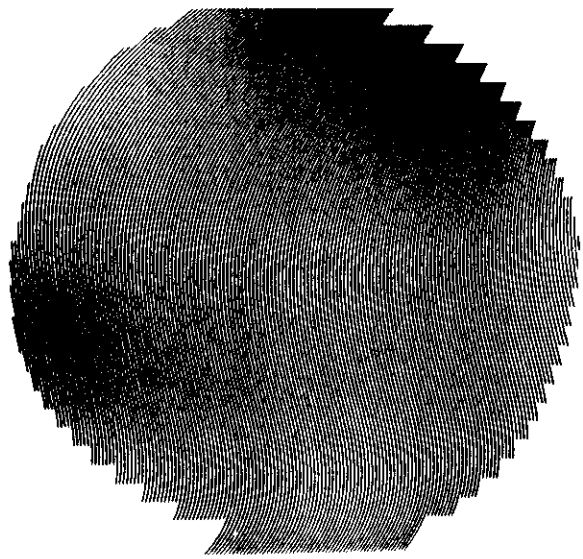

FIGURE 23 Computer-generated hologram for testing an aspherical wavefront. (*From Wyant, 1978.*)

simultaneously. The group wavelength or equivalent wavelength λ_{eq} is longer than any of the two components and is given by:

$$\lambda_{eq} = \frac{\lambda_1 \lambda_2}{|\lambda_1 - \lambda_2|} \tag{34}$$

Under these conditions, the requirement in order to avoid phase uncertainties is that there should be at least two detectors for each fringe produced if the wavelength is λ_{eq}.

The great advantage of this method is that we may test wavefronts with large

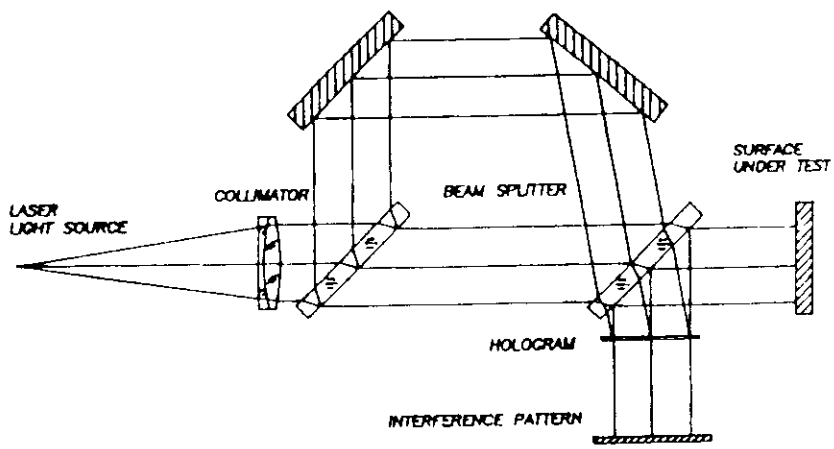

FIGURE 24 An optical arrangement for testing an aspherical wavefront with a computer-generated hologram.

asphericities, limited in asphericity by the group wavelength, and accuracy limited by the shortest wavelength of the two components.

Moiré Tests

An interferogram in which a large amount of tilt has been introduced is an ideal periodic structure to form moiré patterns. A moiré pattern represents the difference between two periodic structures. Thus, a moiré formed by two interferograms represents the difference between the two interferograms. There are several possibilities for the use in optical testing of this technique, as shown by K. Patorski (1988).

Let us assume that the two interferograms are taken from the same optical system producing an aspherical wavefront, but with two different wavelengths λ_1 and λ_2. The moiré obtained represents the interferogram that would be obtained with an equivalent wavelength λ_{eq} given by Eq. (31). If the tilt is of different magnitude in the two interferograms, the difference appears as a tilt in the moiré between them. Strong aspheric wavefronts may be tested with this method.

A second possibility is to produce the moiré between the ideal interferogram for an aspheric wavefront and the actual wavefront. Any differences between both would be easily detected.

Another possibility of application is for eliminating the wavefront imperfections in a low-quality interferometer. One interferogram is taken with the interferometer alone, without any optical piece under test. The second interferogram is taken with the optical component being tested. The moiré represents the wavefront deformations due to the piece being tested, without the interferometer imperfections.

Sub-Nyquist Interferometry

It was pointed out before that in phase-shifting interferometry each detector must have a phase difference smaller than π from the closest neighboring detector, in order to avoid 2π phase ambiguities and to ensure phase continuity. In other words, there should be at least two detector elements for each fringe. This condition is known as the Nyquist condition.

Since there is a minimum practical distance between detectors, the maximum asphericity in a surface to be tested by phase-shifting interferometry is only a few wavelengths. This condition may be relaxed (Greivenkamp, 1987) if the wavefront and its slope are assumed to be continuous on the whole aperture. Then, optical surfaces with larger asphericities may be tested.

30.9 REFERENCES

Bareket, N. "Three-Phase Phase Detector for Pulsed Wavefront Sensing," *Proc. SPIE* **551**:12 (1985).

Becker, F., G. E. A. Maier, and H. Wegner, "Automatic Evaluation of Interferograms," *Proc. SPIE* **359**:386 (1982).

Bruning, J. H., D. J. Herriott, J. E. Gallagher, D. P. Rosenfeld, A. D. White, and D. J. Brangaccio, "Digital Wavefront Measurement Interferometer," *Appl. Opt.* **13**:2693 (1974).

Creath, K., "Phase-Measurement Interferometry Techniques," in E. Wolf (ed.), *Progress in Optics* vol. XXVI, Elsevier Science Publishers, Amsterdam, 1988.

Foucault, L. M., "Description des Procedes Employes pour Reconnaitre la Configuration des Surfaces Optiques," *C.R. Acad. Sci. Paris* **47**:958 (1852); reprinted in Armand Colin, *Classiques de al Science*, vol. II.

Greivenkamp, J. E., "Sub-Nyquist Interferometry," *Appl. Opt.* **26**:5245 (1987).

Greivenkamp, J. and J. H. Bruning, "Phase Shifting Interferometers," in D. Malacara (ed.), *Optical Shop Testing*, 2d ed., John Wiley and Sons., New York, 1991.

Hariharan, P. and D. Sen, "The Separation of Symmetrical and Asymmetrical Wave-Front Aberrations in the Twyman Interferometer," *Proc. Phys. Soc.* **77**:328 (1961).

Hariharan, P., "Multiple-Pass Interferometers," in D. Malacara (ed.), *Optical Shop Testing*, 2d ed., John Wiley and Sons, New York, 1991.

Hartmann, J., "Bemerkungen über den Bann und die Justirung von Spektrographen," *Zt. Instrumentenkd.* **20**:47 (1990).

Hayslett, C. R. and W. Swantner,"Wave Front Derivation from Interferograms by Three Computer Programs," *Appl. Opt.* **19**:3401 (1980).

Johnson, G. W., D. C. Leiner, and D. T. Moore, "Phase Locked Interferometry," *Proc. SPIE* **126**:152 (1977).

Johnson, G. W., D. C. Leiner, and D. T. Moore, "Phase Locked Interferometry," *Opt. Eng.* **18**:46 (1979).

Koliopoulos, C. L., "Simultaneous Phase Shift Interferometer," *Proc. SPIE* (in press) (1991).

Loomis, J. S., "Analysis of Interferograms from Waxicons," *Proc. SPIE* **171**:64 (1979).

Malacara, D., *Optical Shop Testing*, 2d ed., John Wiley and Sons, New York, 1991.

Malacara, D., "Interference," in *Methods of Experimental Physics*, Academic Press, New York, 1988.

Malacara, D., J. M. Carpio-Valadéz, and J. J. Sánchez-Mondragón, "Wavefront Fitting with Discrete Orthogonal Polynomials in a Unit Radius Circle," *Opt. Eng.* **29**:672 (1990).

Macy, W. W., Jr., "Two Dimensional Fringe Pattern Analysis," *Appl. Opt.* **22**:3898 (1983).

Massie, N. A., "Digital Heterodyne Interferometry," *Proc. SPIE* **816**:40 (1987).

Moore, D. T., "Phase-locked Moire Fringe Analysis for Automated Contouring of Diffuse Surfaces," *Appl. Opt.* **18**:91 (1979).

Ojeda-Castañeda, J., "Foucault, Wire and Phase Modulation Tests," in D. Malacara (ed.), *Optical Shop Testing*, 2d ed., John Wiley and Sons, New York, 1991.

Patorski, K., "Moiré Methods in Interferometry," *Opt. and Lasers in Eng.* **8**:147 (1988).

Reid, G. T., "Automatic Fringe Pattern Analysis: A Review," *Opt. and Lasers in Eng.* **7**:37 (1986).

Reid, G. T., "Image Processing Techniques for Fringe Pattern Analysis," *Proc. SPIE* **954**:468 (1988).

Roddier, C. and F. Roddier, "Interferogram Analysis Using Fourier Transform Techniques," *Appl. Opt.* **26**:1668 (1987).

Ronchi, V., "Le Franque di Combinazione Nello Studio Delle Superficie e Dei Sistemi Ottici," *Riv. Ottica mecc. Precis.* **2**:9 (1923).

Roychoudhuri, C., "Multiple-Beam Interferometers," in D. Malacara (ed.), *Optical Shop Testing*, 2d ed., John Wiley and Sons., New York, 1991.

Takeda, M., H. Ina, and S. Kobayashi, "Fourier Transform Method of Fringe-Pattern Analysis for Computer-Based Topography and Interferometry," *J. Opt. Soc. Am.* **72**:156 (1982).

Wizinowich, P. L., "Systems for Phase Shifting Interferometry in the Presence of Vibration," *Proc. SPIE* **1164**:25 (1980).

Womack, K. H., J. A. Jonas, C. L. Koliopoulos, K. L. Underwood, J. C. Wyant, J. S. Loomis, and C. R. Hayslett, "Microprocessor-Based Instrument for Analysis of Video Interferograms," *Proc. SPIE* **192**:134 (1979).

Womack, K. H., "Frequency Domain Description of Interferogram Analysis," *Opt. Eng.* **23**:396 (1984).

Wyant, J. C., "Holographic and Moire Techniques," in D. Malacara (ed.), *Optical Shop Testing*, John Wiley and Sons, New York, 1978.

Wyant, J. C., B. F. Oreb, and P. Hariharan, "Testing Aspherics Using Two-Wavelength Holography: Use of Digital Electronic Techniques," *Appl. Opt.* **23**:4020 (1984b).

Zernike, F., "Diffraction Theory of Knife Edge Test and its Improved Form, The Phase Contrast," *Mon. Not. R. Astron. Soc.* **94**:371 (1934a).

Zernike, F., "Begünstheorie des Schneidener-Fahrens und Seiner Verbasserten Form, der Phasenkontrastmethode," *Physica.* **1**:689 (1934b).

ELSEVIER

Optics and Lasers in Engineering **26** (1997) 1–42

0143-8166/97/$15.00

0143-8166(95)00069-0

Some Applications of the Murty Interferometer: A Review

R. P. Shukla

Spectroscopy Division, Bhabha Atomic Research Centre, Trombay, Bombay 400 085, India

&

Daniel Malacara

Centro de Investigaciones en Optica, A. C., Apdo. Post. 948, 37000 León, Gto., Mexico

ABSTRACT

Several applications of the Murty interferometer in the testing of optical systems and components are reviewed in this article. The interferometer has applications in the testing of lenses, spherical mirrors, paraboloidal mirrors and parallel plates. The interferometer can also be used for the determination of homogeneity of optical materials, measurement of refractive indices of glasses and liquids, measurement of radii of curvature and location of cardinal points, checking the laser beam collimation, determination of the power of ophthalmic lenses, measurement of refractive indices of simple lenses, measurement of birefringence of optical materials, thermal expansion coefficient of metallic bars and optical distortion in transparencies or glass windows. Copyright © 1996 Elsevier Science Ltd.

1 INTRODUCTION

Lateral shearing interferometers have certain advantages over conventional interferometers, mainly that they do not require a perfect reference wavefront. In the lateral shearing interferometer, a test wavefront is shifted laterally with respect to itself and this acts as a reference wavefront, thereby avoiding the need for a standard test surface. These interferometers were devised by several authors, as shown in the references at the end of the chapter. Ordinary sources of light having broad spectral lines were used in these interferometers and

hence zero-order compensation was required. In order to have interference between the sheared wavefronts in such interferometers, the angular size of the source must be very small to give spatial coherence over the entire wavefront. This condition was fulfilled by reducing the source size to the diffraction limited size at the cost of the brightness of the fringes. When the He–Ne laser operating at 632·8 nm, which has a highly monochromatic and highly spatially coherent beam in TEMoo mode, became available, Murty[1] suggested the use of a laser in a lateral shearing interferometer, now known as a Murty interferometer in the literature.[2,3,6a] This instrument was used for the testing of lenses, mirrors, parallel plates, and paraboloidal mirrors by several authors.[4–6] It can also be used for determining the homogeneity of optical materials, measuring refractive indices of glasses, measuring the radius of curvature of test plates and locating the cardinal points of an optical system. This interferometer has also been used with infrared light, by employing a screen that can be observed with an infrared viewer. For CO_2 lasers the plate has been made with ZnSe (zinc selenide) or germanium and a pyroelectric detector for viewing the fringes. This interferometer is so useful that there are some commercially available versions, manufactured by companies such as Blue Sky Research, Melles Griot, Optical Systems Div. and Continental Optical Corp. The purpose of this paper is to review the applications of the Murty interferometer. The information presented in this article will be useful to the various workers in optics, mainly in the field of laser interferometry applied to testing of optics. There are many other types of lateral shearing interferometer, for example, grating interferometers, but they will not be considered here.

1.1 Basic theory

In the Murty interferometer, as in any other lateral shear interferometer, the wavefront interferes with a copy of it, laterally displaced by an amount S in the x direction. The wavefront may be represented by $W(x, y)$ and the laterally displaced wavefront by $W(x - S, y)$. By expanding in a Taylor series, the optical path difference between the two wavefronts may be written as

$$W(x, y) - W(x - S, y) = \left(\frac{\partial W}{\partial x}\right) S - \left(\frac{\partial^2 W}{\partial x^2}\right) \frac{S^2}{2} + \cdots \qquad (1)$$

Only the first term needs to be considered, if S is very small, so that

$$S \ll 2\frac{\left(\frac{\partial W}{\partial x}\right)}{\left(\frac{\partial^2 W}{\partial x^2}\right)} \tag{2}$$

To satisfy this condition, the ratio of the gradient, given by the first derivative, to the local curvature, represented by the second derivative, must be small at any point on the aperture. In other words, the wavefront must be smooth with small aberrations. Thus in a first approximation, the shape of the fringes is given by

$$\left(\frac{\partial W}{\partial x}\right)S = n\lambda \tag{3}$$

where n is the order of interference. Since $(\partial W/\partial x)$ is the gradient of the wavefront, we conclude that the fringes are the locus of points on the wavefront, with constant gradient in the direction of the shear. This gradient represents the component of the transverse aberration of the ray in the direction of the shear, TA_x. Thus we may also write

$$TA_x S = n\lambda \tag{4}$$

This expression tells us that a lateral shearing interferometer does not directly measure the optical path difference or wavefront deformations OPD as most interferometers, but the value of the transverse aberration TA_x in the direction of the shear. The wavefront deformations OPD may be indirectly obtained by integrating the relationship

$$\frac{\partial W(x, y)}{\partial x} = -\frac{TA_x}{r_{ref}} \tag{5}$$

where r_{ref} is the radius of curvature of the reference wavefront, or the distance from the vertex of the wavefront to the plane where the transverse aberrations are measured, if this plane is not at the center of curvature of the wavefront.

We may notice that the wavefront deformations over the complete aperture may not be obtained with a single interferogram. Two interferograms with lateral shears in perpendicular directions are needed. A rotatable shear plate interferometer has been designed by Sweatt[7] in order to be able to take these interferograms, one after the other, in a minimum amount of time. The shear plate is fixed in a mount that allows the direction of shear to be rotated.

When the wavefront deformations with respect to the reference

sphere are also spherical, we say that we have pure defocusing. Then, the wavefront may be written as

$$W(x, y) = D(x^2 + y^2) \tag{6}$$

where D is a defocusing coefficient, equal to $D = 1/2r$ if the reference wavefront is flat and the wavefront has a radius of curvature r, as is normally the case for a Murty interferometer. If the reference wavefront is not flat but has a radius of curvature r_{ref}, the defocusing coefficient is equal to $D = \Delta r/2r_{ref}^2$, where Δr is the difference in the radii of curvature of the wavefront and its reference. Substituting this wavefront expression in eqn (3) we find

$$2DxS = n\lambda \tag{7}$$

This is a system of straight, parallel and equidistant fringes, with separation X equal to $\lambda/2DS$. Thus, in the Murty interferometer the spatial frequency $1/X$ of the system of fringes is $2DS/\lambda = S/r\lambda$. In other words, the spatial frequency of the fringes in the direction of the lateral shear is directly proportional to the curvature $c = 1/r$ of the wavefront and to the magnitude of this lateral shear S. In a complicated interferogram, with highly deformed fringes, the local frequency of the fringes in the direction of the shear would give an indication of the local curvature of the wavefront.

In the Murty interferometer shown in Fig. 1, the light is reflected from the front and back surfaces of the plate and because of the thickness of the plate there is lateral shear. The lateral shear S for a

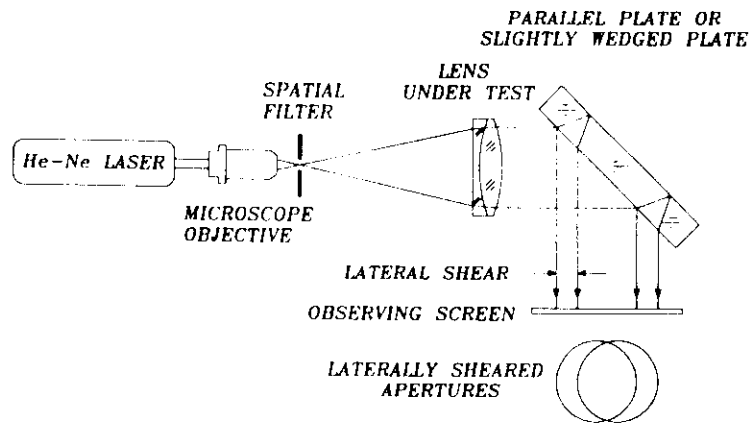

Fig. 1. Schematic diagram showing the parallel plate used as a lateral shearing interferometer.

plate of thickness T and refractive index N, and for an angle of incidence θ, is given by Malacara[32a] as

$$S = \frac{T \sin 2\theta}{\sqrt{N^2 - \sin^2 \theta}} \tag{8}$$

For a glass with $N = 1{\cdot}515$ at 632·8 nm, Fig. 2 shows the plot of S/T versus θ. From this it is seen that S has a maximum value of about 0·8, corresponding to an angle of incidence of 50°. Therefore a 45° angle is quite convenient to use in a practical setup. The maximum lateral shear for any refractive index is given by

$$\sin^2 \theta = N^2 - N\sqrt{N^2 - 1} \tag{9}$$

An interesting problem solved by Mantravadi[6] is the calculation of whether there is any material with a refractive index that gives a maximum lateral shear at 45° incidence. From eqn (9) we may find that if we want this maximum shear to occur at 45°, the refractive index N has to be infinity. Thus, θ has to be greater than 45° if we want the maximum shear with a real index of refraction.

2 TESTING OF LENSES AND MIRRORS

2.1 Testing of lenses

The schematic diagram of the Murty interferometer for testing a collimating lens is shown in Fig. 1. The light from the He–Ne laser is focused by a suitable microscope objective on a pinhole located at the focus of a collimating lens.[8] The collimated beam of light is incident on the parallel plate which is normally used without any coating on either surface. Figure 3 shows some lateral shearing interferograms of aberrated lenses, taken with this interferometer.

The interference takes place between the sheared wavefronts in a common area. If the lens under test is perfect, a fringe-free field is obtained for a well-collimated beam. When the collimation is not perfect, but there is a small amount of defocusing, straight fringes occur in the field, as shown in Fig. 4. The direction of the fringes is perpendicular to the direction of shear. Hence, the interferometer may be used for checking the collimation of the beam.

In the above-mentioned arrangement, the glass plate was considered as strictly parallel. Such an arrangement is not convenient for the testing of lenses suffering from small aberrations because the common

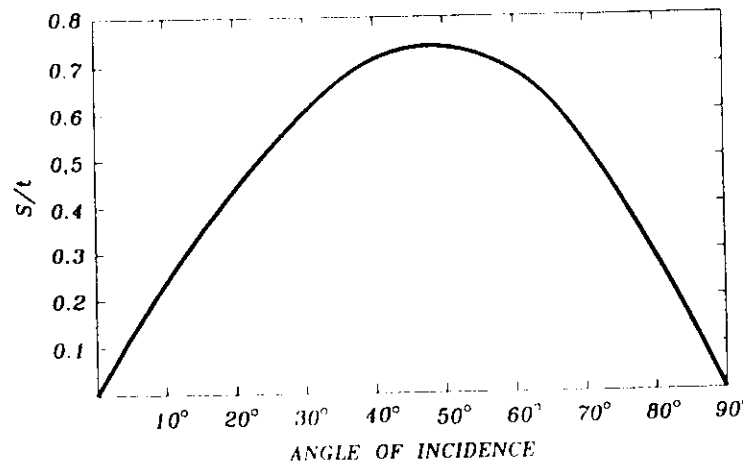

Fig. 2. Plot of S/t versus angle of incidence for a typical borosilicate crown glass plate. From the plot it is seen that any angle of incidence up to a maximum of 50° is convenient.

area between the beams appears fringe-free when the light is perfectly collimated. It is usually convenient to have a small tilt between the two sheared beams in a direction perpendicular to the direction of the lateral shear. This is easily achieved by making the plate slightly wedge-shaped. The apex of the wedge-shaped plate is set parallel to the direction of shear. The direction of the wedge may be easily determined by using the glass plate in a Fizeau configuration, as shown in Fig. 5. With the wedge set parallel to the shear, the fringes would be straight and parallel to the direction of shear for the exact collimated beam. Hence, when an optical system is being collimated, we go through the region of the focus, obtaining the sequence of interferograms as in Fig. 6. Thus, it is possible to detect a slight defocusing, because we are looking for a change in the direction of the fringes rather than the absence of them. At the focus the fringes are parallel to the direction of shear, whereas inside and outside of focus they are inclined. The quality of the optical system may also be determined by analyzing the shearing interferogram.

If the wedge angle of the glass plate is ψ in a first approximation, then the tilt angle between the wavefronts is equal to $\gamma = 2N\psi$. However, as pointed out by Mantravadi,[6] since the plate is normally used with an angle of incidence of 45°, the tilt γ between the wavefronts is more accurately given by

$$\gamma = 2\psi\sqrt{N^2 - \sin^2\theta} \tag{10}$$

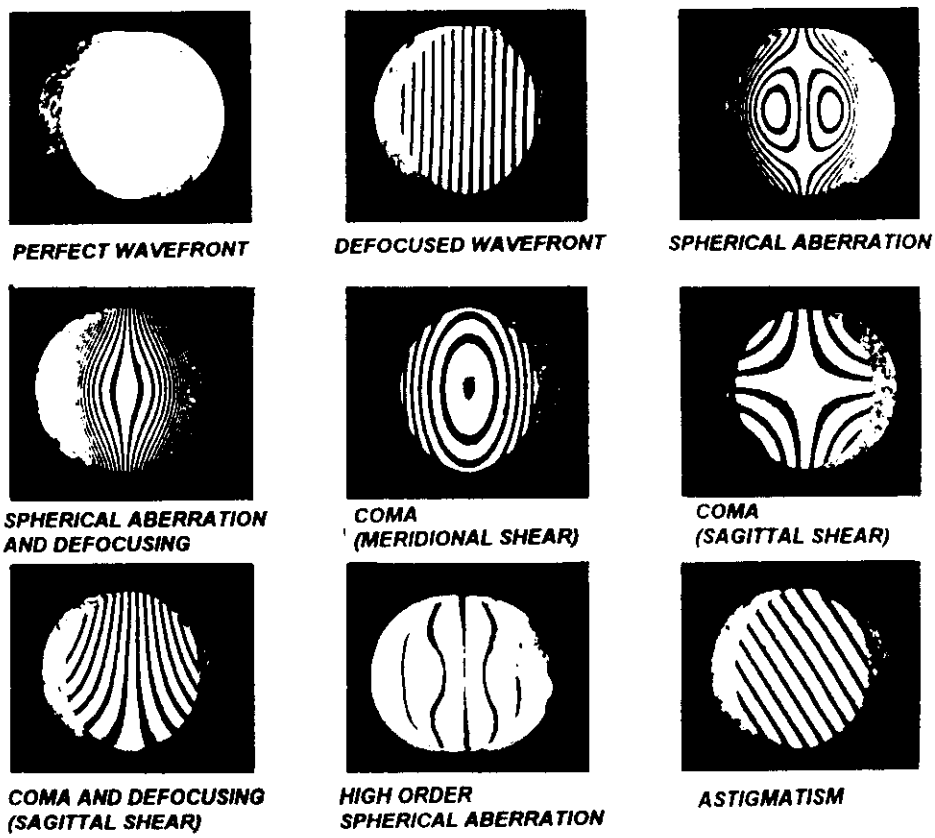

Fig. 3. Lateral shear interferograms in a Murty interferometer, for the primary aberrations.

which, for $\theta = 45°$ gives

$$\gamma = 2\sqrt{N^2 - 0{\cdot}5\psi}$$

The primary or Seidel aberrations produce very characteristic interference patterns that permit us an easy and fast identification of these aberrations, as shown in Fig. 3. The primary aberrations may be represented by

$$W = D(x^2 + y^2) + A(x^2 + y^2)^2 + B_y y(x^2 + y^2) + B_x x(x^2 + y^2) + C(x^2 - y^2) \tag{11}$$

where the first term D as described in the preceding section, is the defocusing coefficient, equal to $D = 1/2r$ with r being the radius of curvature of the wavefront. The second term is the primary spherical aberration. The third and fourth terms represent the primary coma aberration, when the image has been displaced off-axis in the y

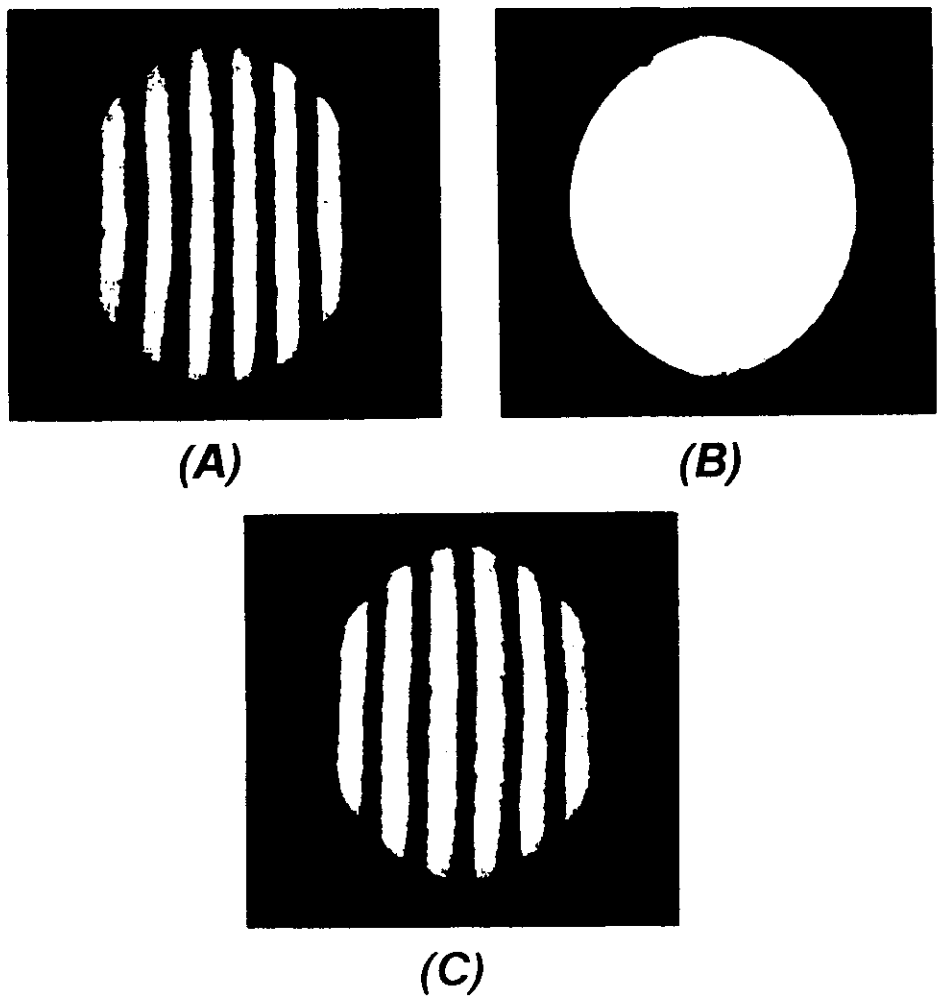

Fig. 4. Sequence of lateral shearing interferogram for an aberrationless wavefront as one passes through the focus. The central fringe pattern is obtained when there is no defocusing. The patterns on either side are due to slight defocusing in either direction by the same amount. (A) inside the focus, (B) at the focus, (C) outside the focus.

direction and when the image has been displaced off-axis in the x direction, respectively. Finally, the fifth term is the astigmatism. Then, from eqn (3), the interference pattern for a lateral shear S in the x (sagittal) direction is

$$2DxS + 4A(x^2 + y^2)xS + 2BxyS + 2CxS = n\lambda \tag{12}$$

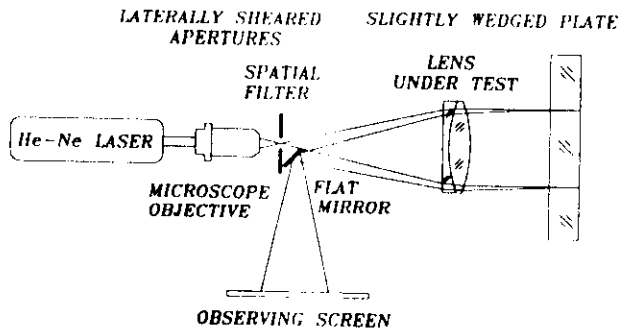

Fig. 5. Fizeau configuration to find the direction of the wedge in the glass plate.

and the interference pattern for a lateral shear T in the y (tangential) direction is

$$2DxT = 4A(x^2 + y^2)xT + B(x^2 + 3y^2)T - 2CyT = n\lambda \tag{13}$$

The procedure for calculating the shape of the wavefront when it has many kinds of deformation, not only primary abberations, is given in several publications.[9–15] Some methods[14] involve the fitting of the wavefront to a two-dimensional function, typically to Zernike polynomials. This procedure is very accurate, but requires that the wavefront be sufficiently smooth, without any strong local irregularities. Another simple method not requiring polynomial fitting[9,15] is shown in Fig. 7. In this method the interference pattern is scanned from left to right along a line in the shear direction and the wavefront differences ΔW_i are estimated at equally spaced points. This spacing between the data point must be equal to the magnitude S of the lateral shear, obtaining

$$\begin{aligned} W_1 &= 0 \\ W_2 &= \Delta W_1 \\ W_3 &= \Delta W_1 + \Delta W_2 \\ W_4 &= \Delta W_1 + \Delta W_2 + \Delta W_3 \\ &\vdots \\ W_j &= \Delta W_1 + \Delta W_2 + \Delta W_3 + \cdots + \Delta W_{j-1} \end{aligned} \tag{14}$$

These methods require a lot of computation; however, a qualitative estimation of the wavefront accuracy can be done by observing the deviation of the fringes from the ideal linear pattern, as in the interferograms in Fig. 3.

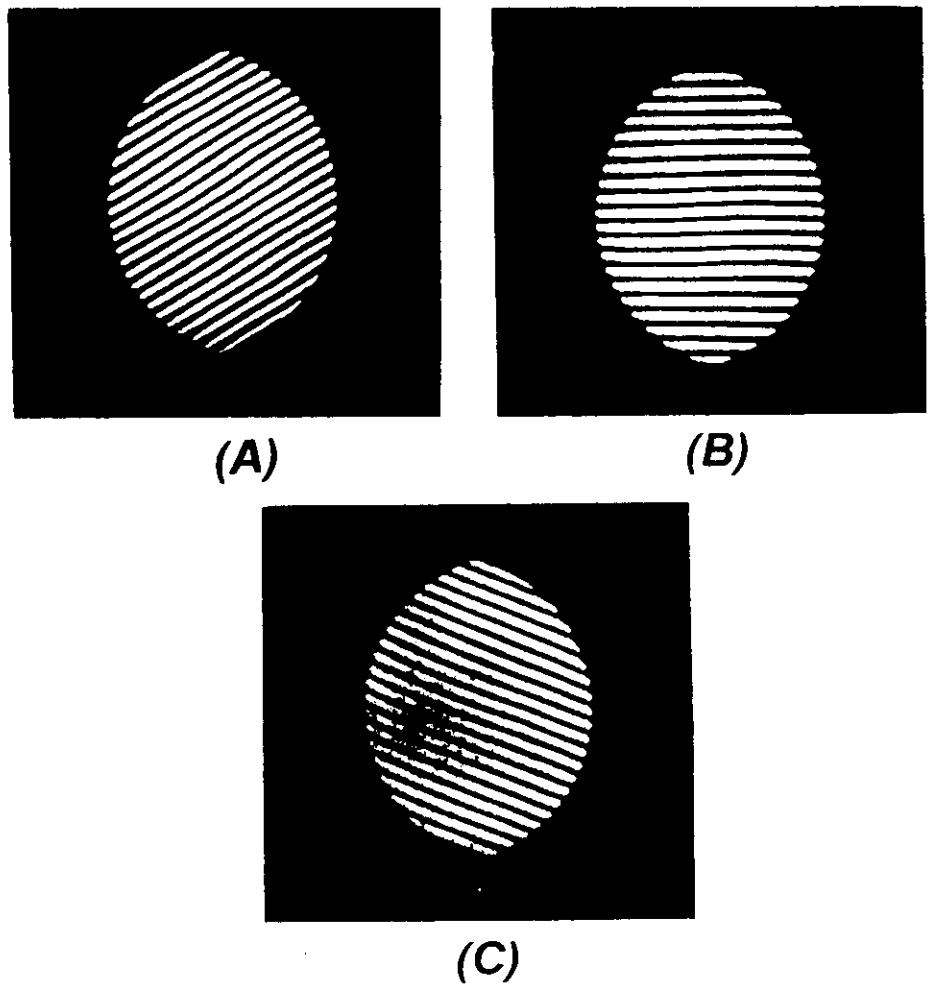

Fig. 6. Sequence of lateral shearing interferograms of an aberrationless wavefront as one passes through the focus. In this case, a certain amount of tilt orthogonal to the direction of shear is introduced. At the focus the fringes are parallel to the direction of shear, whereas inside and outside the focus they are inclined. (A) Inside the focus, (B) at the focus, (C) outside the focus.

2.2 Testing of large optics

The interferometer can be used in the testing of large optics because a reference surface as large as the test surface is not required in the setup because the wavefront is compared with itself. The reference and test wavefronts obtained from the shearing plate travel almost identical paths and therefore the vibrations and turbulence of the medium are

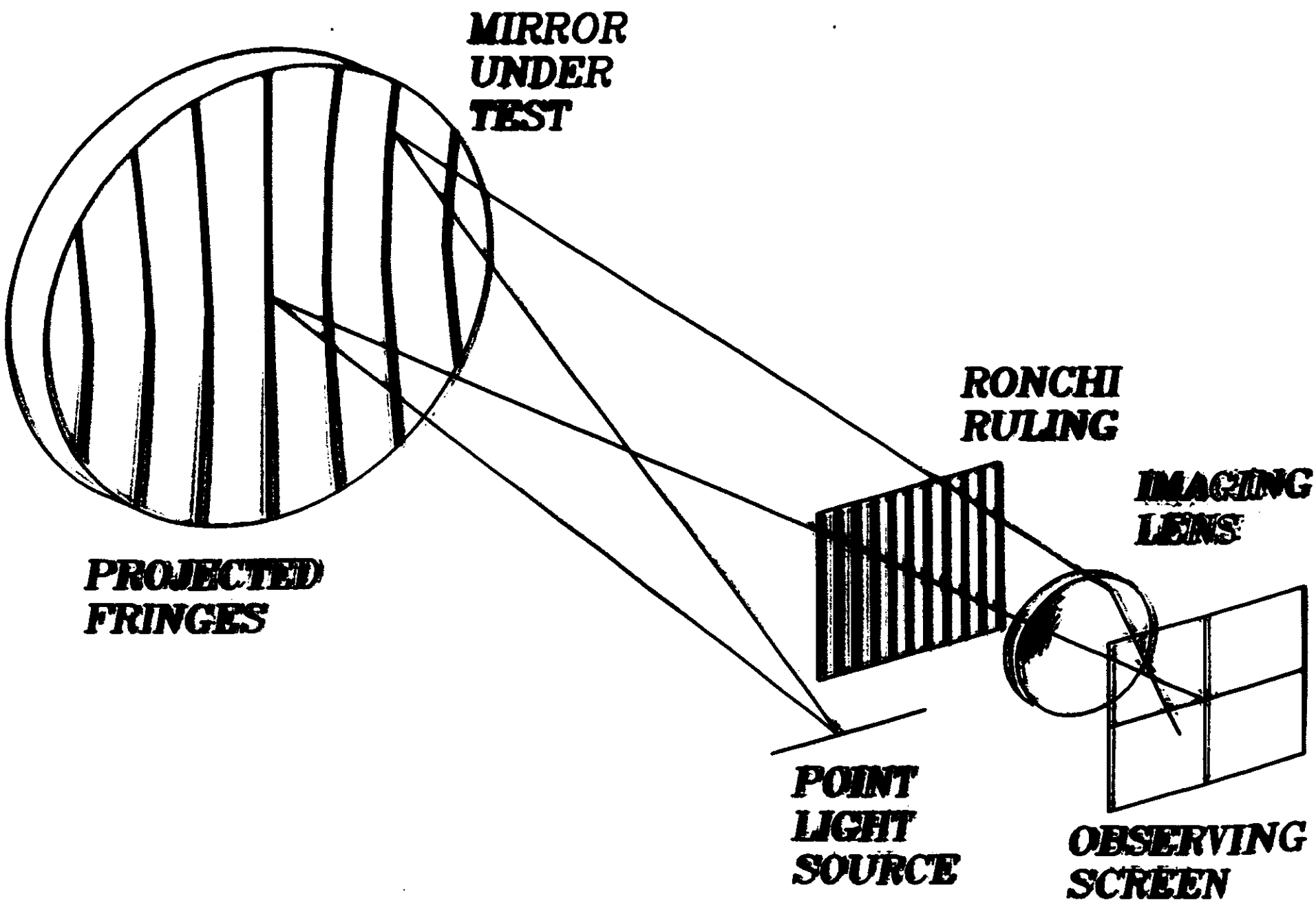
MIRROR
UNDER
TEST
PROJECTED
FRINGES
RONCHI
RULING
IMAGING
LENS
POINT
LIGHT
SOURCE
OBSERVING
SCREEN

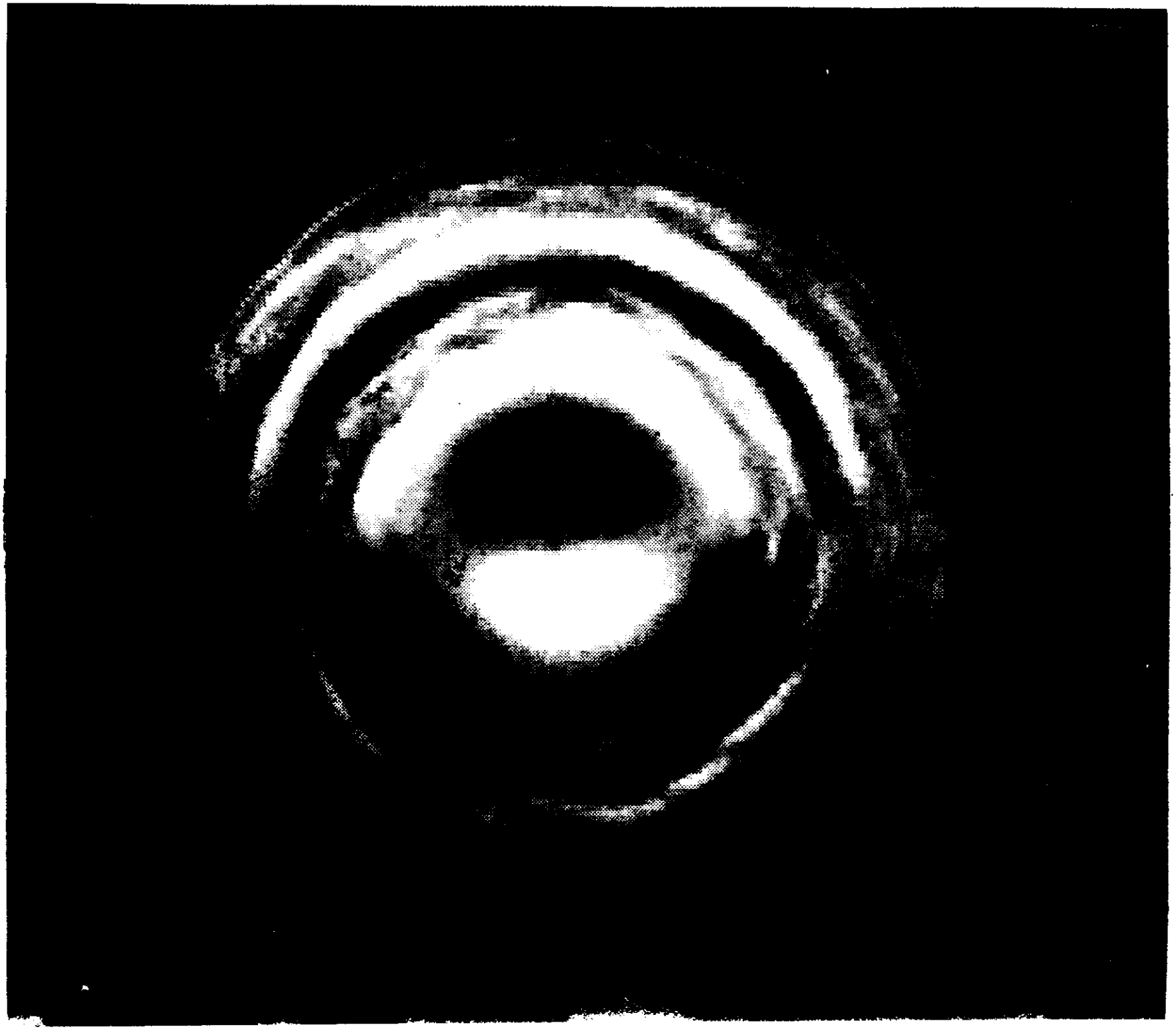

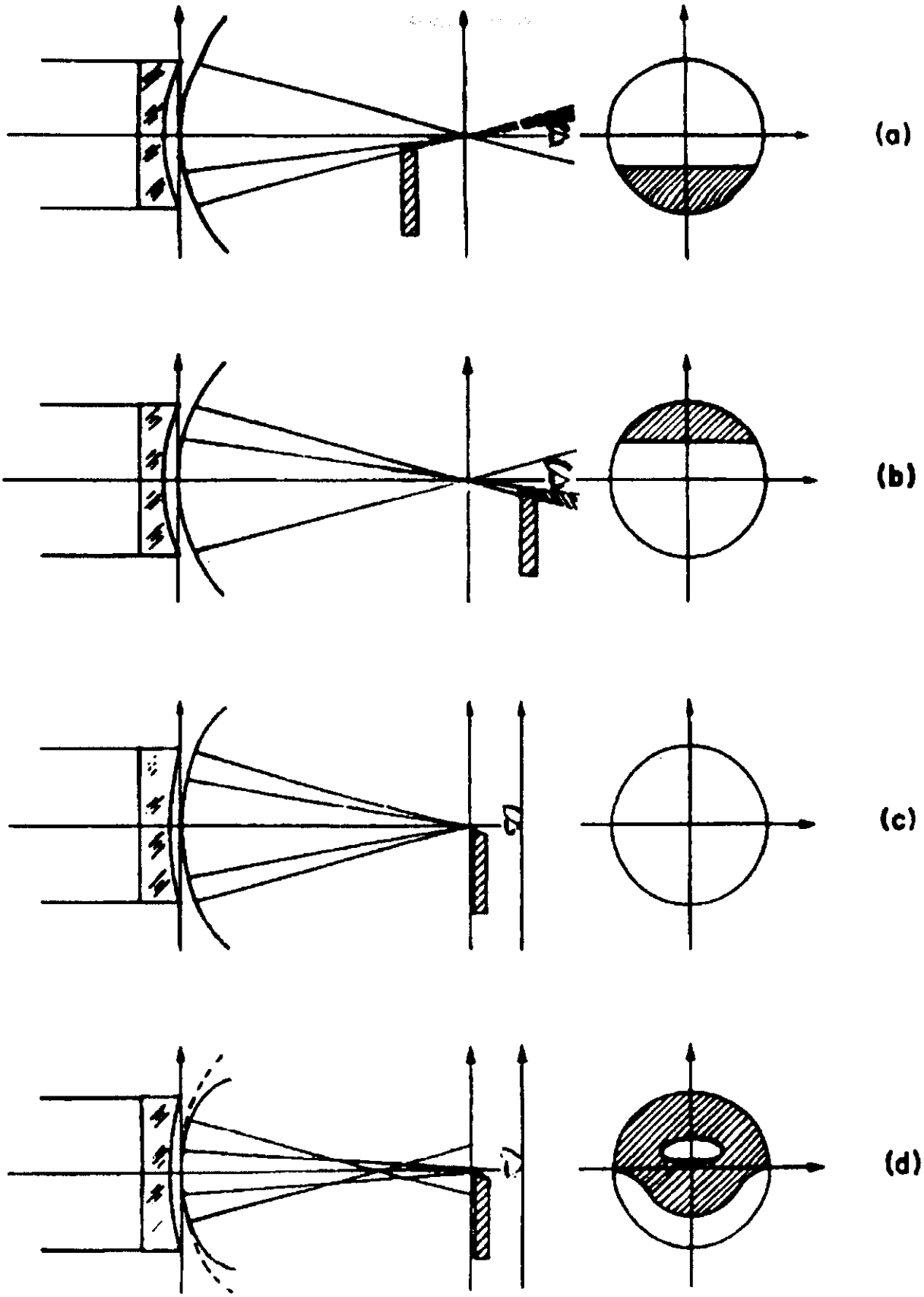

Foucault test of a spherical mirror, at several positions of the knife edge.

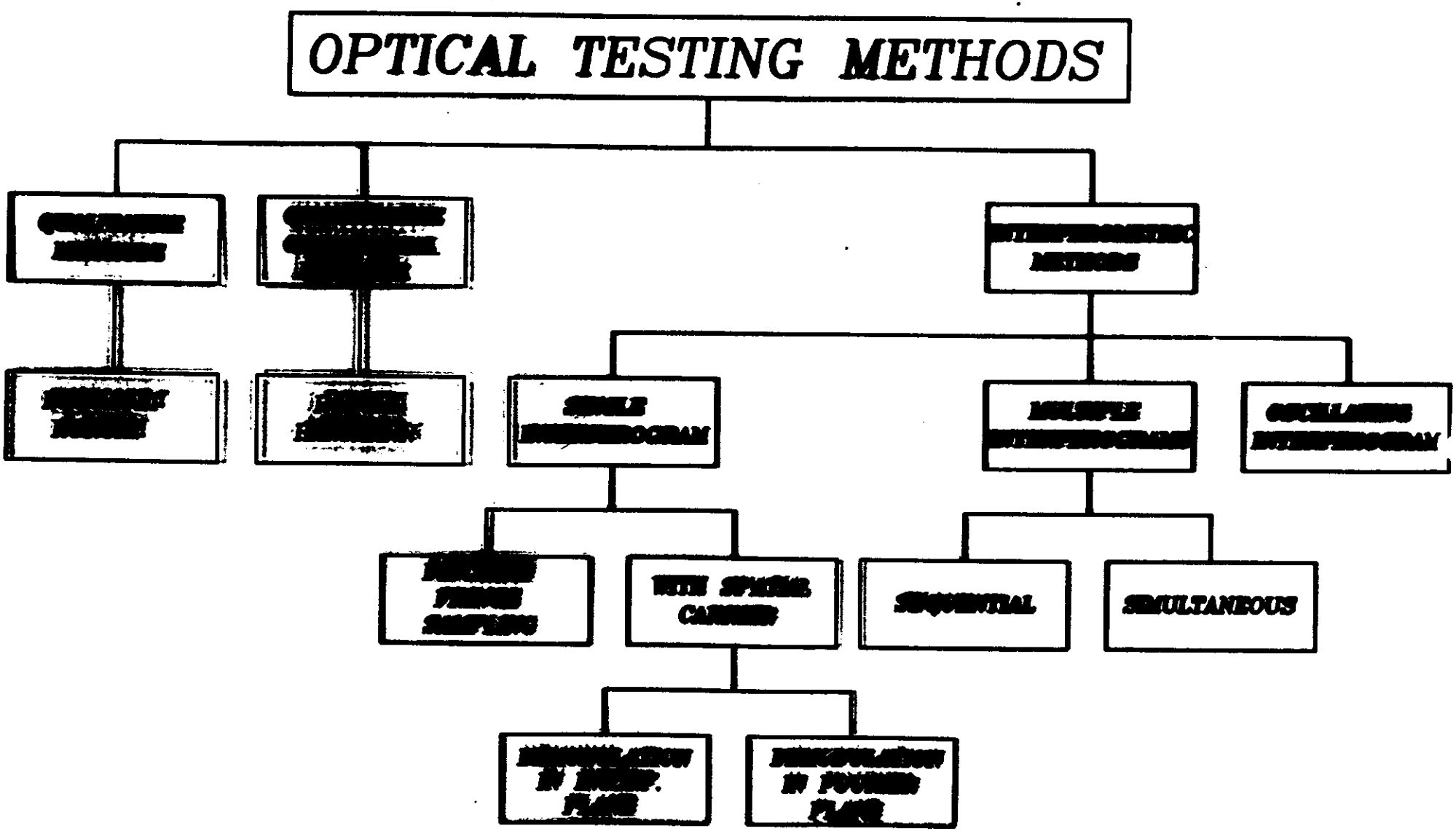
OPTICAL TESTING METHODS
SEQUENTIAL
SIMULTANEOUS

Interferometers without observable fringes

Jorge L. García-Márquez
Daniel Malacara-Hernández, FELLOW SPIE
Daniel Malacara-Doblado, MEMBER SPIE
Centro de Investigaciones en Optica A.C.
Apartado Postal 1-948
C.P. 37000, León Gto., México

Abstract. There are some optical arrangements that closely resemble interferometric configurations but do not produce fringe patterns. An important characteristic of these devices is that they do not have two different outputs with complementary patterns, but only one. Some of these interferometers are described here, pointing out their common properties and differences. It is shown that if we open the second output, both complementary patterns will appear. © *1997 Society of Photo-Optical Instrumentation Engineers.* [S0091-3286(97)02710-4]

Subject terms: interferometry; fringe patterns; cyclic interferometers; polarization.

Paper 05106 received Oct. 2, 1996; revised manuscript received May 29, 1997; accepted for publication May 29, 1997. This paper is a revision of a paper presented at the SPIE international conference on Optical Fabrication and Testing, June 1995, Tokyo, Japan. The paper presented there appears (unrefereed) in SPIE Proceedings Vol. 2576.

1 Introduction

It is well known that any two-beam interferometer produces two complementary interference patterns, i.e., a bright fringe in one of the interference patterns corresponds to a dark fringe in the other. The reason for this complementarily lies in the principle of energy conservation. Obviously, if only one pattern exists, it is really the superposition of both complementary patterns and hence the field must actually be fringe-free. Sometimes, the presence of one of the two fringe patterns is not obvious, but even then, its presence is sufficient to guarantee the existence of the fringes in the main pattern.

There are some optical arrangements closely resembling interferometric configurations that have only one output. These instruments, however, do not produce fringe patterns. An important characteristic of these devices is that they do not have two different outputs with complementary patterns, but only one, as we pointed out before. Here, we describe some of these instruments, which we call noninterferometers.

2 Cyclic Interferometers

The first example has a cyclic configuration, described by Cervantes.[1] In Figs. 1(a) and 1(b) two similar cyclic configurations are illustrated, where a collimated wavefront with amplitude a enters the interferometer. We see that there is only one output, that is, only one interference pattern.

We show that this interferometer may take on several different but equivalent configurations based in a generalized Fabry-Perot interferometer with the two mirrors having different reflection coefficients.

The amplitude E in the cyclic interferometer in Fig. 1 may be obtained as the sum of all the multiple reflected beams as follows:

$$E = ar + a\tau tt' e^{i\phi} + a\tau^2 tt' r' e^{2i\phi} + a\tau^3 tt' r'^2 e^{3i\phi} + a\tau^4 tt' r'^3 e^{4i\phi} + \cdots , \tag{1}$$

where ϕ is the phase difference introduced in every cycle. An optical element with amplitude transmission coefficient τ is inserted in the optical path. Here, r is the amplitude reflectivity for external reflection, r' is the amplitude reflectivity for internal reflection in the beamsplitter, and t is the amplitude transmitted from the air into the beamsplitter. After some algebraic manipulations we may obtain the following result for the amplitude in the output beam of the interferometer:

$$E = ar + \frac{a\tau tt' e^{i\phi}}{1 - \tau r' e^{i\phi}}. \tag{2}$$

If we assume that there are no absorption losses in the beamsplitters, we may use Stokes's relationships

$$r^2 + tt' = 1 \tag{3}$$

and

$$r = -r' \tag{4}$$

Hence, the amplitude of the output beams becomes

$$E = \frac{ar + a\tau r^2 e^{i\phi} + a(1 - r^2)\tau e^{i\phi}}{1 + \tau r e^{i\phi}} = a\,\frac{r + \tau e^{i\phi}}{1 + \tau r e^{i\phi}}. \tag{5}$$

Multiplying this equation by its conjugated complex E^*, the irradiance on the output field is

$$I = \frac{a^2 (r + \tau e^{i\phi})(r + \tau e^{-i\phi})}{(1 + \tau r e^{i\phi})(1 + \tau r e^{-i\phi})}, \tag{6}$$

which may be transformed into

$$I = I_0\,\frac{(r - \tau)^2 + 2r\tau(1 + \cos\phi)}{(1 - r\tau)^2 + 2r\tau(1 + \cos\phi)}, \tag{7}$$

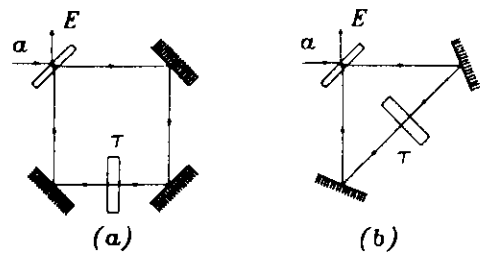

Fig. 1 Two possible cyclic interferometer configurations.

where $I_0=a^2$. Alternatively,

$$I=I_0\,\frac{(r+\tau)^2-4r\tau\,\sin^2(\phi/2)}{(1+r\tau)^2-4r\tau\,\sin^2(\phi/2)}. \tag{8}$$

It should be pointed out that this result is valid only for a system with nonabsorbing beamsplitter[1] and mirrors. However, any absorbing or reflecting element with transmission τ can be included the system.

Plots of the irradiance versus the phase are shown in Fig. 2 for $\tau=0.5$, 0.7, 0.9 and, 1.0. Here, we may notice the following interesting facts:

1. The fringes disappear for the extreme values of τ, equal to zero and one.
2. The dark fringes width is reduced when increasing the value of τ.

Figure 3 shows plots of the real versus the imaginary part of the reflectivity. It is interesting to see that these graphs are circles whose diameter represents the variation between the minimum and maximum amplitudes in the fringe pattern. If the beamsplitter reflectance increases, the circle decreases in diameter and shifts toward the edge of the largest (unit-radius) circle. This means that the interferometer reflectance becomes unity. We may also notice that for values of τ equal to r the circle passes through the center, making the irradiance equal to zero.

Considering a particular case with the irradiance transmission coefficient τ equal to one, we obtain

$$I=a^2\,\frac{r^2+1+2r\,\cos\,\phi}{r^2+1+2r\,\cos\,\phi}=a^2. \tag{9}$$

As we see, in this case the irradiance in the interference pattern is a constant, equal to the irradiance in the incident beam. That is, the interferometer acts as a perfect mirror, just introducing a phase shift. If an absorbing beamsplitter is used, a fringe pattern appears. The complementary pat-

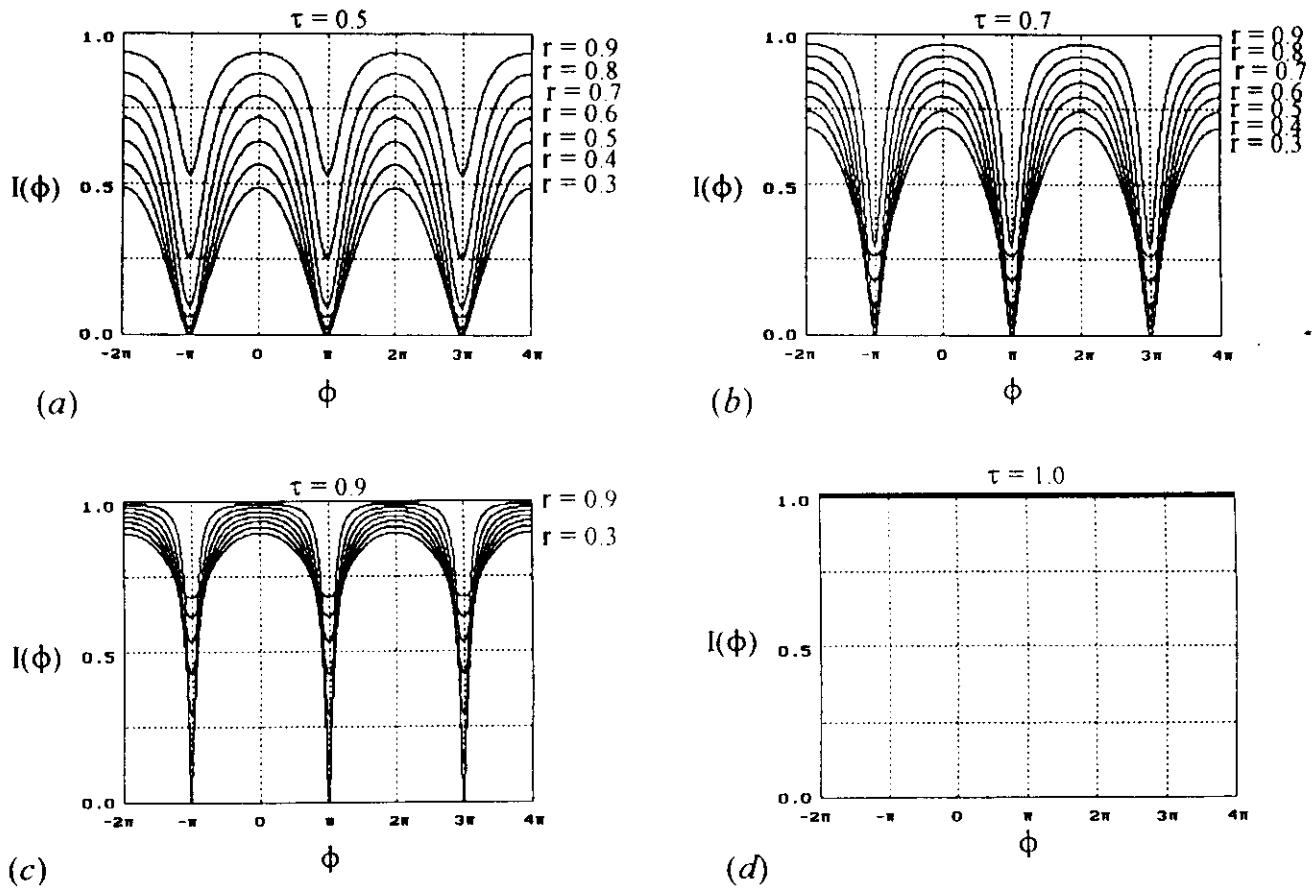

Fig. 2 Plots of the irradiance versus ϕ for several values of r and τ.

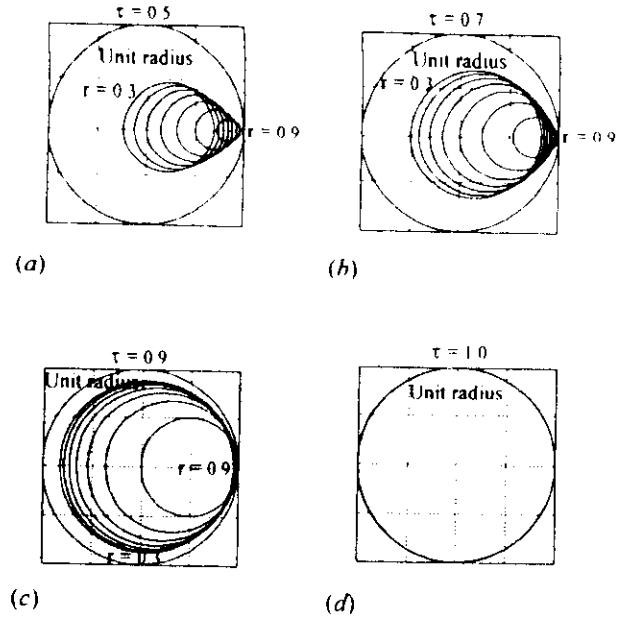

Fig. 3 Graphs in the complex plane showing the irradiance for several values of r and τ. The imaginary versus the real part of Eq. (5) has been plotted.

tern is absorbed in the beamsplitter. A plot of the intensity versus the phase is shown in the Fig. 2(d) for $\tau = 1.0$.

In Fig. 4 a plot of the maximum and minimum irradiance as a function of the reflectivity and the transmission coefficients is presented. When r and τ take the same value, the plot for I_{min} goes to zero. Both the minimum and the maximum irradiances start at the same value and join at the same place when the transmission value is 1.0. In Fig. 5, the visibility versus the transmission coefficient it is plotted; the visibility of our configuration takes its maximum value for identical values of the reflectance r and the amplitude transmission τ. The visibility decreases in all other cases.

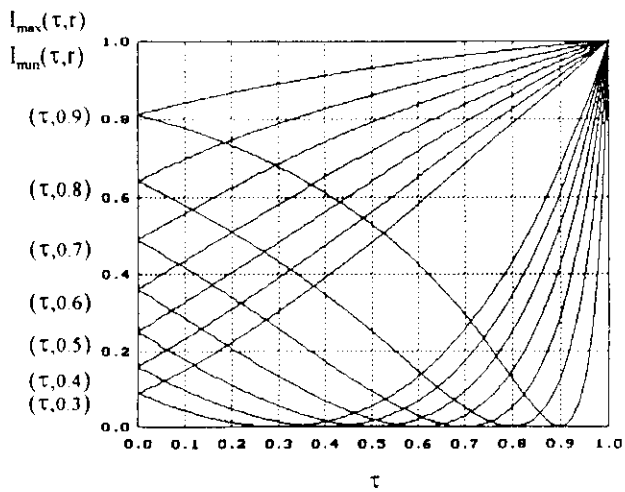

Fig. 4 Plots of the maximum and minimum irradiances as functions of the reflectivity and the transmission coefficients.

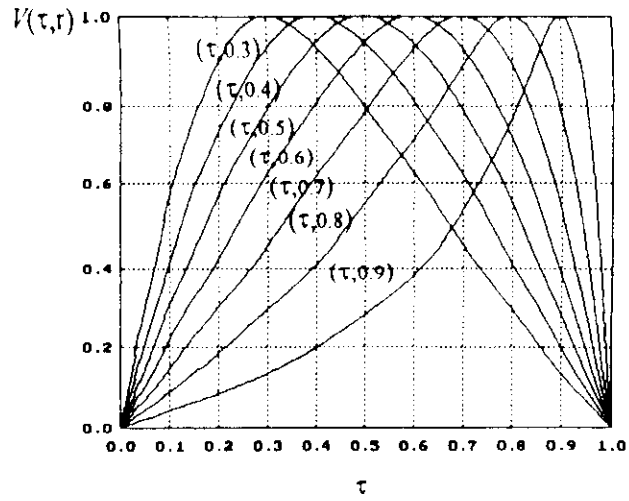

Fig. 5 Plots of the visibility versus the transmittance of the internal element.

The internal element with transmission coefficient τ introduces losses in the system, allowing the interferometer to have two outputs, and hence two complementary interferometric patterns. In this case the complementary pattern is in this absorbing element. It can in principle be made visible if the absorbed energy in this element is transformed by any means into visible light.

A simpler manner to make the complementary pattern observable is by introducing losses in one of the mirrors by making it partially reflective, as in Fig. 6. In this case Eqs. (7) and (8) are still valid if we write $\tau = -r_2$. The minus sign is introduced because the phase shifts upon reflection

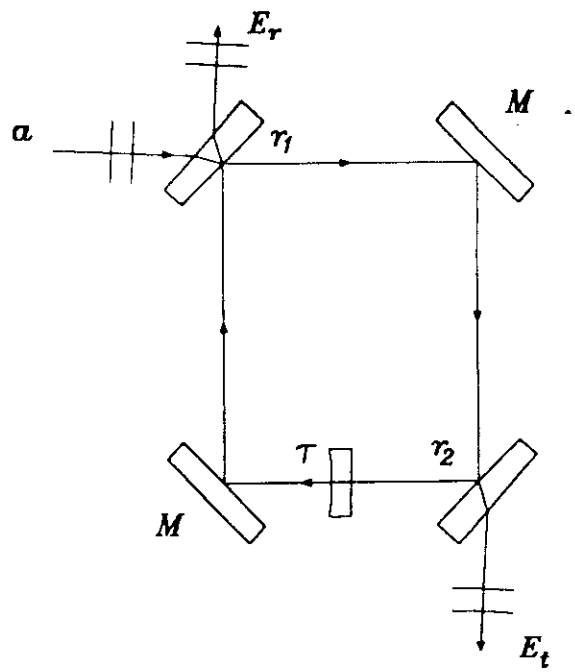

Fig. 6 Cyclic interferometer with two outputs.

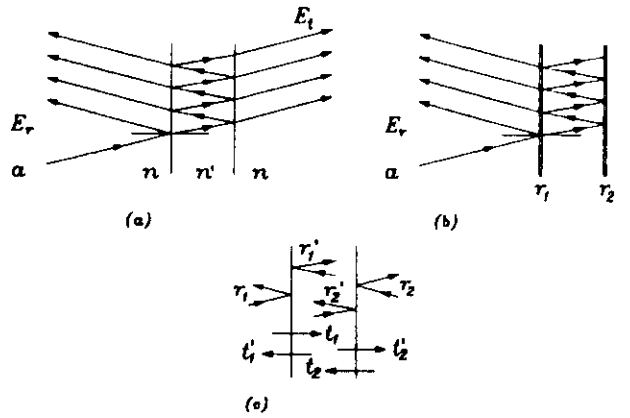

Fig. 7 Fabry-Perot interferometer with different reflection coefficients.

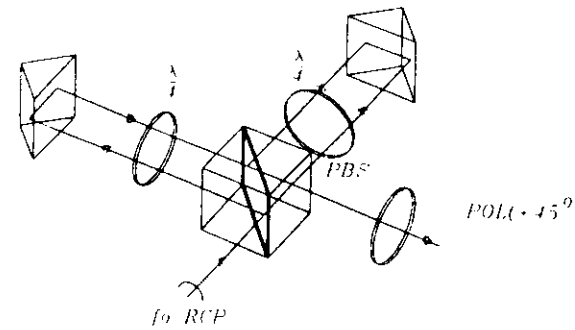

Fig. 8 Another interferometric configuration that uses the polarization states of the light and does not produce fringe patterns.

for r_1 and r_2 are 0 for one of them and 180 deg for the other, because one is an internal reflection and the other is an external reflection.

3 Fabry-Perot Interferometer versus Cyclic Interferometers

This cyclic interferometer with two outputs reminds us of a Fabry-Perot interferometer with two different amplitude reflection coefficients, as in Fig. 7. We now find the reflected and transmitted patterns for this modified Fabry-Perot interferometer using two different amplitude reflection coefficients.

Following the notation in Fig. 7(c), the expressions for the reflected irradiances in the interferometer may be found by using Stoke's relations to be

$$I_r = I_0 \frac{(r_1 - r_2)^2 + 4r_1 r_2 \sin^2(\phi/2)}{(1 - r_1 r_2)^2 + 4r_1 r_2 \sin^2(\phi/2)}, \tag{10}$$

where I_0 is the incident irradiance and ϕ is the phase difference for two consecutive reflections. In an analogous manner, the transmitted irradiance is found to be

$$I_t = I_0 \frac{(t_1 t_2')^2}{(1 - r_1 r_2)^2 + 4r_1 r_2 \sin^2(\phi/2)}. \tag{11}$$

Now, since all surfaces are dielectric, the transmitted irradiance plus the reflected irradiance should equal the incident irradiance; hence we may find

$$I_t = I_0 \frac{1 - r_1^2 - r_2^2 + (r_1 r_2)^2}{(1 - r_1 r_2)^2 + 4r_1 r_2 \sin^2(\phi/2)}. \tag{12}$$

If we compare the result in Eq. (10) for the Fabry-Perot interferometer with Eq. (8) for the cyclic interferometer, we see that the two irradiances become identical if we make the substitutions $r = r_1$ and $\tau = -r_2$.

4 Polarizing Interferometers

Another example in which no fringe pattern appears is the well-known[2] interferometer configuration shown in Fig. 8. The incident beam is right circularly polarized. Again, as in the preceding example, there is only one interference pattern. No complementary pattern exists. The two interfering beams w_1 and w_2 are linearly and orthogonally polarized as shown in Fig. 9, so that no interference can occur.

If a polarizing filter is placed in the beam with its axis along the direction P as illustrated in Fig. 9, the components of w_1 and w_2 along P will interfere, forming the interferogram. If the filter is rotated to have its axis in a direction P', the complementary pattern appears. Thus, we might say that without the polarizing filter no fringe pattern is observed, because the two complementary orthogonally polarized patterns overlap in the same direction of observation. With the filter, the two complementary patterns are separated by absorbing the energy of one in the filter. If a nonabsorbing polarizing prism is used instead of the filter, the two complementary patterns may be observed.

5 Conclusions

We have described some examples in which the interferometric systems do not produce fringes, because there is only one output beam. In this case there is no complementary pattern. So, in order to have a fringe pattern in the cyclic interferometer, one of following conditions should be satisfied:

1. There is a real output.
2. If not, the output should be through absorption (i.e., an absorptive element).

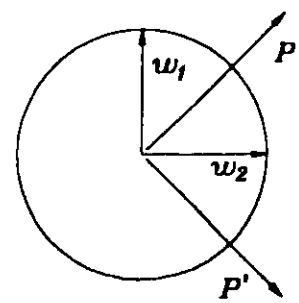

Fig. 9 Axis of rotation for a polarizing filter.

We have obtained some important relations between the Fabry-Perot and the cyclic interferometers. From Fig. 6 it can be observed that the light beam follows only one direction in both possible path, but in the Fabry-Perot interferometer (Fig. 7) it travels the same path in both directions. Another requirement is that in both interferometers the reflection coefficient r_2 should be different from one in order to have fringes (or an absorbing element).

The main practical difference between the cyclic and the Fabry-Perot interferometers is the same as between the Mach-Zehnder and the Twyman-Green interferometers, i.e., that in the first the tested sample is traversed only in one direction by the light, while in the second, it is traversed in both directions.

Acknowledgments

The authors wish to acknowledge the financial support of CONACyT.

References

1. M. Cervantes, "Multiple-beam cyclic interferometer," *Appl. Opt.* 27, 1952–1956 (1988).
2. J. Z. Malacara, "Angle, distance, curvature, and focal length measurements," Chapter 18 in *Optical Shop Testing*, D. Malacara, Ed., Wiley New York, 1992.

Jorge L. García-Márquez received his BE in electronic engineering from the Universidad Iberoamericana León in 1992, and his MSc degree in optics from the Centro de Investigaciones en Optica-Universidad de Guanajuato in 1995. Since then he has been a research assistant. His research interests are optical design and interferometry. He is currently pursuing a PhD degree in optical sciences at the Centro de Investigaciones en Optica.

Daniel Malacara-Hernández received his BSc in physics in 1961 from the Universidad Nacional Autonoma de Mexico and his PhD in optics in 1965 from the University of Rochester, New York. He then joined the Institute of Astronomy of the National University of Mexico and in 1972 in Instituto Nacional de Astrofisica, Optica y Electrónica. In 1980 the Centro de Investigaciones en Optica was created, and he became its first general director, a position he held from 1980 to 1989. He has been the author or editor of several books on optics; the best known is *Optical Shop Testing*. He has published more than 100 papers in well-known optics journals. He is a fellow of the OSA and SPIE, is a topical editor for *Applied Optics*, and has been on many international scientific committees. In 1986 he received the National Prize for Technology in Mexico.

Daniel Malacara-Doblado received a BS degree in electronic engineering from the Universidad Iberoamericana in Leon, México, in 1992. He received his MS in optics from the Centro de Investigaciones en Optica, in León, México. Now he is working on his PhD thesis. He is interested in Talbot interferometry and optical metrology. He is a member of the Sociedad Mexicana de Fisica and a member of SPIE.

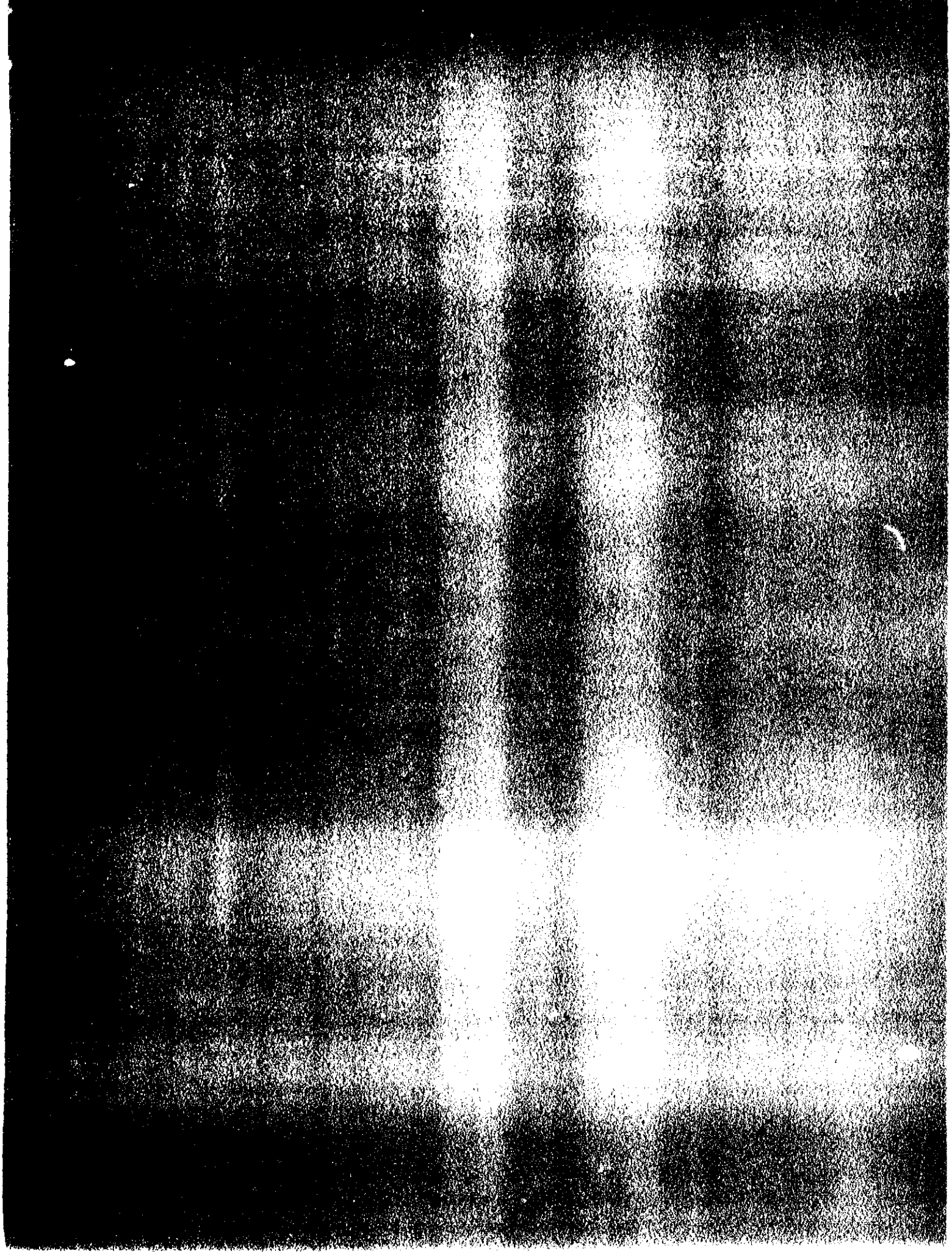

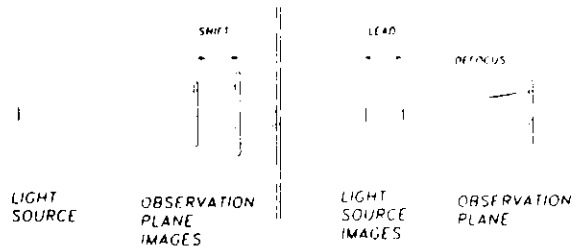

Fig. 10. Point in the observing plane that is illuminated by a light ray from a point source, in an interferometer with pure shift.

When the light source is extended and there is shift or any kind of shear, then the two images of the observing plane are separated in space as shown in Fig. 11. As we pointed out above, this effect reduces the interference pattern contrast. The maximum contrast with an extended light source is thus obtained when there is no shift and no shear. This is the same as saying that the two images of the light source must coincide in space and must also be perfectly coplanar to each other. Using this fact, Guild[3] proposed a method to verify the compensation for the size of the light source in a Twyman–Green interferometer by eliminating the equal inclination fringes that are observed when one looks at the spatially separated images of the light source. An exact compensation for the light source size may be obtained only if the two light source images not only coincide in space but also have the same size and orientation to avoid the presence of any kind of shear. This condition may be satisfied by use of many methods. Connes[4] proposed the use of adjustable telescopic compensators in a Michelson interferometer, and Steel[5] used thin-field lenses placed at the light source images.

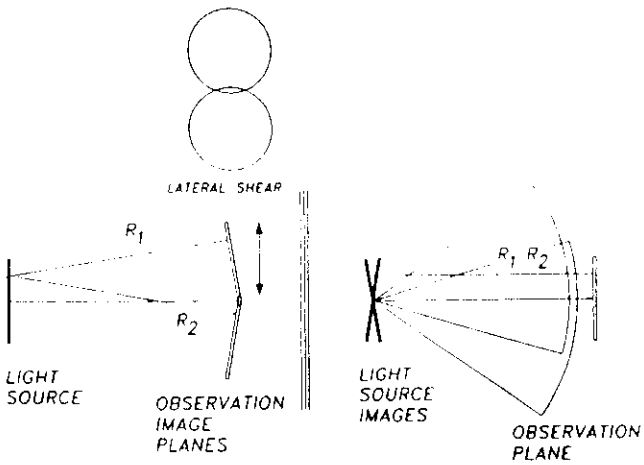

Fig. 11. Point in the observing plane that is illuminated by two different light rays from the same point in the light source.

4. Light Source Monochromaticity

The OPD is an interferometer parameter that is independent of the other four. It is given by[1]

$$\mathrm{OPD} = \sum_{1} nd - \sum_{2} nd = \sum_{12} nd. \tag{16}$$

This relative OPD is independent of the wavelength when $d\mathrm{OPD}/d\lambda = 0$; thus we obtain

$$\sum_{1} \bar{N}t = \sum_{2} \bar{N}t, \tag{17}$$

where $\bar{N}$ is the group refractive index defined by

$$\bar{N} = N - \lambda \frac{dN}{d\lambda}. \tag{18}$$

Therefore the interferometer compensates for the bandwidth $\Delta\lambda$ when the group optical path for both interferometer paths is the same. A particular case is when both paths travel the same distances, with the same amount and type of glass on both paths. White-light fringes may be observed only if the interferometer is perfectly compensated for the whole visible spectrum.

5. Conclusions

Four parameters, shift, shear, lead, and tilt, have been defined in an analogous but slightly different manner from those defined by Steel.[1] The effect of each of these parameters in a practical interferometer has been analyzed. As pointed out by Steel,[1] if the interferometer is made out of plane mirrors and thin or nondispersive plane beam splitters, without any lens or spherical mirror or glass plate, then the shift, lead, and OPD are all equal. These three parameters are equal even with glass plates, as long as the glass in both paths is the same. This forms what is known as a compensated interferometer. However, if the glass path is not the same for both beams, then the OPD is different from the shift and lead. If there are lenses or spherical mirrors in the interferometers, the shift, lead, and OPD are generally different.

References

1. W. H. Steel, *Interferometry*, 2nd ed. (Cambridge U. Press, New York, 1983), p. 90.
2. G. Hansen, "Die sichtbarkeit der interferenzen beim Twyman interferometer," Optik **12**, 5 (1955).
3. J. Guild, "Fringe systems in uncompensated interferometers," Proc. Phys. Soc. London **33**, 40 (1920–1921).
4. P. Connes, "Aumentation du produit luminosité x resolution des interferometers par l'emploie d'une difference de marche independente de l'incidence," Rev. Opt. **35**, 37 (1956).
5. L. Steel, "The compensation of a Williams interferometer," Opt. Acta **10**, 205–208 (1963).

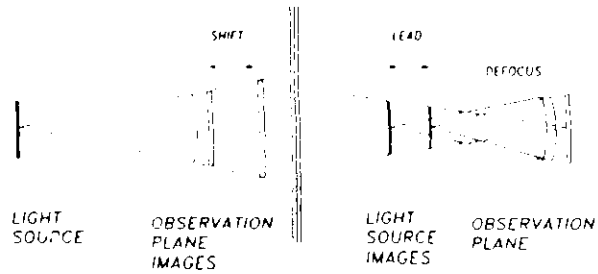

Fig. 8. Interferometer with pure defocusing.

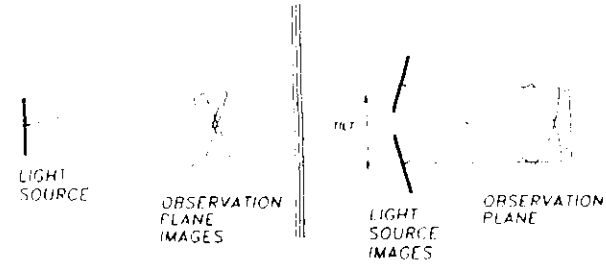

Fig. 9. Interferometer with pure tilt.

other. If the light source is small compared with its distance to the observation plane images, then the interferometer produces two reversal sheared wave fronts.

If there are only lead and shift (shear = tilt = 0) in the interferometer, the light source is small compared with its distance from the images of the observation plane, and at least one of the two images of the light source is at a finite distance, then both radial shear and defocusing are present. In the case of pure defocusing as shown in Fig. 8,

$$\frac{\beta}{\alpha} = \frac{\delta}{\gamma} = 1. \tag{13}$$

The presence of defocusing implies the presence of lead; however, the converse is not necessarily true because the two images of the light source might be separated, but at infinity.

If there is no lead and no shear, besides Eq. (13) we may also write

$$\alpha_2' = \beta_1', \tag{14}$$

$$\delta_2' = \gamma_1'. \tag{15}$$

This result means that when the two images of the light source coincide in spatial position, size, and orientation, then the two images of the observing plane must also coincide in spatial position and size. In other words, it is impossible to have a shift value different from zero if the lead is zero, unless there is a radial shear value that is different from zero.

If the two images of the light source are laterally displaced with respect to each other and with the perpendiculars pointing to the center of the observing plane, as in Fig. 9, then the interferometer has pure tilt. In this case the two images of the observation plane are located one over the other and have the same size, but one is tilted with respect to the other.

Table 2 shows the effect of these parameters on the configuration of the interferometer. The column labeled interferometer parameters lists only those different from zero.

3. Light Source Size

Let us consider first the case of an extremely small light source, as in Fig. 10. If there is pure shift, a ray from the light source illuminates the same point on the two images of the observation plane; then there are no spatial coherence problems. If there is any kind of shear, however, spatial coherence problems may appear even with a point source, because the two images of the observing plane will be separated in space. Thus any given point in the observing plane will be illuminated by two different rays, coming from a given point in the light source but with different directions. The greater the angle between these rays the smaller the degree of coherence between them. This effect reduces the interference pattern contrast.

Table 2. Effect of the Interferometer Parameters on the Interferometer Configuration

Interferometer		Images	
Operation	Parameter	Observing Plane	Light Source
Tilt	Tilt	Same size, laterally separated along arc	Same position and size, tilted with respect to each other
Defocusing	Lead shift	Longitudinally displaced, same angular size	Longitudinally displaced, same angular size
Shear			
Radial	Shift shear (radial)	Different position, ratio of angular sizes = ρ	Same position, different sizes, with ratio = ρ
Rotational	Shear (rotational)	Same position and size, rotated with respect to each other	Same position and size, rotated with respect to each other
Reversal	Shear (reversal)	Same size and position, reversed with respect to each other	Same position and size, reversed with respect to each other
Lateral	Shear (lateral)	Same position and size, tilted with respect to each other	Same size, laterally separated along arc

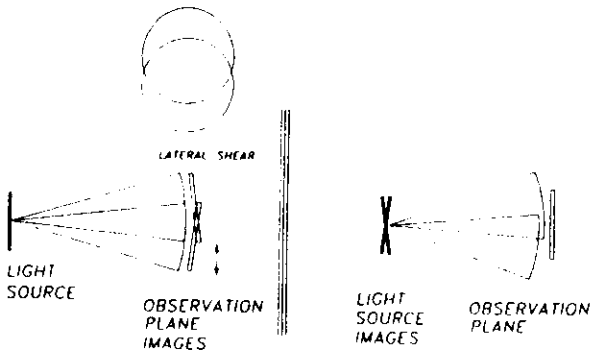

Fig. 4. Interferometer with pure lateral shear.

$$\frac{\alpha}{\beta} = \frac{E_2 G_2}{E_1 G_1} \frac{\delta_2'}{\gamma_1'}. \tag{10}$$

Then from the last two relations we find

$$\frac{\alpha}{\beta} = \frac{\delta}{\gamma} = \frac{\alpha_1'}{\beta_1'} = \frac{\delta_1'}{\gamma_1'}. \tag{11}$$

This result shows that the angular sizes of the images of the observation plane, as seen from the light source, are always equal to the ratio of the angular sizes of the images of the light source as seen from the observing plane.

2. Interpretation of Interferometer Parameters

Let us now examine the effect of each of these parameters in a practical interferometer. The shear or lateral displacement of one of the images of the observation plane with respect to the other must be interpreted in a general manner. In other words, a lateral displacement may be present, but a size contraction of one image with respect to the other, an angular displacement, or an orientation change may also be present. One may perform an orientation change, for example, by reflecting one of the images of the observing plane upside down and vice versa, while leaving the left and right sides unchanged.

In a lateral shear interferometer the two images of the observation plane are placed with respect to each other as in Fig. 4. The two images of the light source are then one over the other in the same place with the same size, but they are tilted with respect to each other. A point on the observation plane is illuminated by rays with two different directions from the light source. Then if the light source is small compared with its distance to the observation plane images, the interferometer produces two laterally sheared wave fronts.

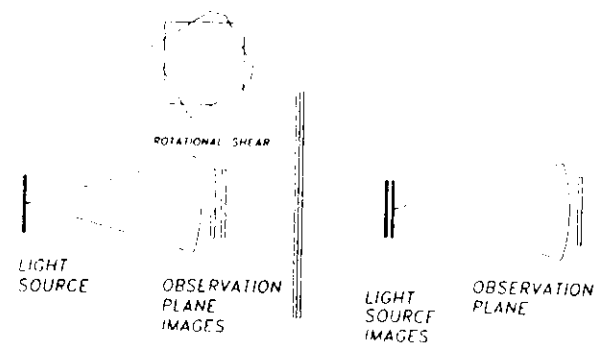

Fig. 6. Interferometer with pure rotational shear.

In a radial shear interferometer the two images of the light source have a different size but coincide at the same plane (lead = 0) as in Fig. 5. The two images of the observation plane have a ratio of their angular sizes, as seen from the light source, equal to radial shear ρ, as follows:

$$\rho = \frac{\beta}{\alpha} = \frac{\delta}{\gamma}. \tag{12}$$

As in a lateral shearing interferometer, if the light source is small compared with its distance to the observation plane images, then the interferometer produces two radially sheared wave fronts.

In a rotational shear interferometer the two images of the observation plane have the same size and coincide in the same plane, but one is rotated with respect to the other as in Fig. 6. The two images of the light source are also rotated one with respect to the other. If the light source is small compared with its distance to the observation plane images, then the interferometer produces two rotationally sheared wave fronts.

In a reversal shear interferometer the two images of the observation plane have the same size and coincide in the same plane, but one is reversed with respect to the other as in Fig. 7. The two images of the light source are also reversed with respect to each

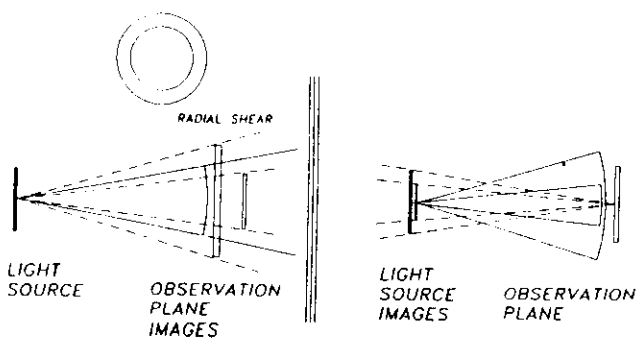

Fig. 5. Interferometer with pure radial shear.

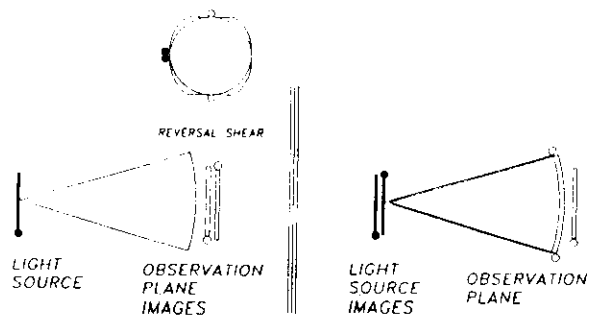

Fig. 7. Interferometer with pure reversal shear.

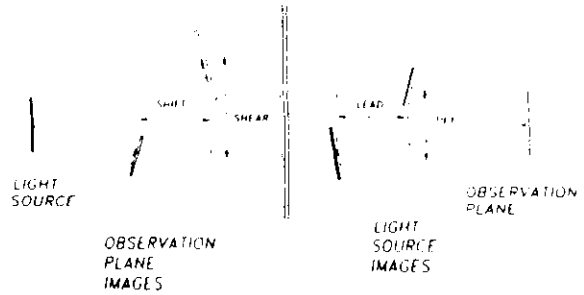

Fig. 2. Modified Steel's parameters for a general two-beam interferometer.

Table 1. Some Points and Ray Paths and Their Images

Object	Image 1	Image 2
Point	Point	Point
A	A_1	A_2
B_1	B	
C	C_1	C_2
E	E_1	E_2
F_1	F	
G	G_1	G_2
Ray	Ray	Ray
A–G_1	A_1–G	A_2–H
A–G_2	A_1–F	A_2–G
E–C_1	E_1–C	E_2–D
E–C_2	E_1–B	E_2–C

of wave fronts, because it is easier to visualize these parameters in terms of these rays. These considerations are completely general and valid for any two-beam interferometer, such as the Twyman–Green and the Fizeau interferometers.

Assuming now that the object medium and the observation plane medium have the same index of refraction, by the Lagrange relation that uses a paraxial approximation we may write for ray A–G_1 and its first image

$$AC\beta = A_1C_1\beta_1', \tag{1}$$

and for ray A–G_2 and its images

$$AC\alpha = A_1C_1\alpha_1' = A_2C_2\alpha_2'. \tag{2}$$

Now for ray E–C_1 and its first image we write

$$EG\gamma = E_1G_1\gamma_1', \tag{3}$$

and for ray E–C_2 and its images we write

$$EG\delta = E_1G_1\delta_1' = E_2G_2\delta_2'. \tag{4}$$

From Eqs. (1) and (2) we obtain

$$\frac{\alpha}{\beta} = \frac{\alpha_1'}{\beta_1'}, \tag{5}$$

$$\frac{A_1C_1}{A_2C_2} = \frac{\alpha_2'}{\alpha_1'}. \tag{6}$$

Similarly, from Eqs. (3) and (4) we obtain

$$\frac{\delta}{\gamma} = \frac{\delta_1'}{\gamma_1'}, \tag{7}$$

$$\frac{E_1G_1}{E_2G_2} = \frac{\delta_2'}{\delta_1'}. \tag{8}$$

From an analysis of Fig. 3 we may also find

$$\frac{\delta}{\gamma} = \frac{A_2C_2}{A_1C_1}\frac{\alpha_2'}{\beta_1'}, \tag{9}$$

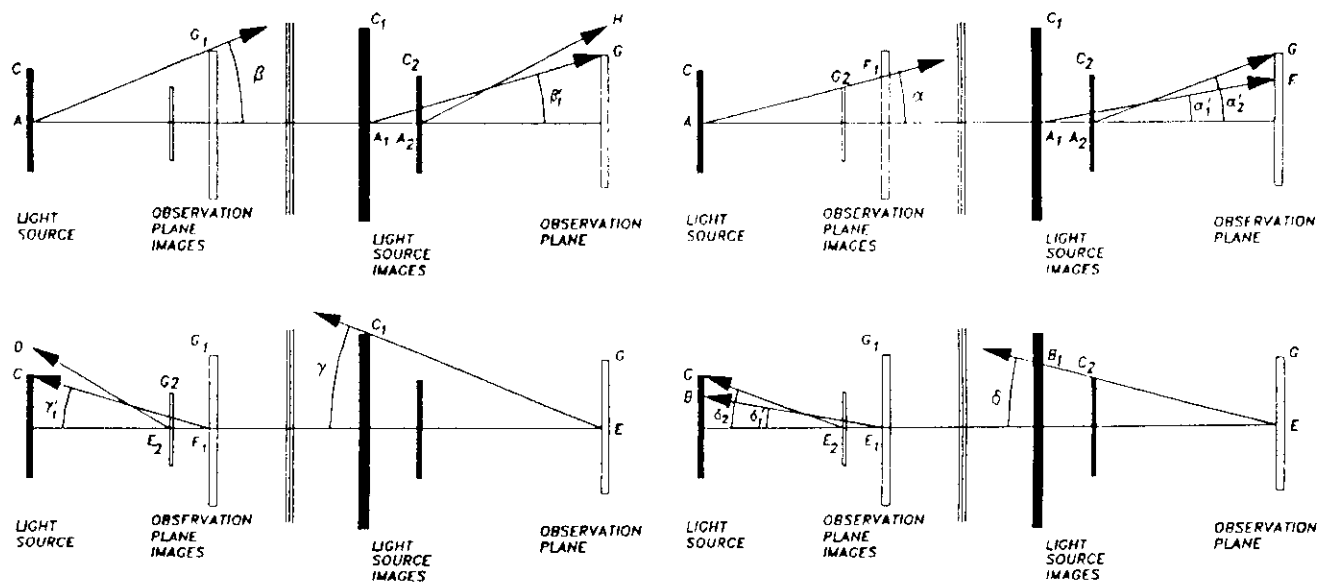

Fig. 3. Relative sizes and positions in a two-beam interferometer for the light source, the observation plane, and their images.

First-order parameters for a general two-beam interferometer

Ian A. Walmsley and Daniel Malacara

We formulate the first-order properties of a general two-beam interferometer. We show that it may be completely described by the light source position and the location, orientation, and size of the two images of this light source as seen from the observation plane, plus the image-plane position and the location, orientation, and size of the two images of this observation screen as seen from the light source position, plus the optical path difference between the two possible optical paths. The parameters are quite similar to those previously defined by Steel [W. H. Steel, *Interferometry*, 2nd ed. (Cambridge U. Press, New York, 1983)].

1. Introduction

The first-order properties of a general two-beam amplitude-division interferometer may be completely described by the light source position and the location, orientation, and size of the two images of this light source as seen from the observation plane, plus the image-plane position and the location, orientation, and size of the two images of this observation screen as seen from the light source position, plus the optical path difference between the two possible optical paths. Steel[1] showed, based on an earlier study by Hansen,[2] that four parameters could be defined by the positions of these images. These parameters are shear, shift, tilt, and lead. As shown in Fig. 1, shear S is the lateral separation of the two images of the observation plane, and shift h is their longitudinal separation. Tilt t is the lateral separation of the two images of the light source, and lead l is their longitudinal separation. As Steel pointed out, a fifth independent parameter is the optical path difference (OPD).

Here we propose a slightly different definition for these parameters, including tilts and sizes of these images, to make them more closely associated with practical interferometer parameters. We show that it is convenient to define these parameters as in Fig. 2. The perpendicular lines passing through the centers of the images of the observation plane pass through the center of the light source. Similarly, the perpendicular lines passing through the centers of the images of the light source pass through the center of the observation plane. The size of the images of the observation plane is directly proportional to their distance from the center of the light source. In addition, the size of the images of the light source is directly proportional to their distance from the center of the observation plane. The first four interferometer parameters are clearly illustrated in this figure. It is obvious that these modified parameters reduce to Steel's parameters when both the light source and the observation plane are at infinity.

To understand the way in which these parameters are related, let us consider an interferometer in which both the shear and the tilt are zero (see Fig. 3). There are two images of the light source and two images of the observation plane, with different points and ray paths imaged as in Table 1. Here we have considered the paths for some important rays instead

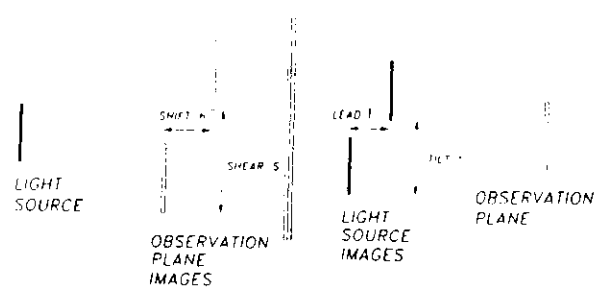

Fig. 1. Steel's parameters for a general two-beam interferometer.

I. A. Walmsley is with The Institute of Optics, University of Rochester, Rochester, New York 14627. D. Malacara is with the Centro de Investigaciones en Optica, A. C., Apartado Postal 948, 37000 Leon, Gto. Mexico.

Received 24 January 1994; revised manuscript received 31 August 1994.

0003-6935/95/193571-05$06.00/0.

Murty, M. V. R. K., Some modifications of Jamin interferometer useful in optical testing. *Appl. Optics*, **3** (1964) 535.

Francon, M., Polarization apparatus for interference microscopy of isotropic transparent objects. *J. Opt. Soc. Am.*, **47** (1967) 528.

Saunders, J. B., A simple inexpensive wavefront shearing interferometer. *Appl. Opt.*, **6** (1967) 1581.

Murty, M. V. R. K., Interferometry applied to testing of optics. *Bull. Opt. Soc. India*, **1** (1967) 33.

Lohmann, A. & Bryndahl, O., A lateral wavefront shearing interferometer with variable shear. *Appl. Optics*, **6** (1967) 1934.

Van Rooyen, E., Design for a variable shear prism interferometer. *Appl. Optics*, **7** (1968) 2423.

Briers, J. D., Prism shearing interferometer. *Opt. Technol.*, **1** (1969) 196.

Van Rooyen, E. & Van Houten, A. G., Design of a wavefront shearing interferometer useful for testing large aperture optical systems. *Appl. Optics*, **8** (1969) 19.

Murty, M. V. R. K., A compact lateral shearing interferometer based on the michelson interferometer. *Appl. Optics*, **9** (1970) 1146.

Kelly, J. C. & Hargreaves, R. A., A rugged inexpensive shearing interferometer. *Appl. Optics*, **9** (1970) 948.

Nyssonen, D. & Jerke, J. M., Lens testing with a simple wavefront shearing interferometer. *Appl. Optics*, **12** (1973) 2061.

Hariharan, P., Simple laser interferometer with variable shear and tilt. *Appl. Optics*, **14** (1976) 1056.

28. Sirohi, R. S. & Kothiyal, M. P., Double wedge plate shearing interferometer for collimation test. *Appl. Optics*, **26** (1987) 4054.
29. Kothiyal, M. P., Sirohi, R. S. & Rosenbruch, K. J., Improved techniques of collimation testing. *Opt. Laser Technol.*, **20** (1988) 139.
30. Sriram, K. V., Kothiyal, M. P. & Sirohi, R. S., Self-referencing collimation testing techniques. *Opt. Engng*, **32** (1993) 94.
31. Sriram, K. V., Senthilkumaran, P., Kothiyal, M. P. & Sirohi, R. S., Double-wedge-plate interferometer for collimation testing: New configurations. *Opt. Engng*, **32** (1993) 94.
32. Langenbeck, P., Improved collimation test. *Appl. Optics*, **9** (1970) 2590.
32a. Malacara, D., Testing of optical surfaces. Ph.D. Thesis, Institute of Optics, University of Rochester, New York, 1965.
33. Gouhua, L., Mingshan, Z. & Jingbin, Z., Improved wedge-plate shearing interferometric technique for a collimation test. *Appl. Optics*, **31** (1992) 4363.
34. Malacara, D. & Harris, O., Interferometric measurement of angles. *Appl. Optics*, **9** (1970) 1630.
35. Tentori, D. & Celaya, M., Continuous angle measurement with a Jamin interferometer. *Appl. Optics*, **25** (1986) 2.
36. Srivastava, S. N., Tomar, M. S. & Kasana, R. S., Determination of the linear thermal expansion coefficient of long metallic bars by Murty shearing interferometer. *Opt. Technol.*, **22** (1990), 283.

General references on lateral shearing interferometers (In chronological order)

Lenouvel, L. & Lenouvel, F., Etude des faisceaux convergents (convergent beams study). *Rev. Opt. Theor. Instrum.*, **17** (1938) 350.
Bates, W. J., A wavefront shearing interferometer. *Proc. Phys. Soc. (Lond.)*, **59** (1947) 940.
Drew, R. L., A simplified shearing interferometer. *Proc. Phys. Soc. (Lond.)*, **864** (1951) 1005.
Francon, M., *Progress in Microscopy*. Pergamon Press, New York, 1951, p. 150.
Brown, D. S., The application of shearing interferometry to routine optical testing. *J. Sci. Instrum.*, **32** (1955) 137.
Baker, J., An interferometer for measuring the spatial frequency response of a lens system. *Proc. Phys. Soc. (Lond.)*, **868** (1955) 871.
Gates, J. W., Reverse shearing interferometry. *Nature*, **176** (1955) 359.
Nomarski, G., Microinterférométrie interféretiel á ondes polarizées. *J. Phys. Radium*, **16** (1955) 9(S).
Smith, F. H., In *Modern Methods of Microscopy*. Butterworths, London, 1956, p. 76.
Hariharan, P. & Sen, D., Cyclic shearing interferometer. *J. Scient. Instrum.*, **37** (1960) 340.
Saunders, J. B., Wavefront shearing prism interferometer. *J. Res. Nat. Bur Stand.*, **68C** (1964) 155.

1: The wavefront shearing interferometer. *J. Res. Nat. Bur. Stand. Sect. B*, **65** (1961) 239.

10. Murty, M. V. R. K. & Malacara-Hernandez, D., Some applications of the gas laser as a source of light for the testing of optical systems. *Jpn J. Appl. Phys. (Japan)*, **4** (1965) 106.

10a. Murty, M. V. R. K. & Shukla, R. P., Measurement of long radius of curvature. *Opt. Engng*, **22** (1983) 231.

11. Dutton, D., Cornejo, A. & Latta, M., A semiautomatic method for interpreting shearing interferograms. *Appl. Optics*, **7** (1968) 125.

12. Saunders, J. B. & Bruning, J. H., A new interferometric test and its applications to the 8 inch reflecting telescope at Kit Peak National Laboratory. *Astron. J.*, **73** (1968) 415.

13. Wyant, J. C., Double Frequency Grating Lateral Shearing Interferometer. *Appl. Optics*, **12** (1973) 2057.

14. Rimmer, M. P. & Wyant, J. C., Evaluation of large aberrations using a lateral shear interferometer having variable shear. *Appl. Optics*, **14** (1975) 142.

15. Saunders, J. B., A simple interferometric method for workshop testing of optics. *Appl. Optics*, **9** (1970) 1623.

16. Wyant, J. C. & Smith, F. P., Interferometer for measuring power distribution of opthalmic lenses. *Appl. Optics*, **14** (1975) 1607.

17. Riley, M. E. & Gusinow, M. A., Laser beam divergence utilizing a lateral shearing interferometer. *Appl. Optics*, **16** (1977) 2753.

18. Murty, M. V. R. K. & Shukla, R. P., Parallel plate interferometer for the precise measurement of radius of curvature of a test plate and focal length of a lens system. *Ind. J. Pure & Appl. Phys.*, **21** (1983) 587.

19. Kasana, R. S. & Rosenbrunch, K. J., Determination of the refractive index of a lens using the Murty shearing interferometer. *Appl. Optics*, **22** (1983a) 3526.

20. Kasana, R. S. & Rosenbrunch, K. J., The use of a plane parallel plate for determining the lens parameters. *Opt. Commun.*, **46** (1983b) 69.

21. Shukla, R. P., Perera, G. M., George, M. C. & Venkateswarlu, P., Determination of refractive index of a simple negative, positive or zero power lens using a wedged plate interferometer. *Appl. Optics*, **29** (1990) 4541.

22. Shukla, R. P., Measurement of refractive index of liquid or glass using Murty interferometer. *Indian J. Pure & Appl. Phys.*, **25** (1987) 90.

23. Shukla, R. P., Perera, G. M., George, M. C. & Venkateswarlu, P., Measurement of birefringence of optical materials using a wedged plate interferometer. *Opt. Commun.*, **78** (1990) 7.

24. Tanner, L. H., Some laser interferometers for use in fluid mechanics. *J Scient Instrum.*, **42** (1965) 834.

25. Tanner, L. H., The design of laser interferometer for use in fluid mechanics. *J. Scient. Instrum.*, **43** (1966) 878.

26. Taboada, J., Lateral shearing interferometric technique for transparency distortion analysis. *Appl. Optics*, **16** (1977) 2603.

27. Xu, D.-Y. & Rosenbruch, K. J., Rotatable single wedge plate shearing interference technique for collimation testing. *Opt. Engng*, **30** (1991) 391.

coefficient of thermal expansion is 3·5% for an aluminum rod of length equal to one meter in the temperature range 20–40 °C.

8 CONCLUSIONS

Several applications of the Murty interferometer were described in this article. The information presented in this review paper will be useful for workers engaged in the testing of optical systems and components.

ACKNOWLEDGMENTS

The authors thank Dr V. B. Kartha, Head, Spectroscopy Division, for his keen interest in the work. Thanks are also due to M. V. Mantravadi, Electronic Systems Division, 500E Orangethorpe Avenue, California, for going through the manuscript and valuable suggestions during the course of this work. Thanks are due to S. Bhattacharya for assistance in tracing the figures.

REFERENCES

1. Murty, M. V. R. K., The use of a single plane parallel plate as a lateral shearing interferometer with a visible gas laser source. *Appl. Optics*, **3** (1964) 531.
2. De Vany, A. S., Using a Murty interferometer for testing the homogeneity of test samples of optical materials. *Appl. Optics*, **10** (1971) 1459.
3. De Vany, A. S., Scanning Murty interferometer for optical testing. *Appl. Optics*, **11** (1972) 1467.
4. Dickey, F. M. & Harder, T. M., Shearing plate optical alignment. *Opt. Engng*, **17** (1978) 295.
5. Xu, D.-Y., Plate lateral shearing interferometer. In *Shearing Interferometers and Their Applications*. Beijing Mechanics Industry House, 1987, pp. 164–206.
6. Mantravadi, M., Personal communication, 1992. (Former name: M.V.R.K. Murty.)

6a. Mantravadi, M., Lateral shearing interferometers. In *Optical Shop Testing*, 2nd edn, ed. D. Malacara. John Wiley,New York, 1992, p. 136.

7. Sweatt, W. C., Rotatable shear plate interferometer. *Opt. Engng*, **29** (1990) 1157.
8. Malacara, D., Two lenses to collimate red laser light. *Appl. Optics*, **4** (1965) 1652.
9. Saunders, J. B., Measurement of wavefronts without a reference standard

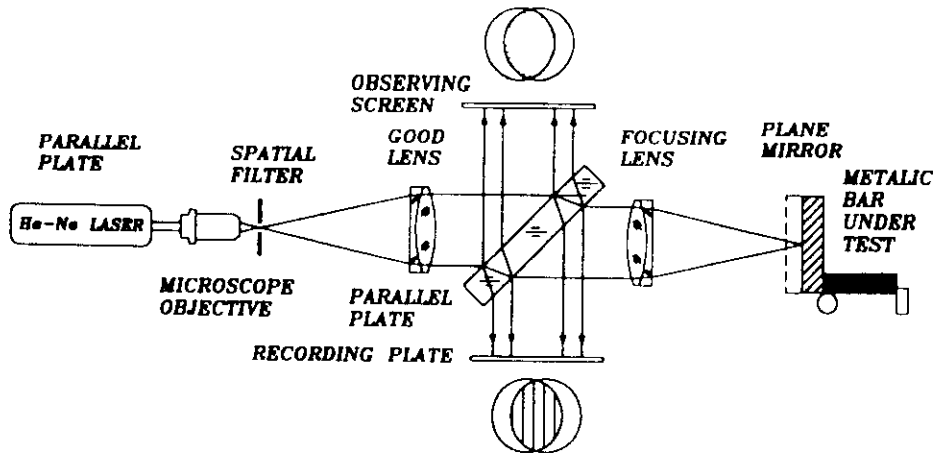

Fig. 37. Schematic diagram of a parallel plate interferometer for measuring the thermal expansion coefficient of a metallic bar.

is shown in Fig. 37. A metallic bar under test is placed in the path of the light transmitted through a parallel plate of glass. One end of the bar is fixed while the other end is free to move along its length. A plane mirror is fixed on the movable end of the bar such that its surface is perpendicular to its length. The collimated laser beam is focused on the plane mirror. The focusing is checked by setting a fringe of uniform brightness. The bar is expanded by heating to a higher temperature. Due to expansion of the bar, the defocusing occurs in the interferometer and straight fringes perpendicular to the direction of shear appear in the shearing interferogram. The fringe spacing is a measure of the defocusing, i.e. the displacement of the mirror due to the expansion of the metallic bar. The linear expansion $\mathrm{d}L$ of the metal is given by

$$\mathrm{d}L = \frac{1}{2}\frac{\lambda}{S}\frac{M}{D}f^2 \tag{45}$$

where λ is the wavelength of the light, M is the number of fringes over distance D in the shearing interferogram, f is the focal length of the focusing lens and S is the shear given by eqn (8).

The linear thermal expansion coefficient α is then calculated by

$$\alpha = \frac{1}{2}\frac{\lambda}{S}\frac{M}{D}\frac{f^2}{L\,\mathrm{d}T} \tag{46}$$

where L is the length of the bar and $\mathrm{d}T$ is the change in the temperature of the bar.

The maximum possible error reported in the measurement of the

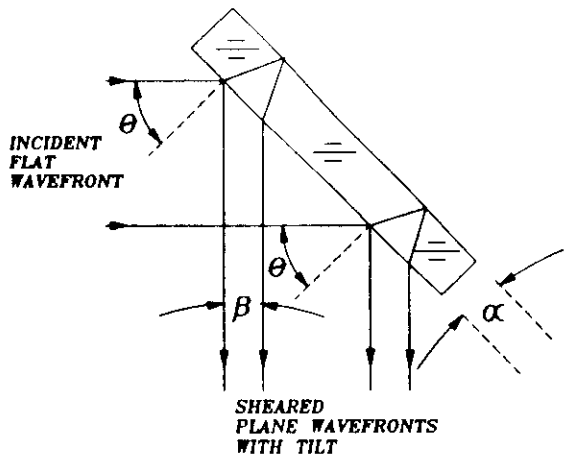

Fig. 36. Schematic arrangement of the interferometer for measuring the wedge angle of a glass plate.

the plate is α, then the angle β between the emergent wavefronts from the front and back surface of the plate is given by

$$\beta = \frac{2\sqrt{N^2 - \sin^2\theta}}{\cos\theta}\alpha = \frac{\lambda}{d} \tag{43}$$

where d is the fringe spacing.

The measurement is done by counting the number of fringes in the common area of the wavefronts. If there are K fringes in the distance $D - S$ for an aperture D and a shear S, then the wedge angle α is calculated by

$$\alpha = \frac{K\lambda\cos\theta}{2(D - S)\sqrt{N^2 - \sin\theta}} \tag{44}$$

Further studies using this method of measuring angles have been reported by Tentori and Celaya.[35]

7 MEASUREMENT OF LINEAR THERMAL EXPANSION COEFFICIENTS

An application of the parallel plate interferometer for measuring the linear thermal expansion coefficient of long metallic bars has been suggested by Srivastava, Tomar and Kasana.[36] The experimental setup

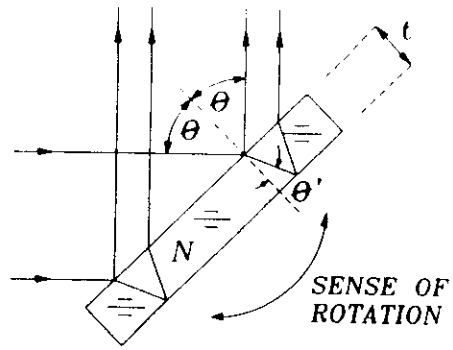

Fig. 35. Schematic arrangement of a parallel plate interferometer for use in measuring angles.

where m is any integer and λ is the wavelength of light. The total angle that the glass plate rotates is given by $\theta_2 - \theta_1$. The integer m is determined by counting the fringes. The angle of rotations is then computed by eqn (3). If the measurement starts at normal incidence, i.e. $\theta_1 = 0$, eqn (40) reduces to

$$\frac{m}{T} = \frac{2}{\lambda}[N - \sqrt{N^2 - \sin^2\theta_2}] \tag{41}$$

This method for measuring angles has two possible applications:

(i) The accurate measurement of angles of prism and wedges. In this case, the measuring plate and the prism are rotated about a common axis. An auto collimator in front of the prism faces may be used to determine the starting and ending points in the fringe counting.

(ii) The measurement of angular velocities of slowly rotating axis is another application of this method. The angular velocity ω in radians per second can be determined by measuring the frequency f of the signal in fringes per second, using the formula

$$f = \frac{dm}{dT} = \left(\frac{4T}{\lambda}\right)\frac{\sin\theta_2\cos\theta_2}{\sqrt{N_2 - \sin^2\theta_2}}\omega \tag{42}$$

This method is capable of measuring any angle from 0° to 360° with a precision of about one second of arc.

Figure 36 shows an arrangement for measuring the wedge angle of glass plate. The collimated beam of laser light is incident on a wedged plate under test. If the angle of incidence is θ, and the wedge angle of

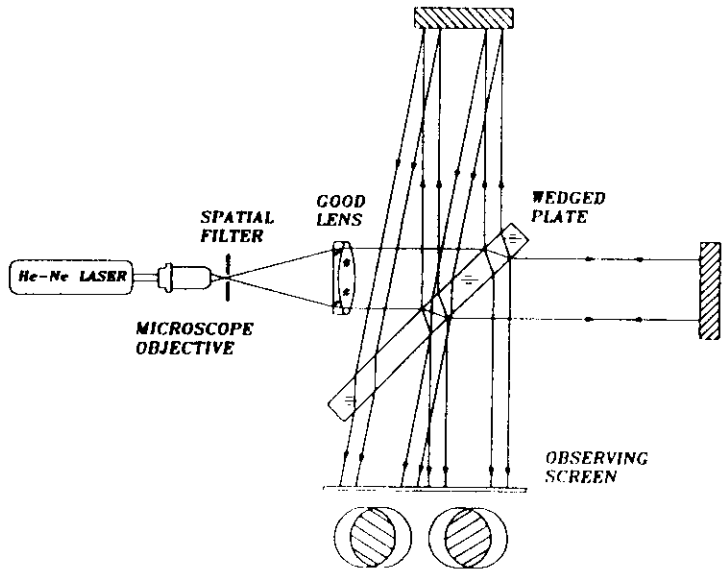

Fig. 34. Schematic arrangement of a Murty interferometer with two interferograms to increase the sensitivity of collimation.

from collimation, the straight fringes move from left to right or from right to left.

6 MEASUREMENT OF ANGLES

A method for measuring small angles or rotations with high accuracy was described by Malacara and Harris[34] using a Murty interferometer. The method is based on the variation of optical path difference OPD between the reflections from the two surfaces of a parallel plate of glass when this plate is rotated. To change the OPD, the plate is rotated about an axis parallel to the plate as shown by a curved arrow in Fig. 35. The difference in the OPD for two different angles of incidence θ_1 and θ_2 on the plate is given by

$$\mathrm{OPD}_1 - \mathrm{OPD}_2 = 2T\,|\sqrt{N^2 - \sin^2\theta_1} - \sqrt{N^2 - \sin^2\theta_2}| \qquad (39)$$

where T is the thickness of the plate and N is the index of refraction.

The condition for destructive interference to occur in this situation is given by

$$\frac{m}{T} = \frac{2}{\lambda}[\sqrt{N^2 - \sin^2\theta_1} - \sqrt{N^2 - \sin^2\theta_2}] \qquad (40)$$

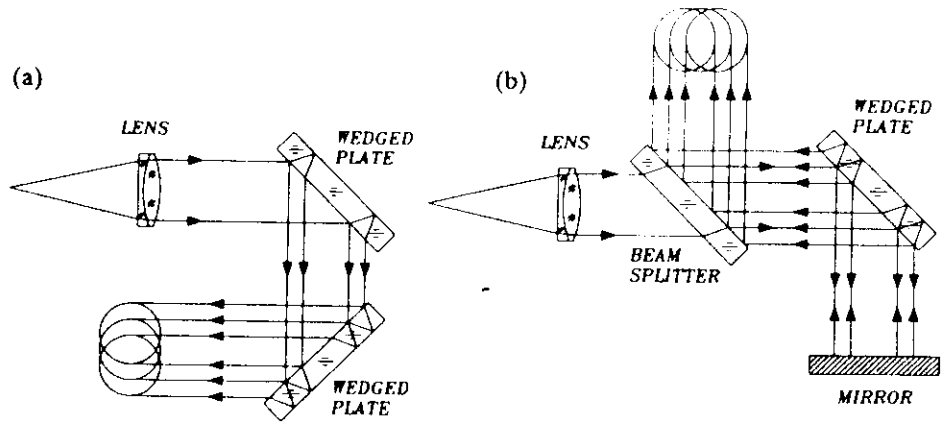

Fig. 32. A series double wedge plate shearing interferometer for collimation test. (a) With two plates, (b) with one plate.

cube corner reflectors, has been devised by Langenbeck.[32] A third method to improve the sensitivity of this test has been described by Gouhua Mingshan and Jingbin.[33] They use an optical arrangement as in Fig. 34. The two fringe patterns will show straight and parallel fringes with an inclination due to the presence of the wedge in the glass plate. When the light beam is not well collimated, the fringes in both patterns rotate due to the wedge in the glass plate. However, the rotation in the two interferograms will be in opposite directions because the transmitted beam reaches the wedge plate in opposite directions.

There is a commercial collimation testing device made by Blue Sky Research, in San José, CA, based on a Murty interferometer using a true parallel plate (without wedge). This instrument shifts the phase between the two wavefronts by slowly rotating the glass plate. At the exact collimation position, the interferogram has no fringes, but the field switches continuously between dark and clear, giving the field a very characteristic blinking appearance. When the position is away

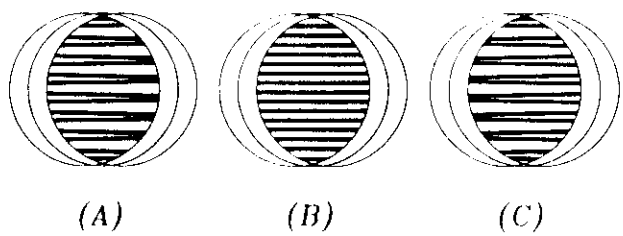

Fig. 33. Schematic drawing of the fringe patterns observed in a series double wedge plate shearing interferometer for collimation test. (A) Inside of focus, (B) collimated, (C) out of focus.

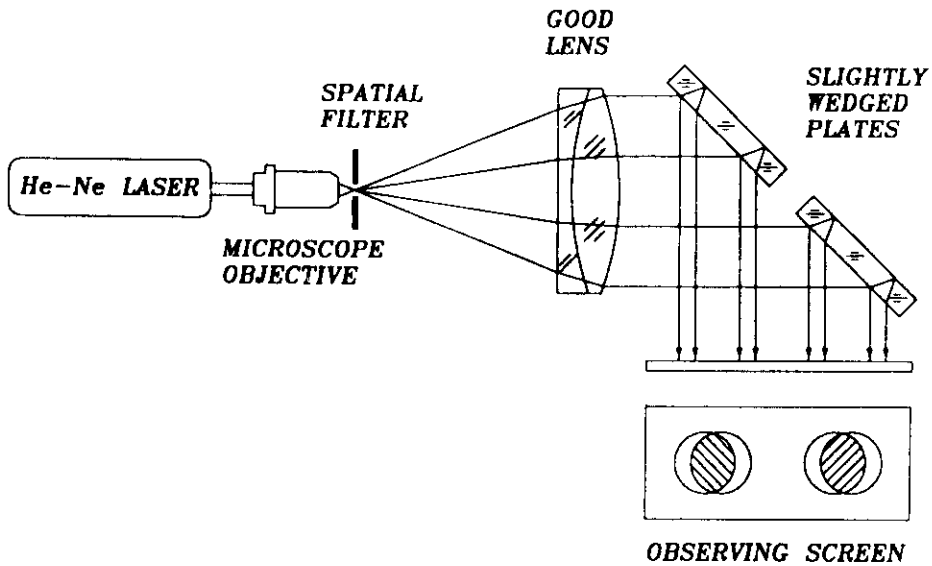

Fig. 31. Double wedge plate shearing interferometer for collimation test.

be horizontal but will be inclined. By moving the lens longitudinally it is evident when one is going through the focus by observing the horizontal fringes. The sequence of the fringe pattern in passing through the focus is like that shown in Fig. 6. A complete study of the Murty interferometer using a rotatable plate with a wedge for collimation testing has been described by Xu and Rosenbruch.[27]

A method of duplicating the sensitivity of this test for collimation has been described by Sirohi and Kothiyal[28] and by Kothiyal, Sirohi and Rosenbruch.[29] Their method, as shown in Fig. 31, uses two plates with the same wedge. The two wedges are parallel to each other, horizontal and on opposite sides. The two interferograms produce straight fringes with opposite slope. The beam is collimated when the two sets of fringes are horizontal.

Sriram, Kothiyal and Sirohi[30] and Sriram, Senthilkumaran, Kothiyal and Sirohi[31] have devised a four-wave interferometer system with two slightly wedged plates, in series, as shown in Fig. 31. Two of the wavefronts coincide in space, without any relative lateral shear. The two wedges are parallel to each other, and both introduce a tilt orthogonal to the shear. The wedges may be on the same or opposite sides. By using a reflecting arrangement as in Fig. 31(b), only a wedged plate is necessary. The result is a set of horizontal fringes if the beam is collimated. Otherwise, the fringes appear as in Fig. 32.

Another similar way to improve the collimation sensitivity, using

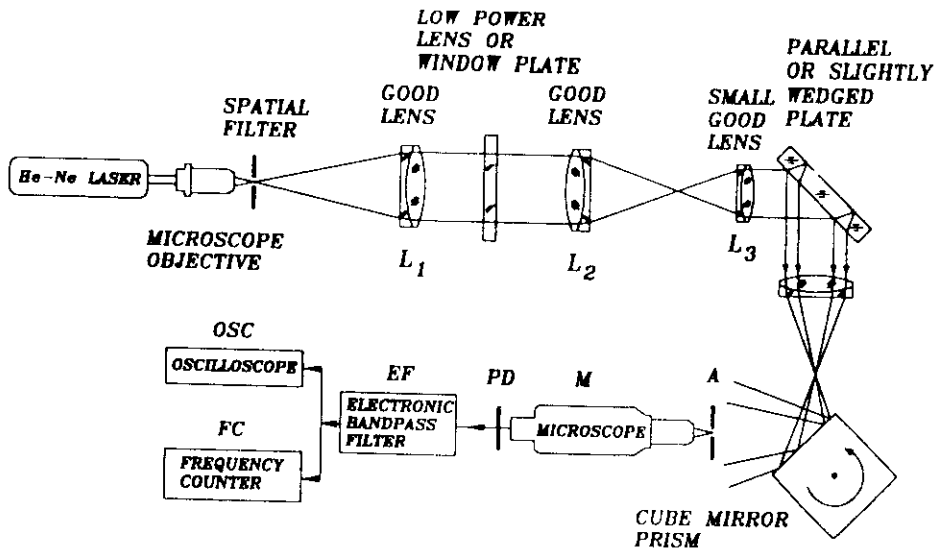

Fig. 30. Schematic diagram of a parallel plate interferometer for measuring the optical distortion of window plate or transparency. The optical arrangement with a digital electronic readout was devised by Taboada (1977).

plate can be tested by bringing different areas into the test region. The reported precision of the measurement in the optical distortion[26] is ±0·005 diopter in this setup.

5 CHECKING THE COLLIMATION OF A LENS

One of the most useful applications of the parallel plate interferometer is for checking (Murty 1992) the collimation of a lens. In Fig. 1 if the pinhole is not located at the focus of the lens, the resulting beam is slightly divergent or convergent. Hence the shearing interferometer pattern is as shown in Fig. 4(a) and (c). Only when the pinhole coincides with the focus of the collimating lens will the common area of the two sheared apertures be free of any fringes as seen in Fig. 4(b). However, a better judgment can be made of the exact collimation if a wedged plate is used for the purpose of indicating it. In this case the plate is first used normal to the beam emerging from the collimating lens. The reflected beam shows the Fizeau fringes indicating the direction of the wedge. Since in this position the shear is zero, slight decollimation does not matter. The wedged plate is rotated in its own plane until the Fizeau fringes are horizontal. Then, the plate is at about 45°. If the pinhole is slightly outside the focus, the shear fringes will not

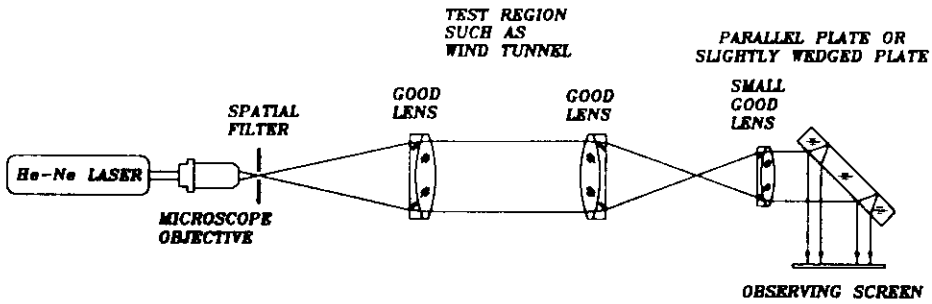

Fig. 29. Schematic arrangement of the parallel plate interferometer for large-aperture wind-tunnel applications.

collimated beam is incident on a combination of lenses L_2 and L_3 separated by the sum of their focal lengths. Therefore, the light emerging out of the lens L_3 is well collimated. The parallel plate then produces two sheared wavefronts showing a fringe of uniform brightness or fringes of nearly zero frequency. However, a slight longitudinal displacement of the lens L_3 introduces a slight positive power in the combination of lenses L_2 and L_3 system. The net power $1/L$ of the lens system is given by

$$\frac{1}{L} = \frac{\lambda}{SX} \tag{38}$$

where S is the shear and X is fringe spacing measured at a convenient place.

Net power in the system can also be introduced by placing a low-power ophthalmic lens in the test region between lenses L_1 and L_2. In such a case, a fringe system of frequency $1/X$ is obtained in the shearing interferogram. The fringe frequency can either be measured by counting the number of fringes per unit length in the interferogram or by sweeping[26] the fringe pattern with a rotating mirror cube across a 100 μm resolution detector consisting of a pinhole aperture A, microscope M and photodiode PD. The periodic fringe signal is low-frequency filtered by an electronic band pass filter EF, monitored with an oscilloscope OSC, and frequency measured with a counter FC.

The calibration is obtained by placing low-power lenses in the test region between L_1 and L_2. A linear plot is obtained of power versus fringe frequency. For measuring the optical distortion, a window plate or a transparency is placed in the test region and the fringe frequency is measured as indicated above. The optical distortion in units of power (diopters) is then determined by the calibration curve. A good window having no distortion shows a power of zero diopters. A large window

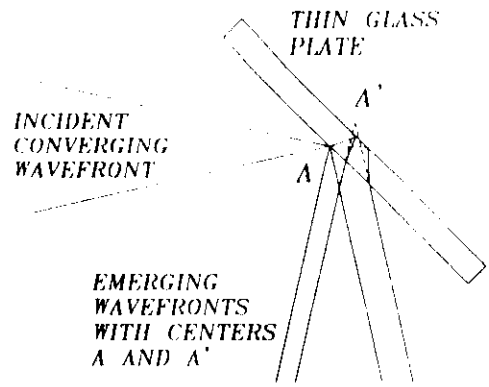

Fig. 27. Ray diagram indicating that pure lateral shear cannot be obtained when the thin glass plate is located at the focus.

the form of an air wedge. Even then only a very limited amount of lateral shear is obtained, and it is better to use a system designed for large aperture wind-tunnel applications or homogeneity measurements, as shown in Fig. 29.

4.6 Measurement of optical distortion in aircraft transparencies and window glasses

An application of the parallel plate interferometer for measuring the optical distortion of large aircraft window plates has been suggested by Taboada.[26] An experimental setup is shown in Fig. 30. A laser beam is expanded up to 2 cm in diameter and collimated by a lens L_1. The

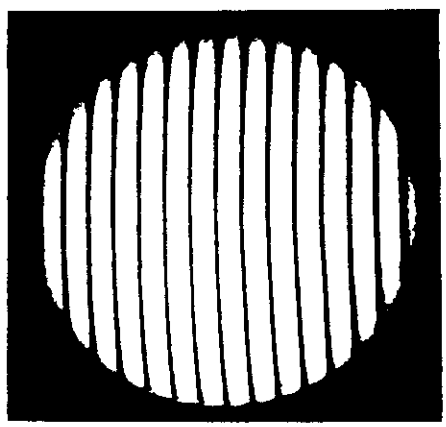

Fig. 28. Typical appearance of the lateral shear fringes in the interferometer shown in Fig. 26.

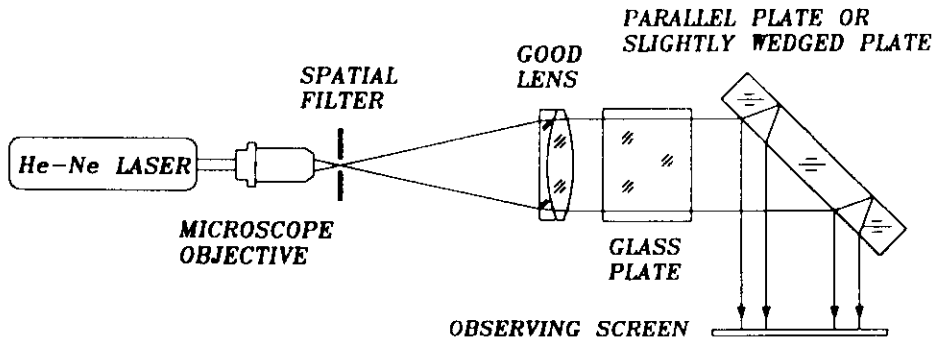

Fig. 25. Schematic arrangement of a parallel plate interferometer for testing the homogeneity of a glass sample.

the shear plate can be used for flow studies, diffusion studies, and other research.

Another modification of the interferometer suitable for the study of aerodynamic research and wind tunnel studies was suggested by Tanner.[24,25] A schematic diagram of this Murty–Tanner arrangement is shown in Fig. 26. A very small, thin parallel plate is used at the focus of the system. The laser light is collimated by the first lens, and after a certain distance, the collimated light beam is focused by the second lens. At a position very close to the focus, a thin glass plate is set at about a 45° angle of incidence. As can be easily seen from Fig. 27 it is not possible to obtain pure lateral shear because of the longitudinal separation between the two images, seen as reflections from the two surfaces of the plate. The result is that, even for a well-corrected optical system, the lateral shear fringes are slightly curved, as shown in Fig. 28. Ideally this system requires an extremely thin plate of glass with a wedge between the surfaces. Alternatively, the system may be made in

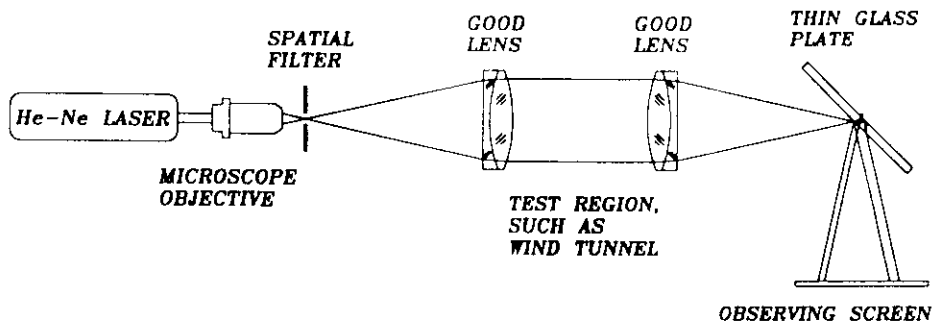

Fig. 26. Schematic diagram of a Murty–Tanner interferometer for wind tunnel studies. A thin parallel plate is used at the point of convergence.

extraordinary ray. The refractive index N_1' for the extraordinary ray is calculated by

$$N_1' = \frac{T}{T - D_1'} \tag{35}$$

Using the above procedure, the refractive indices (N_2, N_2') and (N_3, N_3') are measured along the remaining two directions which are normal to the surfaces of the slab. The birefringence $(N_e - N_o)$ is then calculated using the following relationship:

$$(N_e - N_o) = \left(\frac{1}{2}\right)[(N_1' - N_1) + (N_2' - N_2) + (N_3' - N_3)] \tag{36}$$

where N_e = refractive index for extraordinary ray, N_o = refractive index for ordinary ray N_1', N_2', and N_3' are the refractive indices for the extraordinary ray along the three directions that are normal to the surfaces of the rectangular slab. N_1, N_2, and N_3 are the refractive indices for the ordinary ray (i.e. $N_1 = N_2 = N_3 = N_o$).

The uncertainty in the refractive measurement, dN, is given by

$$dN = \left(\frac{N^2}{T}\right) dD \tag{37}$$

where dD is the uncertainty in the measurement of the displacement D, and N is the refractive index. Assuming $dD = \pm 0{\cdot}003$ mm, $t = 4$ mm, $N = 1{\cdot}5$, then $dN = \pm 0{\cdot}002$. The accuracy of the measurement can be increased by up to $\pm 0{\cdot}0002$ for a sample of thickness of 40 mm.

It may be pointed out here that fringes of high contrast are obtained only when the direction of vibration of the polarized light is parallel to the directions of either the ordinary ray or the extraordinary ray.

4.5 Determination of homogeneity of solid glass samples and aerodynamic studies

A schematic arrangement for the determination of homogeneity[2] of a glass sample is shown in Fig. 25. The sample may be prepared in the form of a parallel plate of glass and sandwiched between two very good plane plates, using a suitable oil for contact. This sandwich is placed between the collimating lens and the shearing plate. Since a good plane wavefront passes through the sample, any inhomogeneity distorts this wavefront, which when laterally sheared reveals the inhomogeneity. This method can very easily reveal variations in the refractive index inside the material. The same region between the collimating lens and

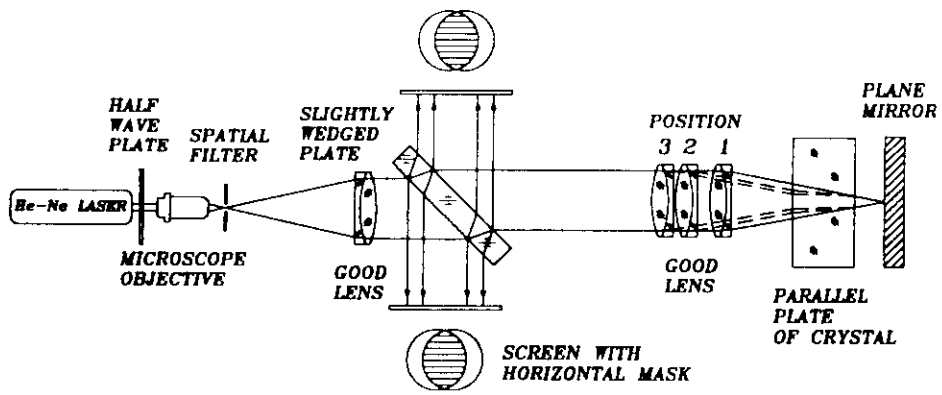

Fig. 24. Schematic diagram of a wedged plate interferometer for measuring the birefringence of optical materials.

lens. The expanded laser beam is focused on a plane mirror by a well-corrected focusing lens mounted on a precision distance measuring device. The apex of the wedged plate is made horizontal by the procedure described in Section 2. Horizontal straight fringes are formed in the shearing interferogram for the precisely focused beam on the plane mirror. Position 1 of the focusing lens is noted. To measure the birefringence of the crystal, a parallel plate of the crystal is placed between the focusing lens and the plane mirror. Longitudinal displacement of the focus for one plane of polarization (say for the ordinary ray) makes the fringes inclined. The focusing lens is then moved away from the plane mirror in order to focus the laser beam on the plane mirror and horizontal straight fringes are again seen on the screen. Position 2 of the focusing lens is noted on the scale of the carriage. The difference between the two positions 1 and 2 gives the displacement D_1 for the ordinary ray. The thickness T of the slab is measured by a micrometer. The refractive index N_1 for the ordinary ray is given by

$$N_1 = \frac{T}{T - D_1} \tag{34}$$

To measure the refractive index for the orthogonal polarization, i.e. for the extraordinary ray, the plane of polarization of the laser light is rotated through 90° by rotating the half-wave plate. Inclined fringes are again obtained on the screen. The fringes are made horizontal by displacing the focusing lens to position 3 such that the light is focused precisely on the plane mirror. The difference between position 3 and the position 1 is a measure of the longitudinal displacement D_1' for the

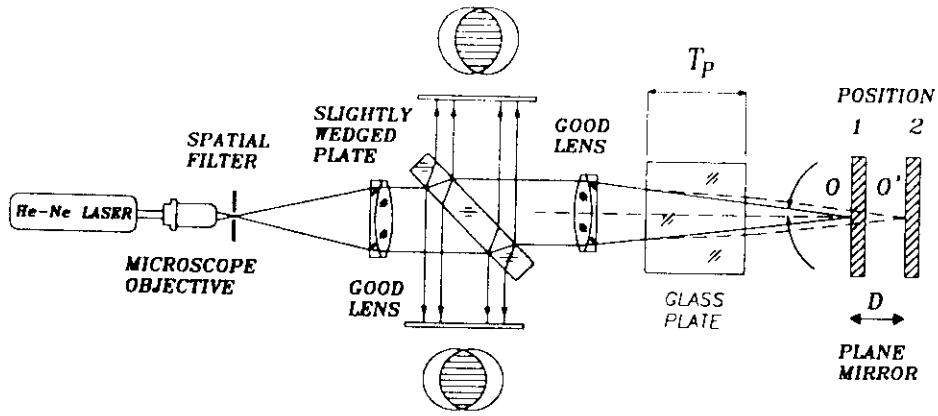

Fig. 23. Schematic diagram of a parallel plate interferometer for use in measuring the refractive index of a glass.

accuracy of ±0·0002 in the measurement of the refractive index of liquids using this setup.

Figure 23 shows a corresponding arrangement for measuring the refractive index of a glass. The glass sample must be fabricated in the form of a parallel plate. The refractive index of the glass is calculated from the following relationship:

$$N_g = \frac{T_p}{T_p - D} \tag{33}$$

where the thickness T_p of the glass plate under test is measured by an accurate micrometer and the displacement is determined by the interferometer. The accuracy achieved in the measurement of the refractive index of glass is ±0·0002.

4.4 Measurement of the birefringence of optical materials

Figure 24 shows a schematic diagram of the wedged plate interferometer for measuring birefringence[23] of optical materials. The material must be in the form of a parallel plate. When the optical axis of the crystal is unknown, a rectangular plate of the crystal is cut and all six surfaces of the slab are ground and polished in such a way that the opposite surfaces are parallel to each other. A He–Ne laser emitting a plane polarized light is used in this setup. A half-wave plate is placed between the He–Ne laser and the microscope objective to rotate the plane of polarization of the laser light. Laser light is expanded by a beam expander consisting of a microscope objective and a collimating

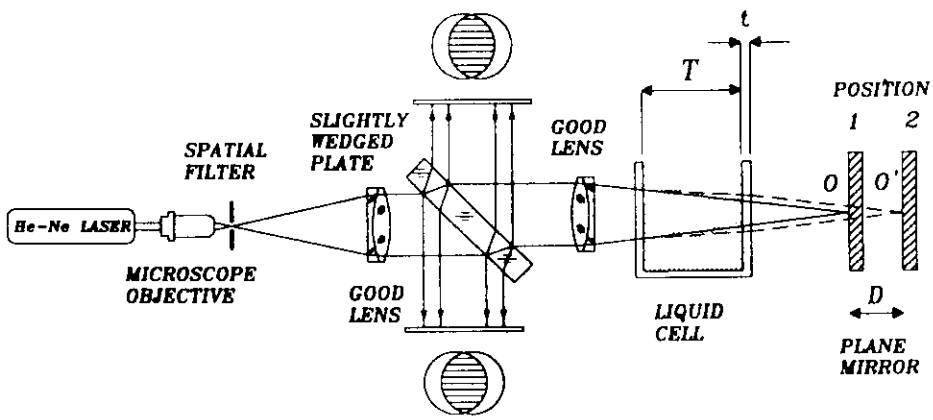

Fig. 22. Schematic diagram of a parallel plate interferometer for use in measuring the refractive index of a liquid.

remains collimated after passing through the cell and lens. This is indicated by observing the horizontal straight fringes in the field. The position of the plane mirror is noted. To measure the refractive index of a liquid, the liquid sample is filled into the cell. The liquid cell now functions like a parallel plate of thickness T and refractive index N_L in the converging beam of light. Consequently, the focus of the lens–liquid cell combination is displaced along the optical axis by an amount given by

$$D = \frac{T(N_L - 1)}{N_L} \tag{31}$$

The longitudinal displacement of the focus is indicated by the inclination of the fringes from the horizontal direction. The plane mirror is then moved back to the new focus O′ in such a way that the fringes again become parallel to the horizontal direction. The position O′ of the mirror is noted. The difference between positions O and O′ gives the measurement of the displacement D caused by the liquid sample. If the cell length T is known, the refractive index of the liquid is calculated by eqn (31), which can be rewritten in the following form

$$N_L = \frac{T}{(T - D)} \tag{32}$$

Since the displacement is measured by taking the difference between two positions of the mirror, the accuracy in the measurement of the displacement D is of the order of a micron. It is possible to achieve an

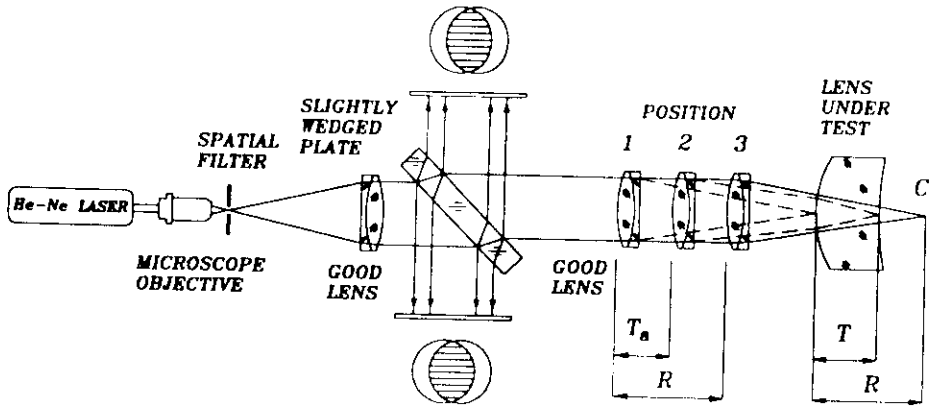

Fig. 21. Schematic diagram of a wedged plate interferometer for measuring the refractive index of a lens. In this setup, the convex surface faces toward the wedged plate.

The method described here is useful for measuring refractive indices of simple negative-, positive- or zero-power lenses. In the case of a plano-concave or plano-convex lenses, the lens is mounted such that light enters the plane surface. The apparent thickness T_a and the actual thickness are measured and the refractive index is given by

$$N = \frac{T}{T_a} \tag{30}$$

An error analysis was done and the measuring accuracy reported[20] is in the range ±0·04 to ±0·001. The measuring accuracy is a function of the shape, radius of curvature, and thickness of the lens. If the lens is of the meniscus type, i.e. the front surface is convex and the rear surface is concave, then it is preferable to measure the radius of curvature of the concave surface using the setup of Fig. 20 to obtain a more accurate value.

4.3 Measurement of the refractive index of a liquid or glass

Another application of the Murty interferometer involves the measurement of the refractive index of a liquid with the instrument shown in Fig. 22 designed by Shukla.[22] A well-collimated laser beam is incident on a wedged plate whose apex lies in the horizontal plane. A focusing lens is placed in the path of the transmitted beam. An empty cell is placed in the converging beam of the light obtained by the focusing lens. A plane mirror is then placed at the focus of the lens and empty cell combination. In this position, the light is reflected back and

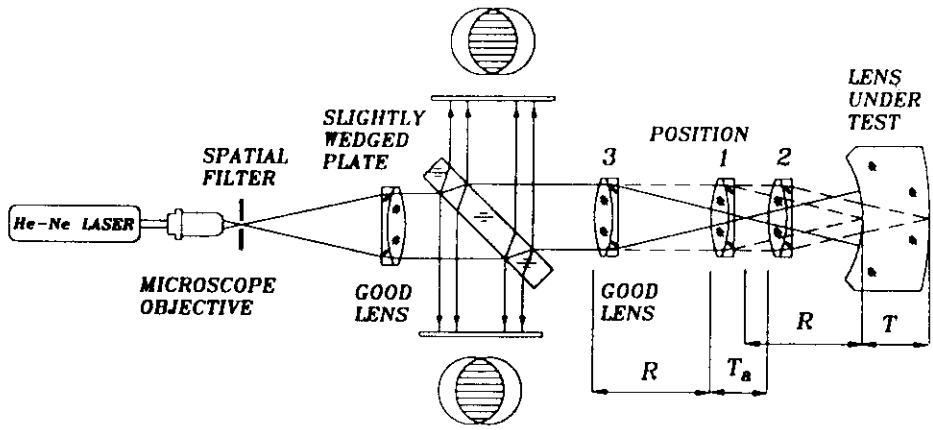

Fig. 20. Schematic diagram of a wedged plate interferometer for measuring the refractive index of a simple negative, positive or zero power lens. In this setup, the concave surface faces toward the wedged plate.

focusing lens is noted on the scale of the carriage. The focusing lens is then moved toward the lens under test in order to focus the light beam on the rear surface of the lens and Position 2 of the focusing lens is noted. The difference between positions 1 and 2 gives the apparent thickness T_a of the test lens. Finally, the focusing lens is moved away from the test lens in order to focus the light beam on the center of curvature of the front surface of the lens. Straight fringes are again obtained when the focus coincides with the center of curvature of the front surface of the lens. Position 3 of the focusing lens is noted and the distance between positions 1 and 3 gives the radius of curvature R of the front surface of the test lens. The central thickness T of the test lens is measured with a micrometer. The refractive index N of the lens is calculated by

$$N = \frac{T(R + T_a)}{T_a(R + T)} \tag{28}$$

Figure 21 shows an optical arrangement for measuring the refractive index of a lens whose convex surface faces towards the wedged plate. The refractive index N of the lens is calculated by

$$N = \frac{T(R - T_a)}{T_a(R - T)} \tag{29}$$

This optical arrangement is similar to that of Fig. 20 except that the focusing lens is moved toward the test lens to measure the radius of curvature of the convex surface.

lens. Hence the focal lengths of the lens in liquids 1 and 2 should be measured separately to determine the refractive index of the lens. Liquids of known refractive indices should be selected and the focal length of the test lens is determined independently with each liquid. The back focal length of the optical system in Fig. 19 is defined as the distance between the focal plane and the back surface of the glass cell and this is determined exactly by means of the parallel plate interferometer. The actual focal length is given by

$$f = S_f' + \frac{T_G}{N_G} + \frac{T_L}{N_L} + S_p', \tag{25}$$

where S_f' = the distance between the back surface of the glass cell and the focal point, T_G = the thickness of the rear side of the cell, S_p' = the axial distance between the principal point and the back vertex of the lens, T_L = the axial thickness of the liquid column between the lens and the rear side of the cell, and N_G and N_L = the refractive indices of the glass cell and the liquid inside the cell, respectively. The factor S_p' is given by

$$S_p' = \frac{T}{N} \tag{26}$$

for a plano-convex lens and

$$S_p' = \frac{T}{2N} \tag{27}$$

for a biconvex lens of equal surface curvatures.

If all the parameters of the cell and liquid are known and the back focal length is determined experimentally, then the refractive index of the lens can be calculated by the use of eqns (24)–(27). The accuracy of the measurement in the refractive index of the lens as reported by Kasana and Rosenbruch[19] is of the order of 1×10^{-4} in this setup.

4.2 Measurement of the refractive index of lenses

An alternative method[21] for measuring the refractive index of a lens is shown schematically in Fig. 20. The apex of the wedged plate is set parallel to the horizontal direction. A focusing lens is mounted on a carriage and placed in the path of collimated beam of laser light. The light is focused on the front surface of the test lens, which is placed on the optical axis of the focusing lens. Consequently, horizontal straight fringes are obtained in the shearing interferogram. Position 1 of the

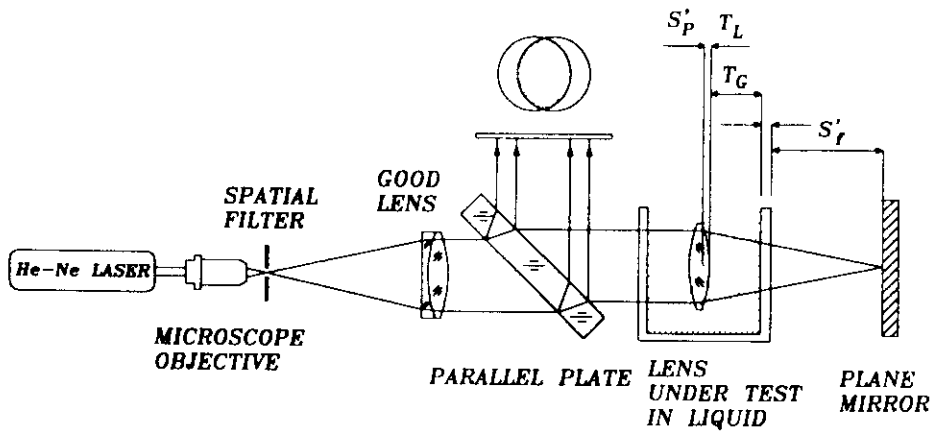

Fig. 19. Schematic diagram of a parallel plate interferometer for measuring the refractive index of a lens.

is repeated. The method described here is applicable only to converging lenses.

4 MEASUREMENT OF REFRACTIVE INDICES AND HOMOGENEITY

4.1 Measurement of the refractive index of lenses with a liquid cell

An innovative nondestructive technique for measuring the refractive index of a simple lens was described by Kasana and Rosenbruch[19] who used a Murty interferometer. The schematic arrangement for this purpose is shown in Fig. 19. The arrangement contains a well-corrected lens which collimates the beam. A glass cell with plane parallel plates as walls is placed in the path of the collimated beam. The test lens is immersed in the liquid inside the glass cell. The wavefront converges to a point incident on a plane mirror which reflects it. This reflected wavefront again passes through a lens which acts as an autocollimator. The plane parallel glass plate is used to test the collimated wavefronts. The refractive index N of the lens is given by the following relationship:

$$N = \frac{N_2 f_2 - N_1 f_1}{(f_2 - f_1)} \tag{24}$$

where f_1 is the focal length of the lens in a liquid of refractive index N_1 and f_2 is the focal length of the lens in a liquid of refractive index N_2. Relationship (24) is valid only for a thin lens or for a plano-convex

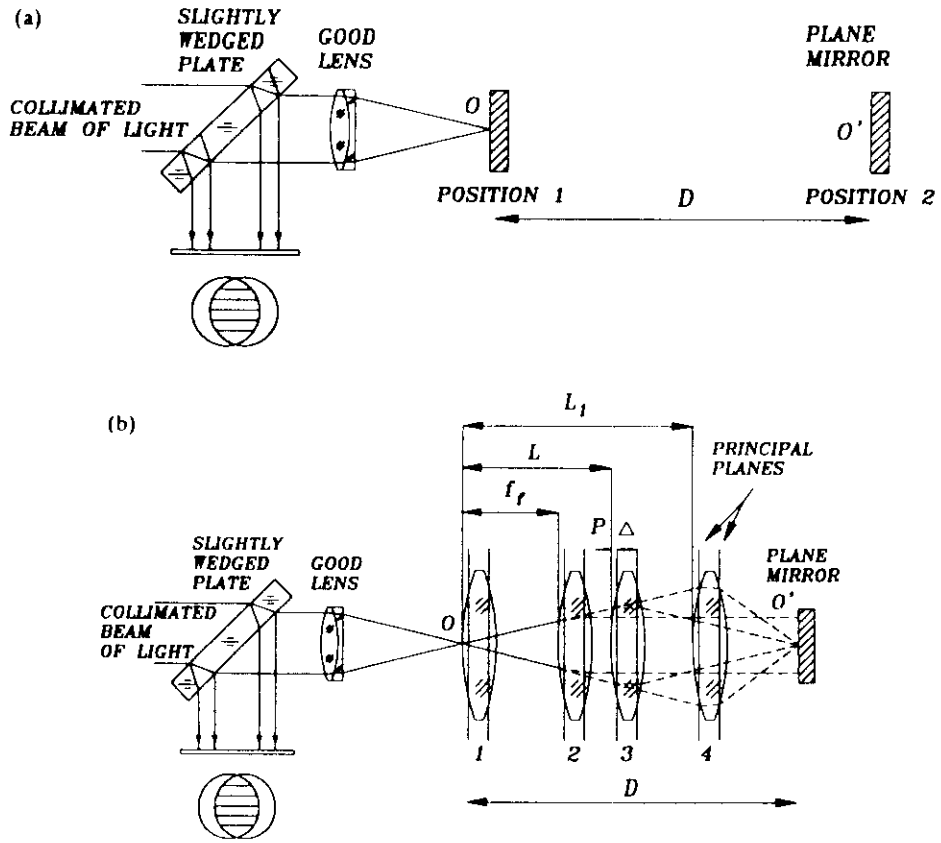

Fig. 18. Schematic diagram showing a parallel plate interferometer in two steps (a) and (b) for location of the cardinal points of a lens system.

The distance between the principal points is given by

$$\Delta = D - (L_1 + L + 2P) \tag{22}$$

The effective focal length of the lens is then calculated from the following equation:

$$\text{efl} = f_f + P = \sqrt{(L - f_f)(L_1 - f_f)} \tag{23}$$

The distance P is considered to be positive when the principal point lies on the right side of the front surface. When the distance P is negative, the front focal length is greater than the effective focal length. By measuring the distances L, L_1 and f_f the position of the cardinal points can be computed from eqns (21)–(23). For measuring the back focal length, the lens is rotated through 180° and the whole procedure

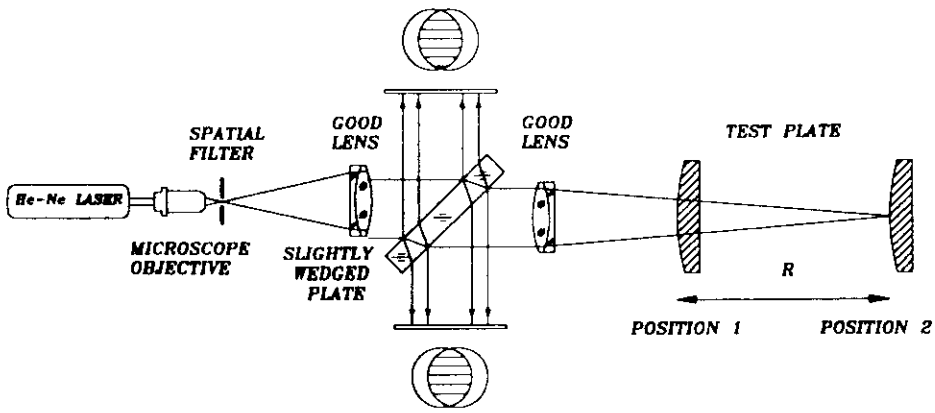

Fig. 17. Schematic diagram of a parallel plate interferometer for measuring the radius of curvature of a convex spherical surface.

The Murty interferometer has also been used for determining the lens parameters.[19,20] Figure 18(a) and (b) shows the schematic arrangements for the determination of effective focal length, efl, and front focal length. The first step is to bring the plane mirror at the focus O by setting the fringes horizontal and noting down the position of the mirror. The mirror is now displaced to a convenient position depending upon the focal length of the lens under test. The position O′ of the mirror is noted. The difference between these two positions is denoted by D. The second step is to place the lens under test at the focus O and the positions are noted (see Fig. 18(b)). The lens is now moved to a position 2 so that the focus of the beam coincides with the focal point of the lens. In this setting the wavefront reflected back is a plane, and consequently one sees a field containing horizontal fringes. The distance between position 1 and position 2 gives the front focal length. The third step is to move the lens to a position 3 such that the image of the point O is focused on the plane mirror at O′. The distance between position 3 and position 1 is denoted by L. The last step is to move the lens to a position 4 such that the points O and O′ are again conjugate points. The distance between position 4 and position 1 is denoted by L_1. The cardinal points can be located by solving the following equation:

$$p^2 + 2f_1P + f_1(L_1 + L) - LL_1 = 0 \tag{20}$$

where P is the distance of the first principal point from the front surface and f_1 the front focal length.

$$P = -f_1 \pm \sqrt{f_1^2 + LL_1 - f_1(L + L_1)} \tag{21}$$

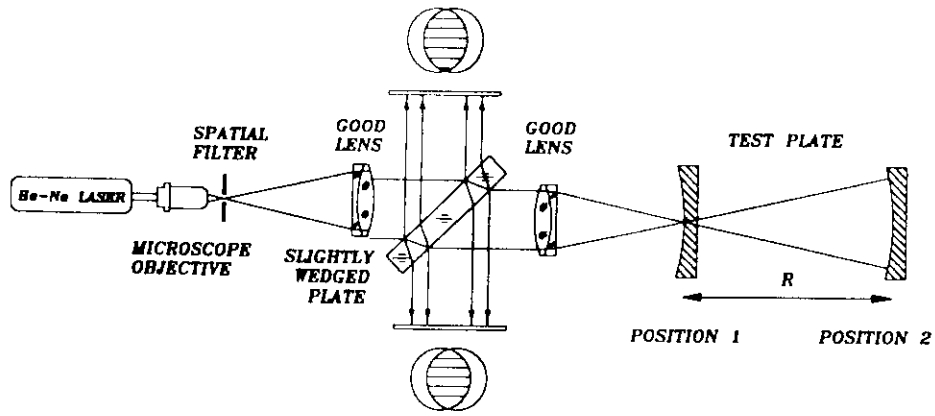

Fig. 16. Schematic diagram of a parallel plate interferometer showing its use in measuring the radius of curvature of a concave spherical surface.

3.3 Measurement of short radius of curvature and location of cardinal points of a lens system

Another application of the interferometer involves the measurement of the radius of curvature[18] of a concave spherical surface as shown in Fig. 16. The system contains two well-corrected lenses, the first of which collimates the beam. The shearing plate is located between the two lenses such that the apex of the wedge is in the horizontal plane. The test plate under test is brought to the focus of the lens. The reflected beam is again collimated by the focusing lens and interference is observed due to the sheared wavefronts. The position of the test plate is noted. The test plate is then moved towards the right in order to focus the laser beam at its center of curvature. When the focus of the beam coincides with the center of curvature of the test plate, horizontal straight fringes are observed. Even a slight error in the setting will incline the fringes, which can be easily detected by placing a horizontal wire against the fringes. The second position of the test plate is noted. The displacement of the test plate between these positions gives the radius of curvature. Since the distance is measured by taking the difference between the two positions, the accuracy of the measurement is high. Figure 17 shows the corresponding arrangement for convex surfaces. In this case the longest radius of curvature of the test plate that can be measured is slightly less than the focal length of the focusing lens. The collimating lenses in the above applications have to be very good, and several designs have been suggested by Malacara (1965), among others.

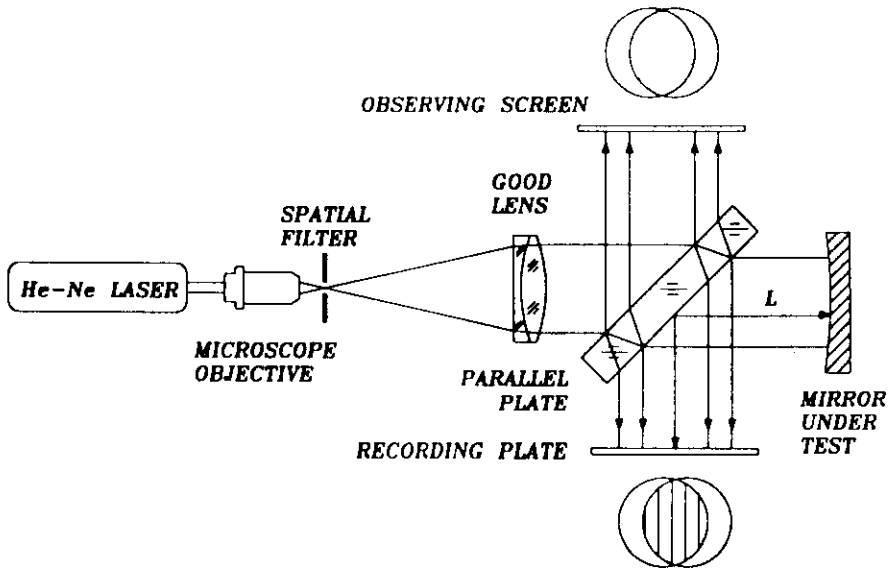

Fig. 14. Schematic diagram of a lateral shearing interferometer for measuring a long radius of curvature for a concave spherical surface. In this arrangement, the shearing plate is a parallel plate of glass.

plate, and the reverse is true for the convex surface. Figure 15 shows the shearing interferogram of a concave mirror of radius 10·275 m which was recorded in the setup of Fig. 14.

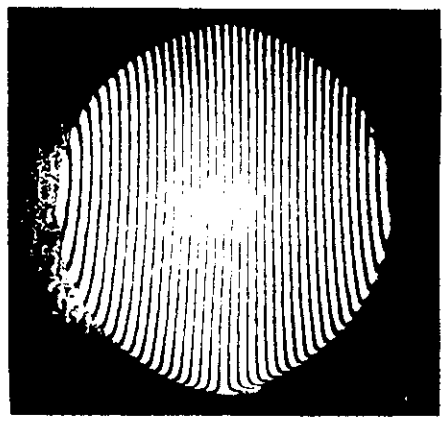

Fig. 15. Photograph of the shearing interferogram of a concave mirror taken with the arrangements of Fig. 14.

convex mirror. L is the distance of the mirror from the recording plane via a parallel plate. Using eqn (8), the lateral shear distance S is calculated by measuring the thickness T and angle of incidence θ. The angle of rotation ϕ is measured from the interferograms and the radius of curvature is then calculated by eqn (17). The accuracy of the measurement is about 0·2% of the radius of curvature. Riley and Gusinow used the following parameters for the glass plate: $N = 1{\cdot}515$, wedge angle = 6·91 seconds of arc, and $T = 1{\cdot}343$ cm.

An alternative optical arrangement for measuring the radius of curvature using a parallel plate of glass[10a,18] is shown schematically in Fig. 14. The collimation is achieved by obtaining uniform illumination over the common region of the sheared wavefronts. In order to achieve a high degree of collimation, it is preferable to use a large aperture lens and large aperture parallel plate. A 100-mm aperture lens and 150-mm aperture parallel plate will be quite adequate for this purpose. In this arrangement, the interference fringes are formed perpendicular to the direction of the shear due to the curved nature of the mirror under test. The radius of curvature of the wavefront at the recording plate is given by

$$R_L = \frac{Sd}{\lambda} \pm \frac{S}{2} \cot \theta \tag{18}$$

where d is the fringe spacing. The positive sign is used for a converging beam and the negative sign for a diverging beam. The radius of curvature of the mirror is given by

$$r = 2\left[\frac{SD}{\lambda n} \pm \frac{T \cos^2 \theta}{\sqrt{N^2 - \sin^2 \theta}} \pm L\right] \tag{19}$$

where L is the distance between the recording plane and the mirror and D is the distance between n fringes in the whole overlapping region along the diameter of the sheared wavefronts. The distance D is measured from the photograph of the shearing interferograms by using an accurate distance-measuring device. The thickness of the plate, T, is measured with a micrometer. For measuring the angle of incidence, the parallel plate is usually mounted on the rotating disc of the spectrometer. The parallel plate is set in autocollimation by making the back-reflected image from the plate coincide with the pinhole. The spectrometer reading is noted. Now the disc is rotated through the required angle. In order to determine the nature of the mirror (i.e. concave or convex), the spacing of the fringes is measured at two different recording planes. For concave surfaces, the fringe spacing decreases as the recording plane is moved away from the shearing

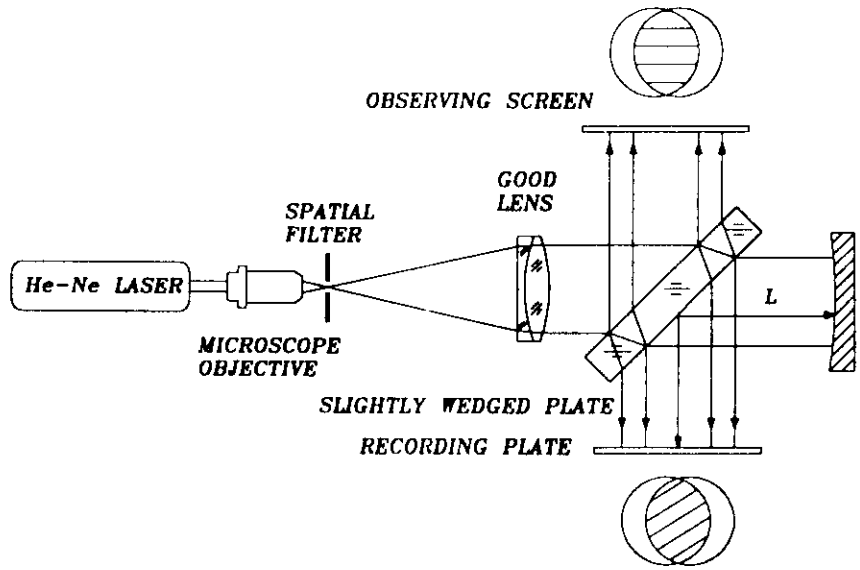

Fig. 12. Schematic arrangement of a lateral shearing interferometer for measuring a long radius of curvature for a concave spherical surface. In this case, the shearing plate is slightly wedge-shaped.

the radius of curvature r of the mirror is calculated from the following relationship, which was derived by Riley and Gusinow (1977)

$$r = 2\left(\frac{Sd}{\lambda \sin \phi} \pm L\right) \tag{17}$$

where the + sign is used for a concave mirror and the − sign for a

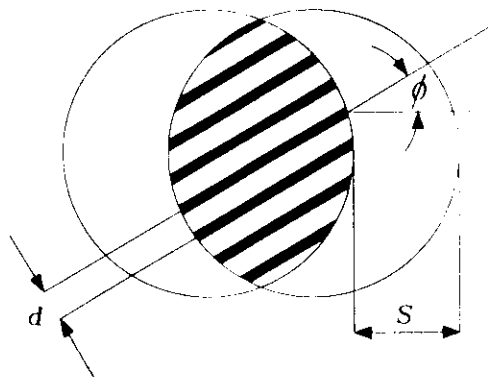

Fig. 13. Schematic representation of interference pattern resulting from the shearing interferometer shown in Fig. 12.

appear in the common area of the two beams. Spacing of these fringes is inversely proportional to the relative local power of the lens. The interferometer can be adjusted so that light leaving the center of the lens is essentially collimated. Then, if the interference fringe spacing X is measured near the edge of the lens, the average power of the lens in the direction of the shear, for the region where the fringe spacing is measured, is different from the power at the center of the lens by an amount equal to

$$P = \frac{\lambda}{XS} \tag{15}$$

If the interferogram is M times as large as the lens, both the shear S and the distance X between the fringes on the interferogram are M times as large as the corresponding distances on the lens under test. Therefore, the power distribution of the lens is given by

$$P = \frac{M^2\lambda}{XS} \tag{16}$$

where M is the magnification of the system and X and S are measured from the interferogram.

The interferometer measures power only in the directions of the shear. The power in each principal axis of a toroidal lens can be measured separately when the lens is oriented so that one of the cylinder axes is perpendicular to the directions of the shear. The power of the second principal axis of a toroidal lens can then be measured by rotating the lens through an angle of 90°.

3.2 Measurement of a long radius of curvature

Figure 12 shows an optical arrangement described by Riley and Gusinow[17] for measuring the radius of curvature of a concave or convex surface. A wedge plate is placed in the path of the beam such that the apex of the wedge is horizontal. The mirror under test is placed on the optical axis of the beam. In this position the reflected beam from the mirror is focused back on the pinhole itself. The shearing interferogram is recorded on the photographic plate. The interference fringes are inclined with respect to the direction of shear due to the curved wavefront obtained from the curved mirror. Figure 13 shows a schematic representation of the interference fringes resulting from a shearing interferogram. If d is the fringe spacing, S the shear, and ϕ the angle of rotation of the fringes with respect to the direction of shear,

of a pair of 35 mm plano-parallel plates of elliptical shape, which are fastened to a steel ribbon running around two pulleys. The pair of plano-parallel plates scan the mirror as they are translated around the aperture in opposite directions by the rotation of the mirror blank. A laser source assembly consisting of a 10 mm aluminized diagonal inside the microscope tube with its diverging objectives is mounted on a lever arm, which can be raised and lowered by a differential micrometer. This focusing arm and the micrometer measure the reflective deviations at each zone being scanned by the pair of plano-parallels. The two reflective interferograms are projected on a viewing screen. The angular deviations can be converted to surface deformations.

3 MEASUREMENT OF LENS PARAMETERS

3.1 Measurement of the power distribution in ophthalmic lenses

The use of the parallel plate interferometer for measuring the power variation of ophthalmic lenses was described by Wyant and Smith.[16] A schematic arrangement of the interferometer is shown in Fig. 11. The lens being tested is placed either in a converging or in a diverging beam of light, so that the light leaving the lens is essentially collimated. If the beam leaving the lens is not perfectly collimated, interference fringes

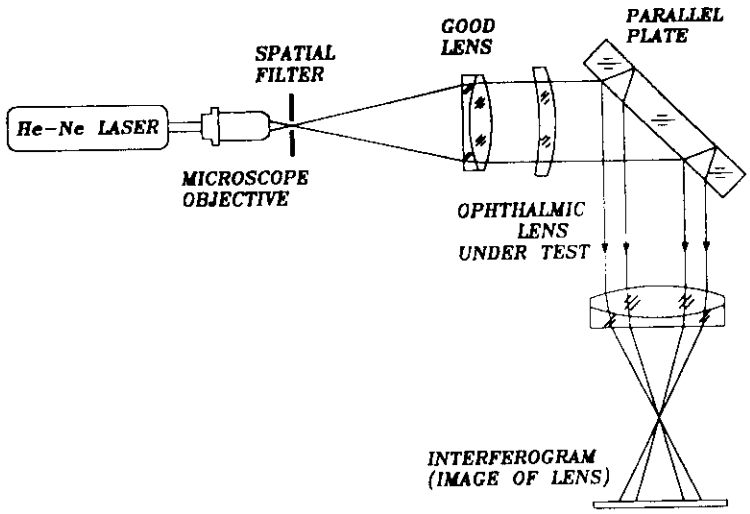

Fig. 11. Schematic diagram of a parallel plate interferometer for measuring the power distribution of ophthalmic lenses.

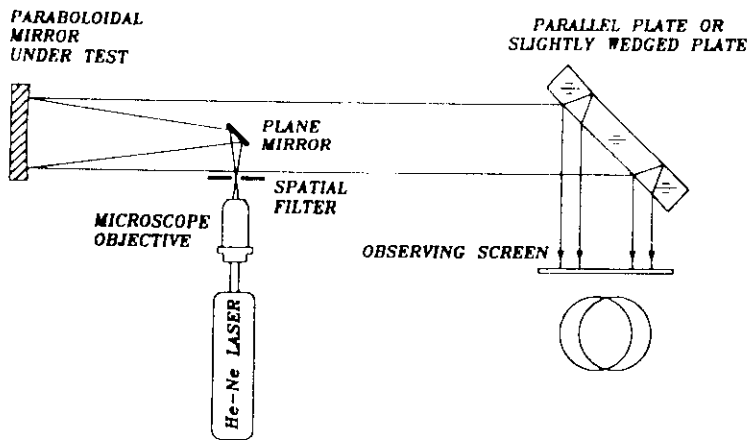

Fig. 9. Schematic arrangement of a parallel plate interferometer for testing a paraboloidal mirror of moderate aperture.

because this particular arrangement eliminates the need for a large-size parallel plate. Figure 10 shows schematically the arrangements devised by De Vany and De Vany called a scanning Murty interferometer. The large concave mirror on the polishing machine is being tested. The assembled scanning unit is mounted in the parallel beam and consists

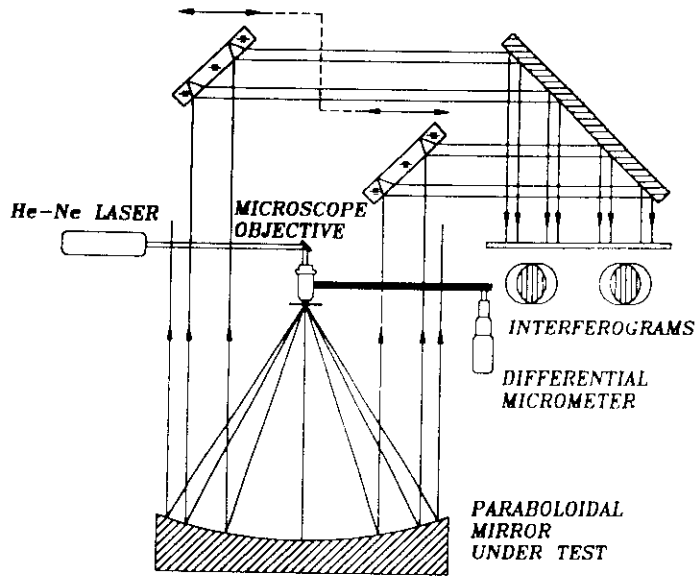

Fig. 10. Schematic arrangement of a parallel plate interferometer for testing a paraboloidal mirror of large aperture. The scanning arrangement was devised by De Vany

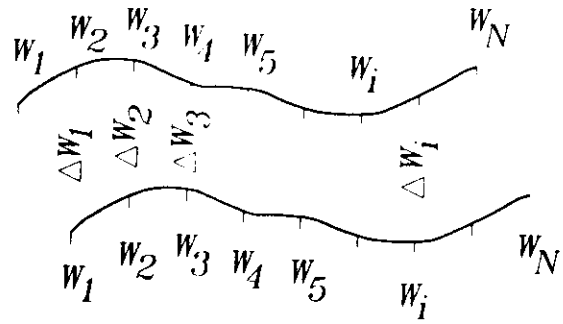

Fig. 7. Computation of the wavefront deformation at several points along a line in the direction of the shear.

reduced considerably. A schematic scheme of the interferometer for the testing of a large concave mirror was devised by Malacara,[32a] as shown in Fig. 8. If the mirror is not spherical, a suitable null correcting system may be inserted into the setup. The shearing interference pattern is scanned photo-electrically or a fringe photograph is taken from which the surface figure of the mirror is analyzed.

2.3 Testing of paraboloids

The schematic arrangement for the testing of a paraboloid is shown in Fig. 9. The laser beam is focused with a microscope objective at the focus of the paraboloidal surface and the beam is well collimated. The rest of the procedure for determining the wave aberration is the same as that for the lens. This scheme is useful only for the testing of a paraboloidal surface of small aperture, say up to 15 cm. Another scheme was adopted by De Vany[3] for a large-size paraboloidal surface,

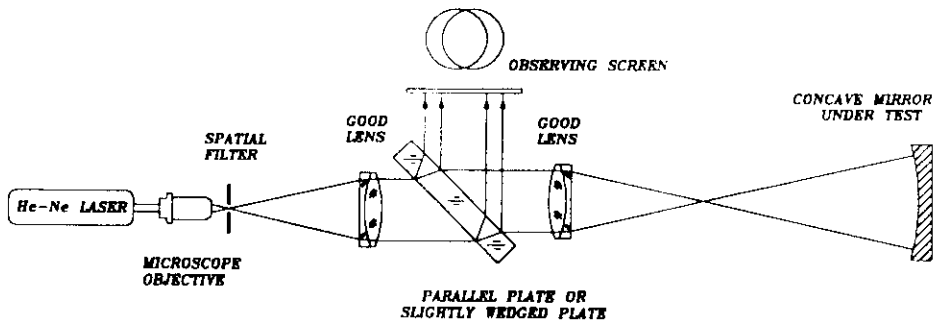

Fig. 8. Schematic diagram of a parallel plate interferometer for use in testing large concave mirrors.

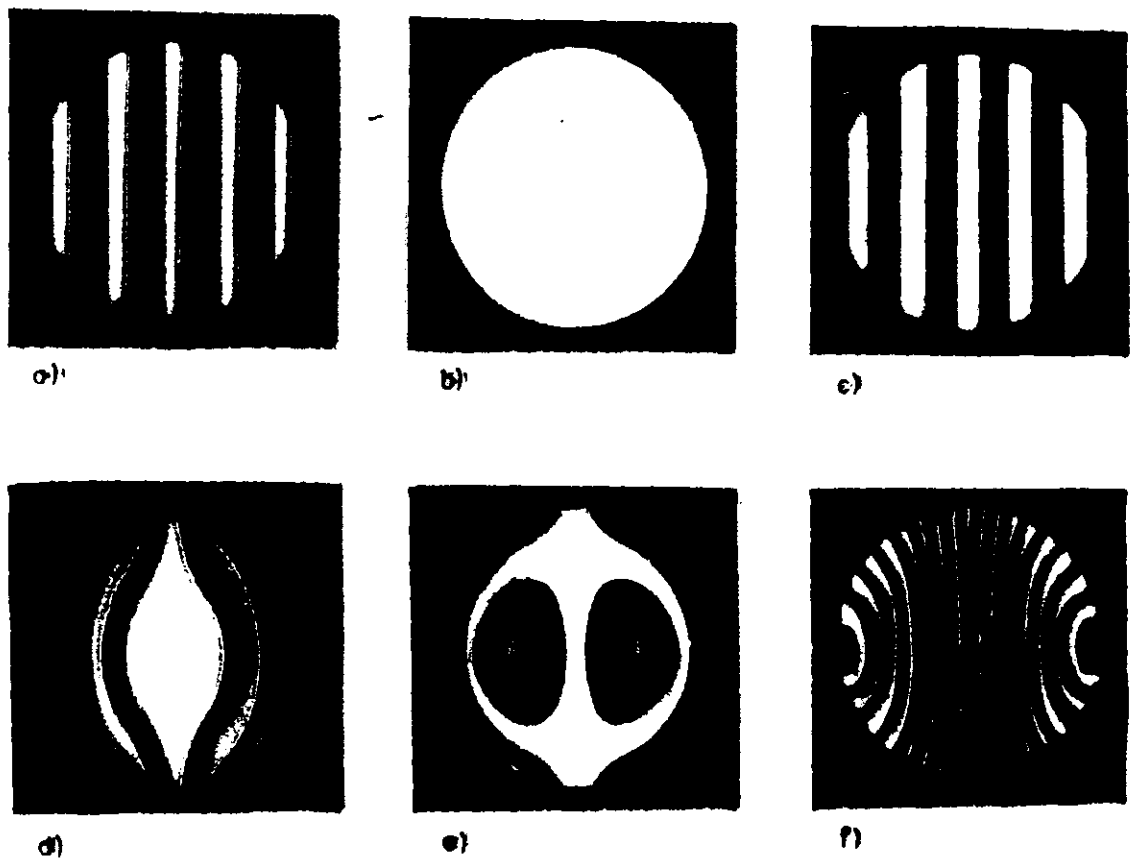

Figure 4.- Typical Ronchi patterns for an spherical and a parabolic mirror for different positions of the Ronchi ruling..

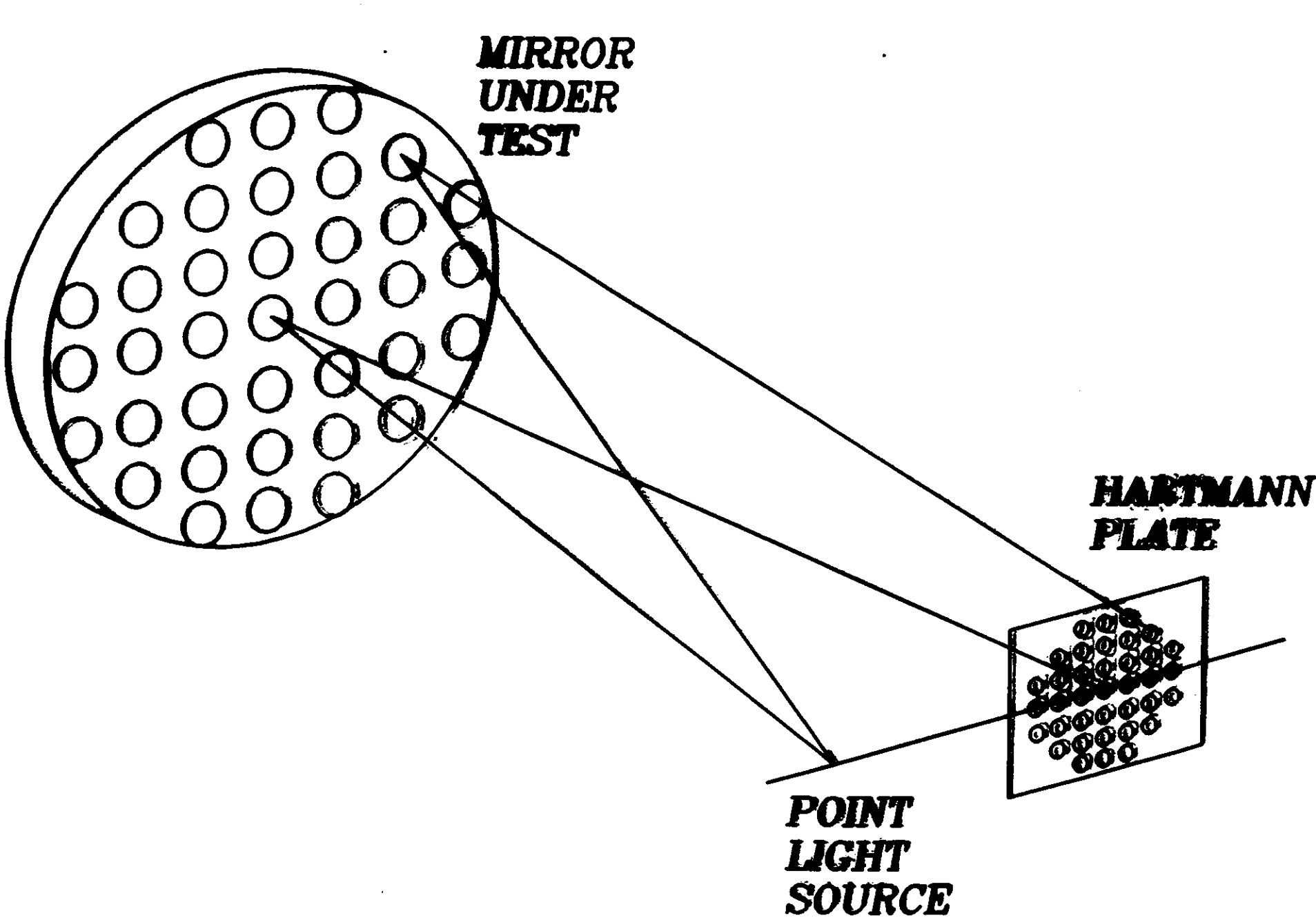
MIRROR
UNDER
TEST
HARTMANN
PLATE
POINT
LIGHT
SOURCE

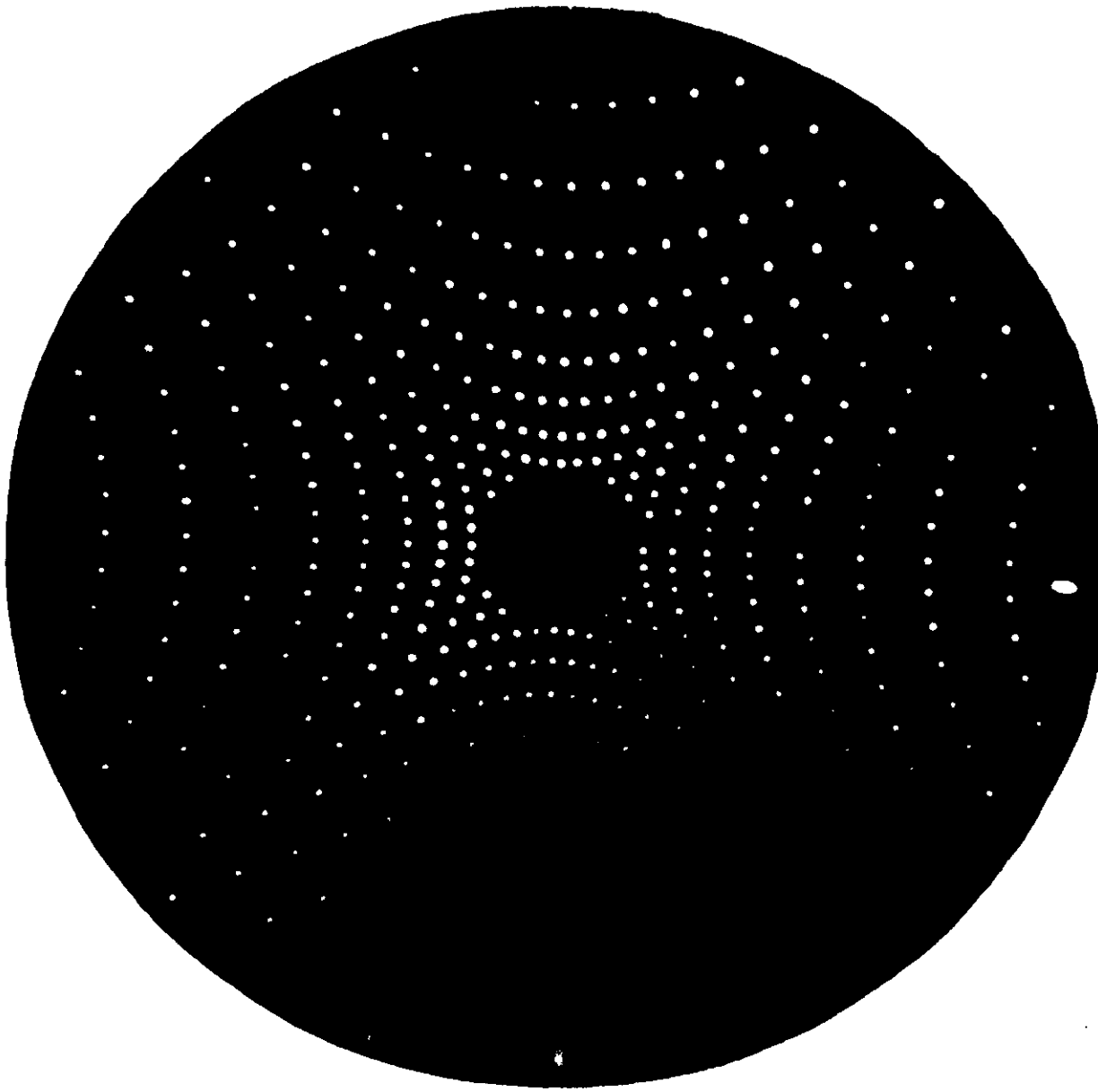

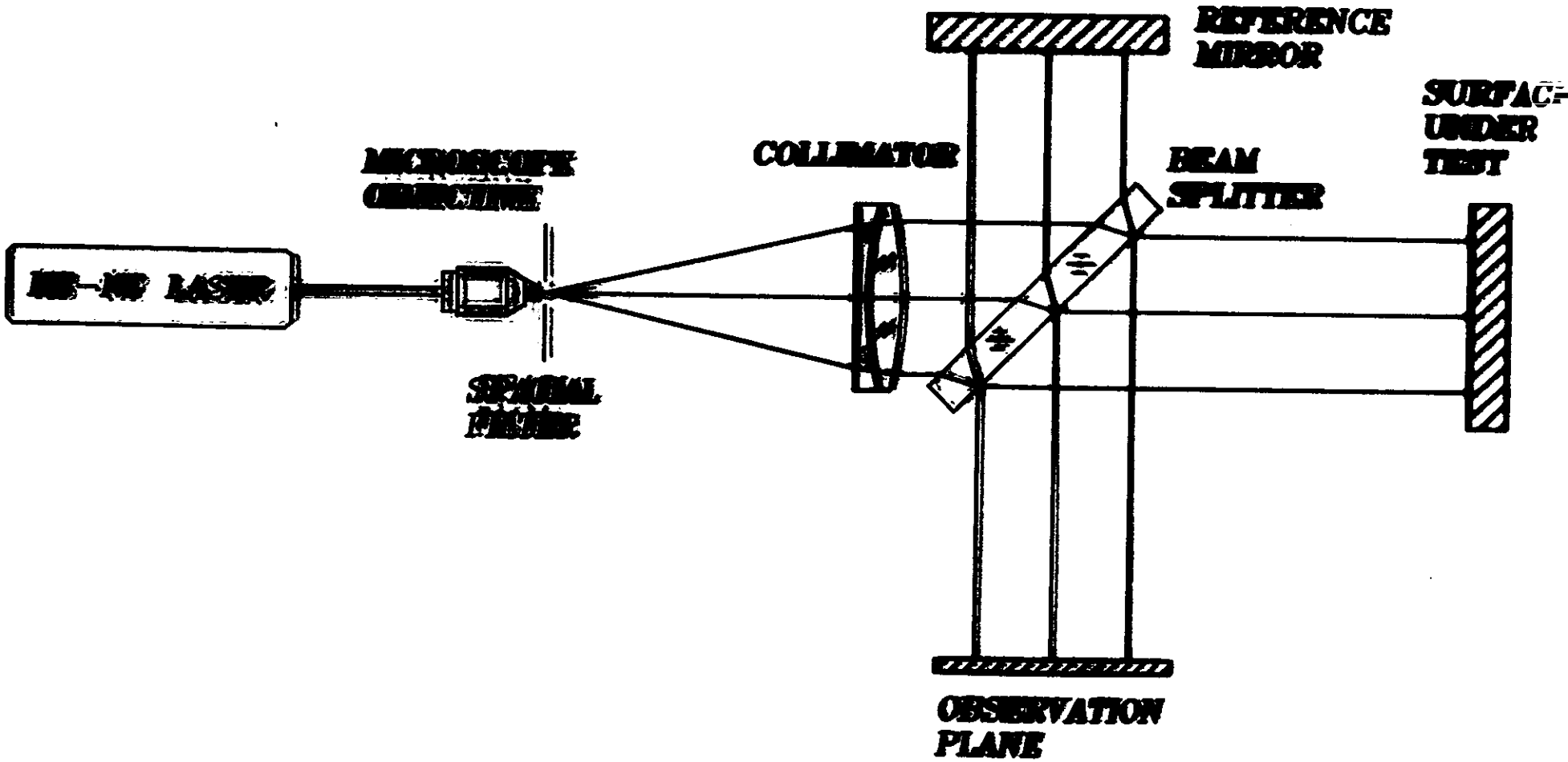
REFERENCE
MIRROR
SURFACE
UNDER
TEST
COLLIMATOR
BEAM
SPLITTER
OBSERVATION
PLANE

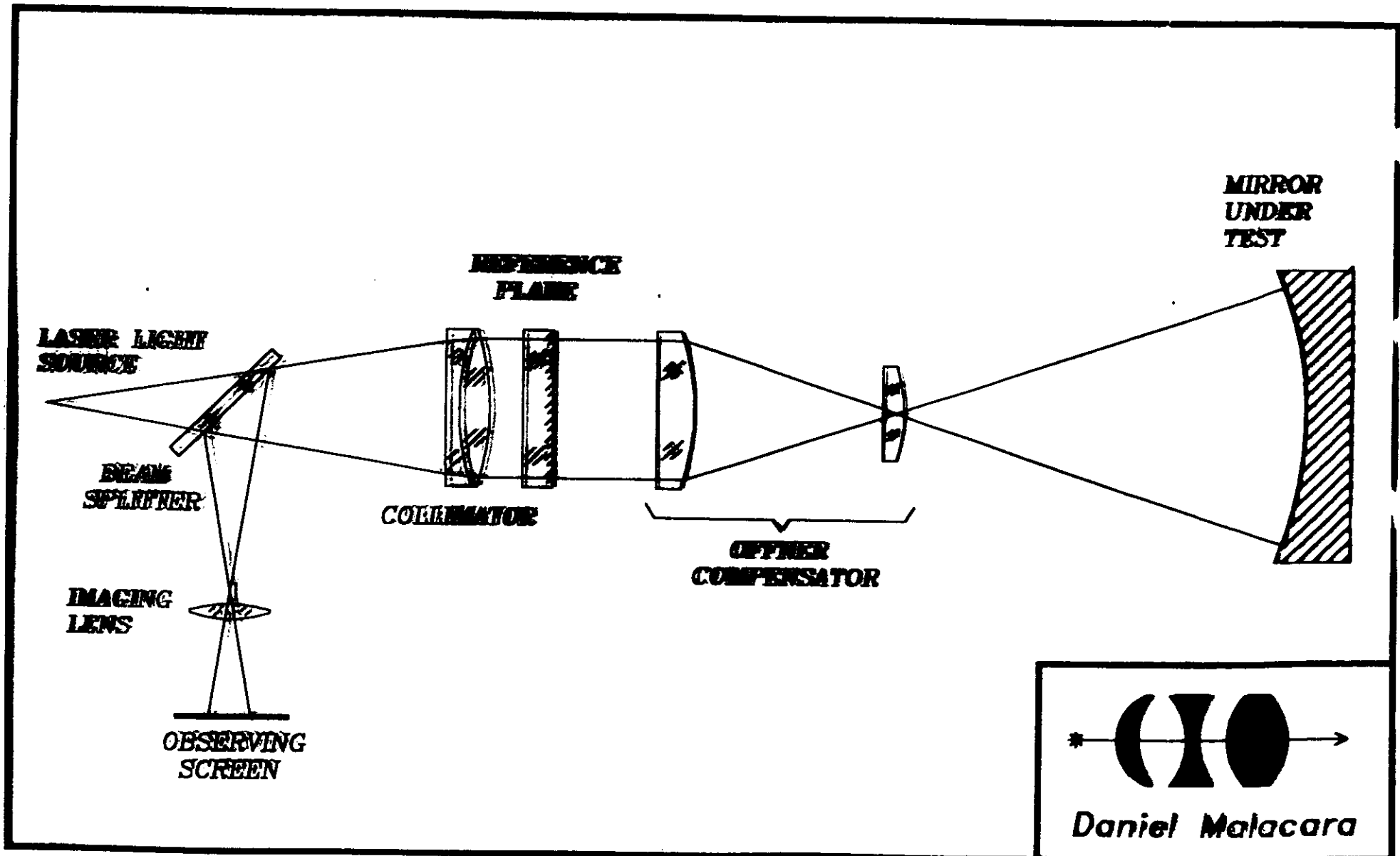
MIRROR UNDER TEST
REFERENCE PLANE
LASER LIGHT SOURCE
BEAM SPLITTER
COLLIMATOR
OFFNER COMPENSATOR
IMAGING LENS
OBSERVING SCREEN
Daniel Malacara

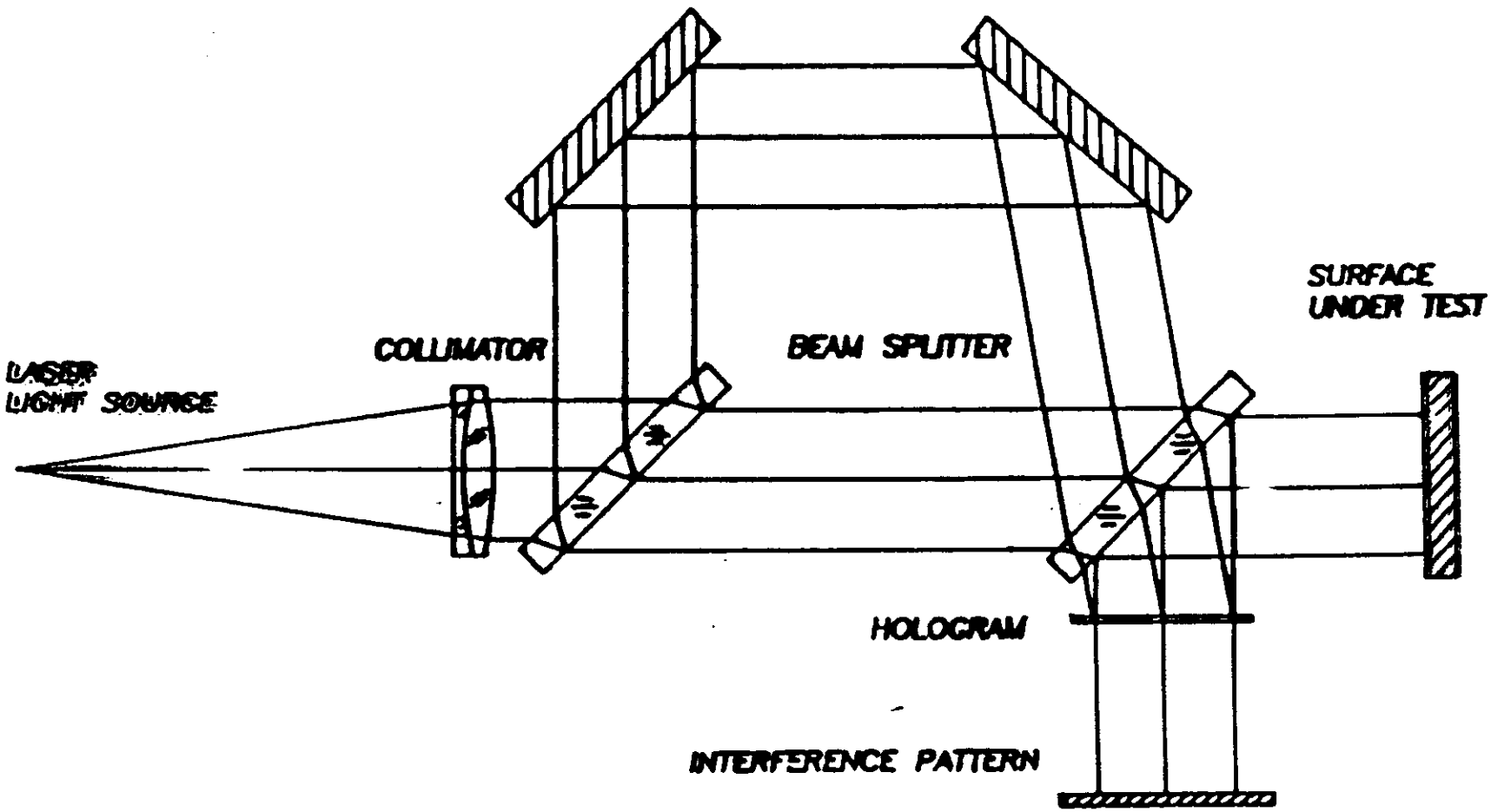

Figure 24.- An optical arrangement for testing an aspherical wavefront with a computer generated hologram.

NO ABERRATION

NO TILT
NO DEFOCUSING

TILT

DEFOCUSING

DEFOCUSING
AND TILT

SPHERICAL ABERRATION

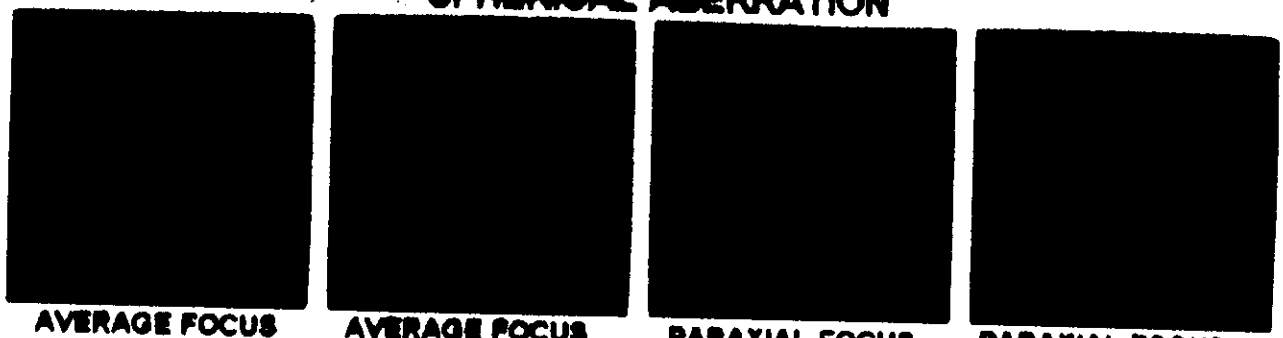

AVERAGE FOCUS

AVERAGE FOCUS
AND TILT

PARAXIAL FOCUS

PARAXIAL FOCUS
AND TILT

COMA

NO TILT
NO DEFOCUSING

DEFOCUSING

TILT IN TANGENCIAL
DIRECTION

TILT IN SAGITTAL
DIRECTION

ASTIGMATISM

SAGITTAL FOCUS

BEST FOCUS

TANGENCIAL FOCUS

DEFOCUSING

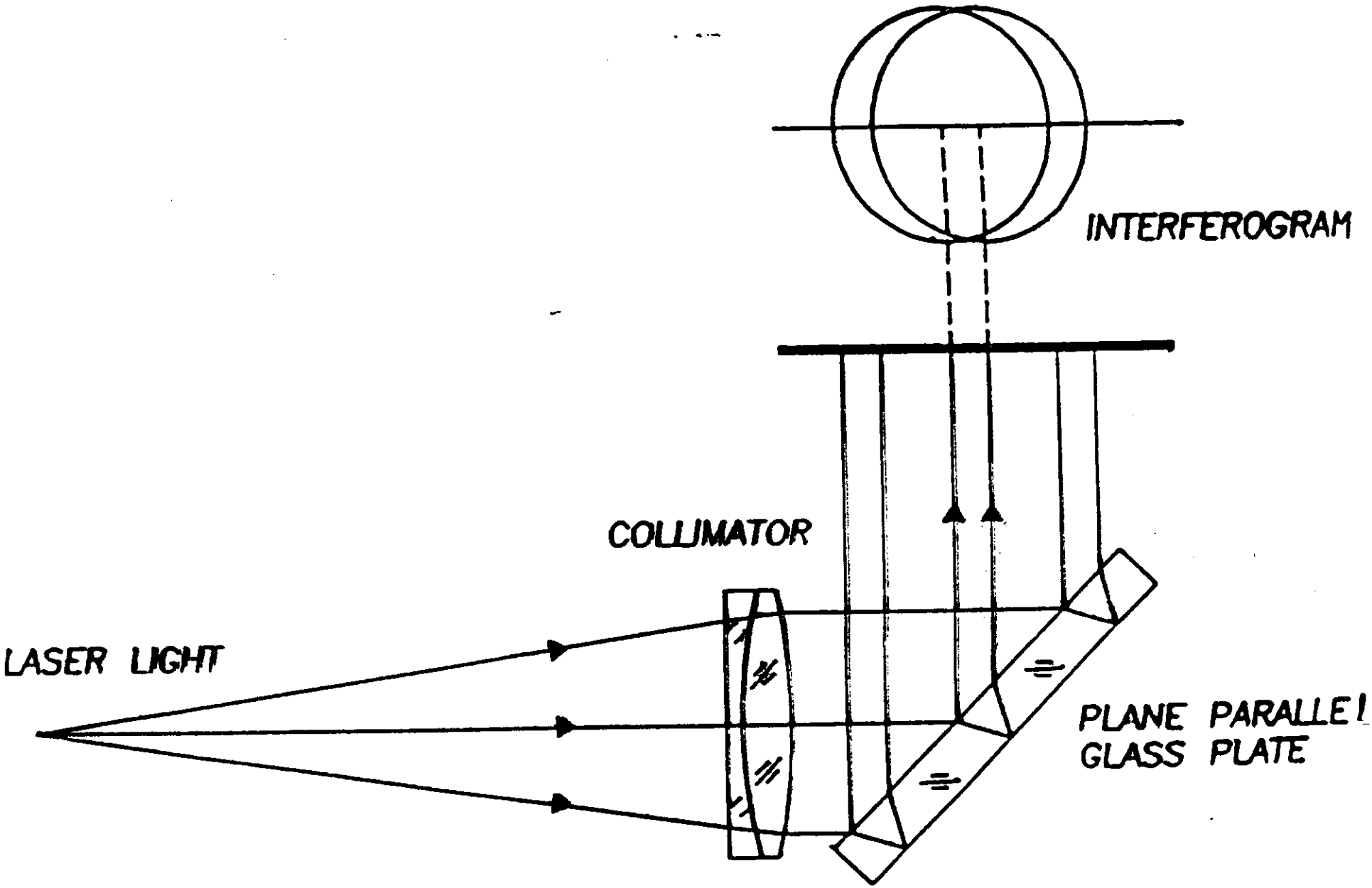

Figure 11.- Murty's lateral shear interferometer.

SHEARING INTERFEROMETERS

The reference wavefront laterally displaced with respect to the other.

The optical path difference OPD(x,y) and the wavefront deformations W(x,y) are related by

$$OPD(x,y) = W(x, y) - W(x - S, y)$$

S is the lateral shear.

If the shear is small, this expression may be approximated by

$$OPD(x, y) = - S \frac{\partial W(x, y)}{\partial x} = - \frac{S}{r} TA_x(x, y)$$

There are also radial, rotational and reversal shearing interferometers

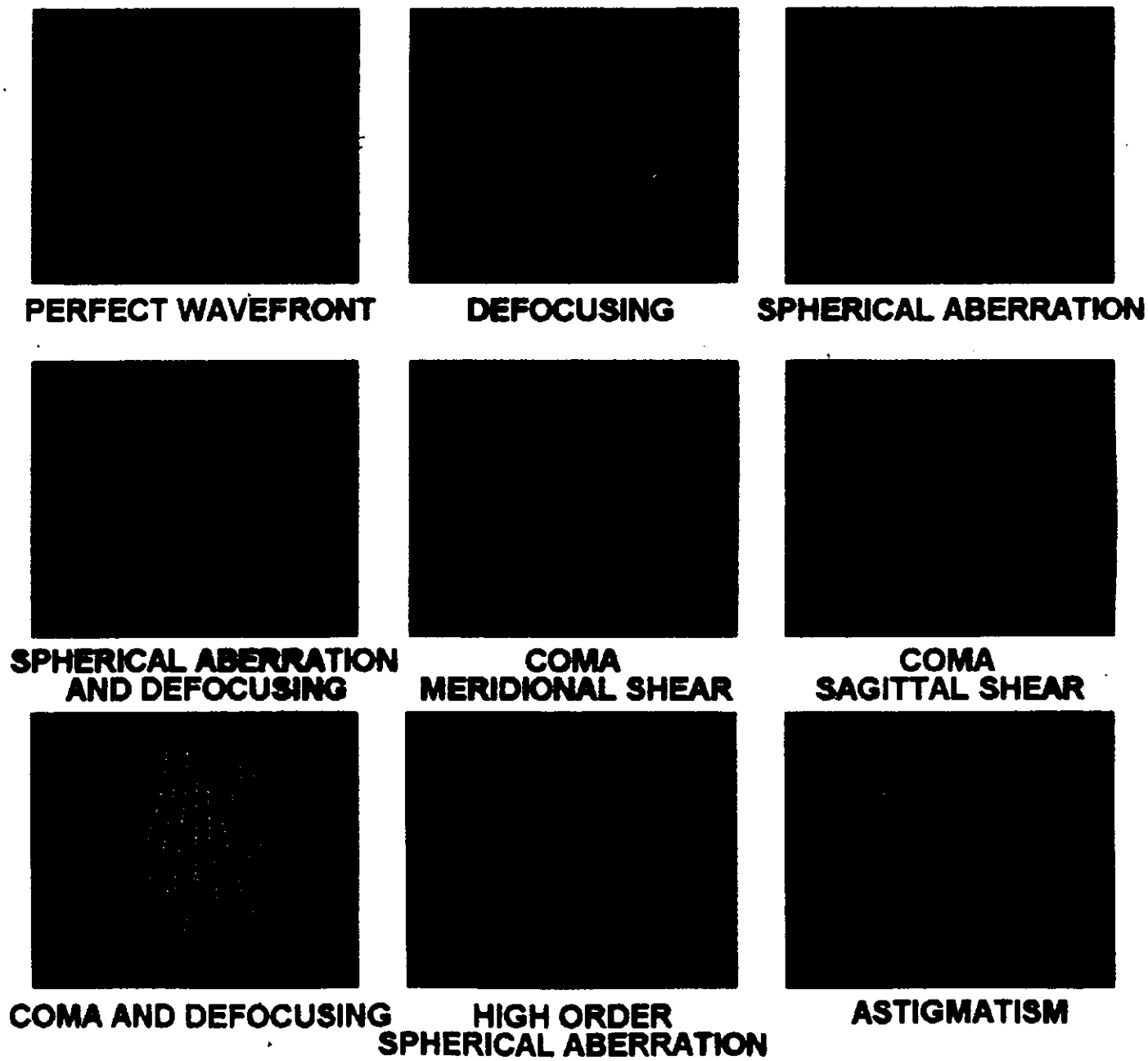
PERFECT WAVEFRONT
DEFOCUSING
SPHERICAL ABERRATION
SPHERICAL ABERRATION AND DEFOCUSING
COMA MERIDIONAL SHEAR
COMA SAGITTAL SHEAR
COMA AND DEFOCUSING
HIGH ORDER SPHERICAL ABERRATION
ASTIGMATISM

FIXED INTERFEROGRAM EVALUATION

The measurements are made with:

Measuring microscope, digitizing tablet or video camera connected to a computer.

To analyze fringes with a computer, they must be digitized, locating fringe centers, and assigning fringe order numbers to them.

$$OPD = m\lambda$$

where m is the fringe order. Any value of the fringe order may be assigned to the first fringe. For the second fringe, order may be increased or decreased by one.

This choice affects the sign of the OPD.

A disadvantage of the fixed interferogram analysis is that the sign of the OPD can be obtained only if the sign of any term, like defocusing or tilt, is previously determined.

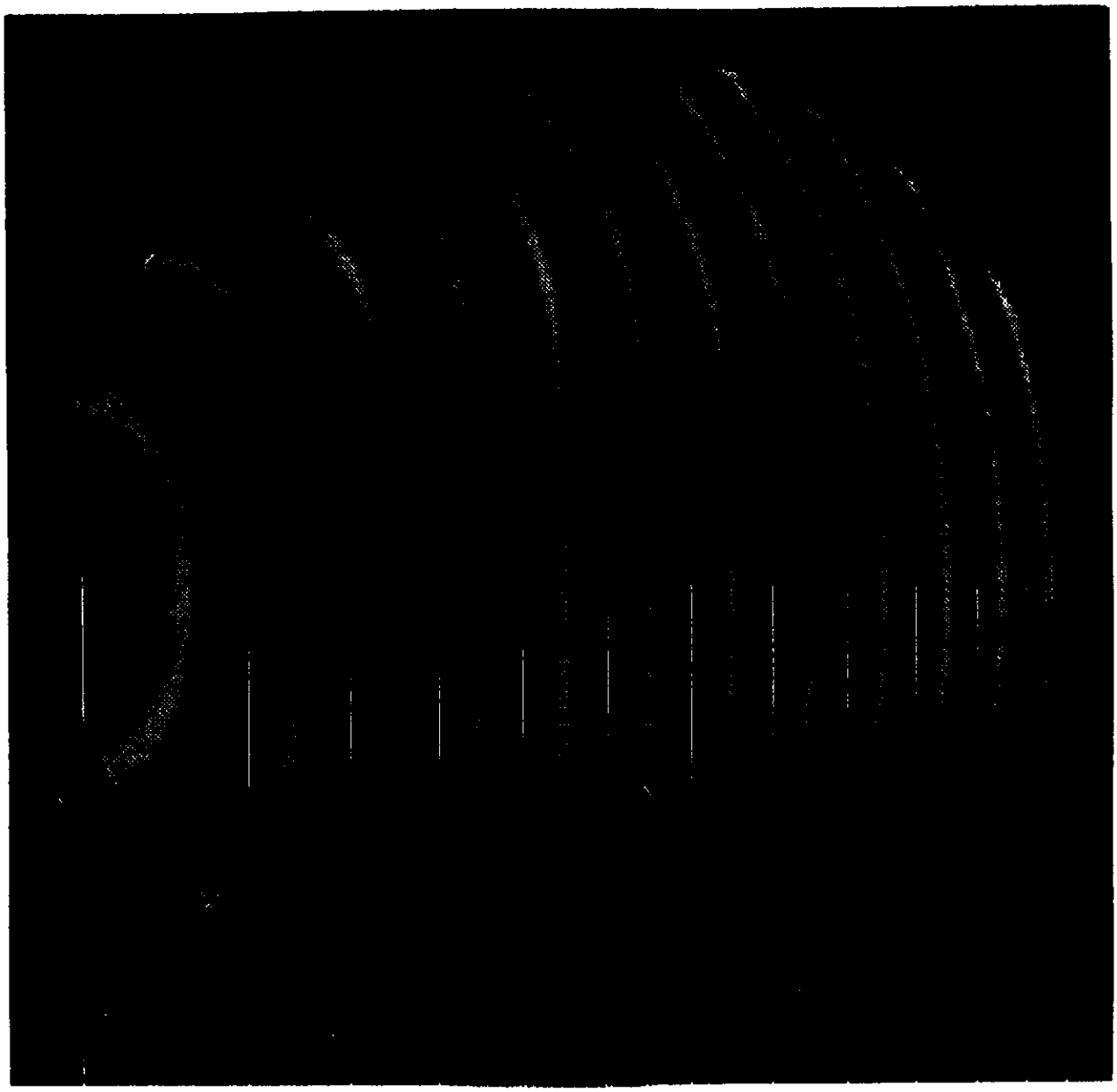
1 2 3 4 5 6 7 8 9 10 11 12 13

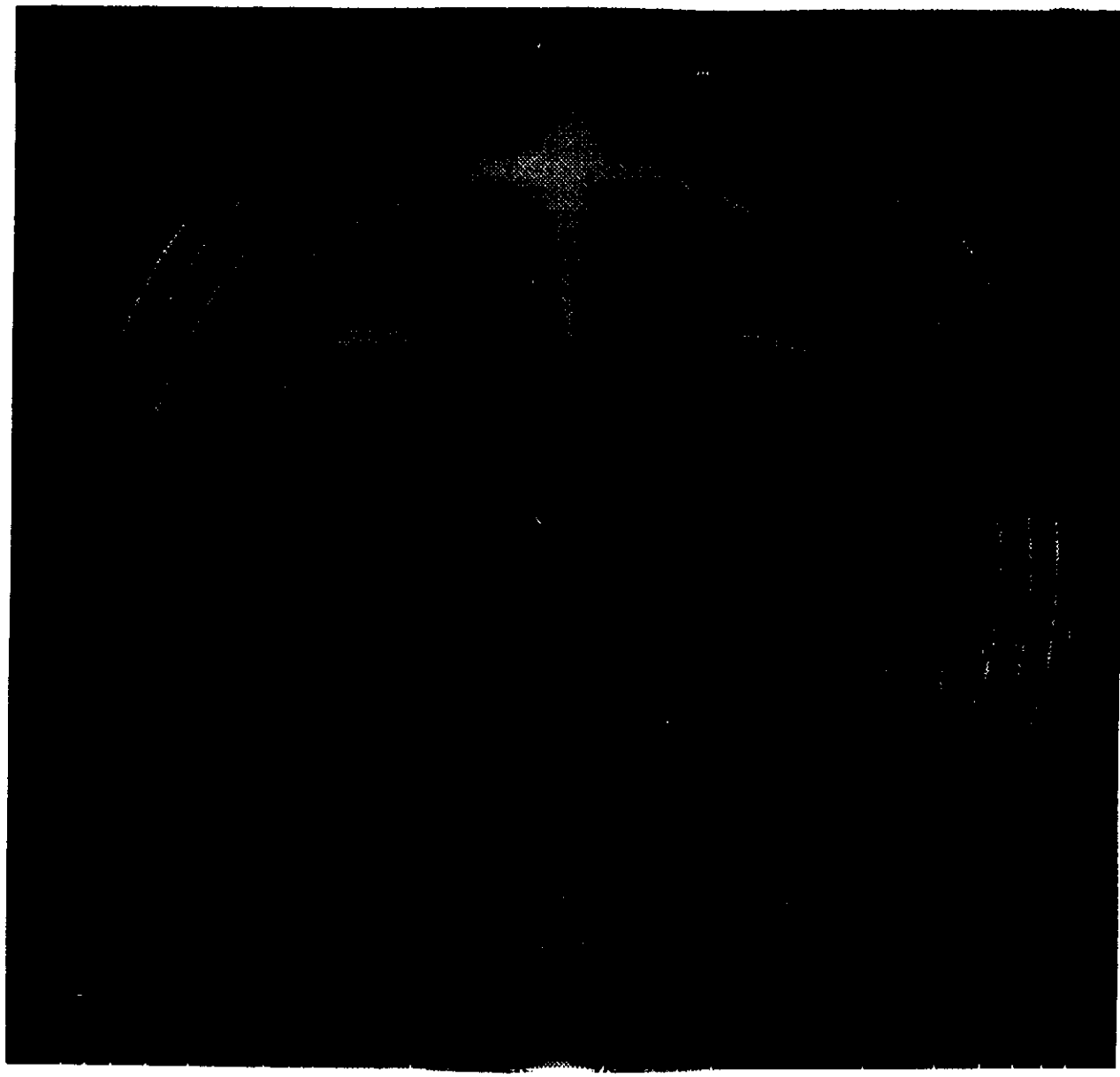

1234 5 6 6 5 4 3 3 4 5678

GLOBAL AND LOCAL INTERPOLATION OF INTERFEROGRAMS

Global interpolation by least-squares fitting of the measured data to a two-dimensional polynomial.

A least squares fitting begins by defining the variance σ of the discrete wavefront fitting, as follows:

$$\sigma = \frac{1}{N} \sum_{i=1}^{N} \left[W_i' - W(\rho_i, \theta_i) \right]^2$$

where N is the number of data points,

W_i' is the measured wavefront deviation for the data point i.

$W(\rho_i, \theta_i)$ is the functional wavefront deviation after the polynomial fitting.

This variance or fit error is minimized.

LEAST SQUARES METHOD

The standard approach is to fit the measured points to a linear combination of polynomials that are orthogonal over the discrete set of data points. Thus, the wavefront is represented by

$$W(\rho_i, \theta_i) = \sum_{n=1}^{L} B_n V_n(\rho_i, \theta_i)$$

$V(\rho, \theta)$ are polynomials of degree r and not the monomials x^r. These polynomials satisfy the orthogonality condition

$$\sum_{i=1}^{N} V_n(\rho_i, \theta_i) V_m(\rho_i, \theta_i) = F_n \delta_{nm}$$

where $F_n = \sum V_n^2$

The matrix of the system becomes diagonal and there is no need to invert it.

To obtain the orthogonal polynomials by means of the Gram-Schmidt orthogonalization procedure.

ZERNIKE POLYNOMIALS

The polynomials $\underline{V}_r$ approach the Zernike polynomials.

We may add or subtract one or more polynomial terms without affecting the fit coefficients of the other terms.

A better choice for the wavefront representation is the set of Zernike polynomials, which are orthogonal on the circle with unit radius, as follows

$$\int_0^1 \int_0^{2\pi} U_n(\rho, \theta)\, U_m(\rho, \theta)\, \rho\, d\rho\, d\theta = F_{nm}\, \delta_{nm}$$

These polynomials are not exactly orthogonal on the set of data points. It is common to transform the wavefront representation in terms of the polynomials $\underline{V}_n$ to another similar representation in terms of Zernike polynomials $\underline{U}_n$, as

$$W(\rho, \theta) = \sum_{n=1}^{L} A_n\, U_n(\rho, \theta)$$

PHASE SHIFTING INTERFEROMETRY

Static fringe analysis is generally less precise than phase shifting interferometry, by more than one order of magnitude.

Phase shifting interferometry requires several images, acquired over a long time interval during which the fringes must be stable.

The reference wavefront is moved along the direction of propagation, with respect to the wavefront under test, changing in this manner their phase difference.

This phase shifting is made in steps or in a continuous manner.

Measuring the irradiance changes for different values of the phase shifts, is possible to determine wavefront under test.

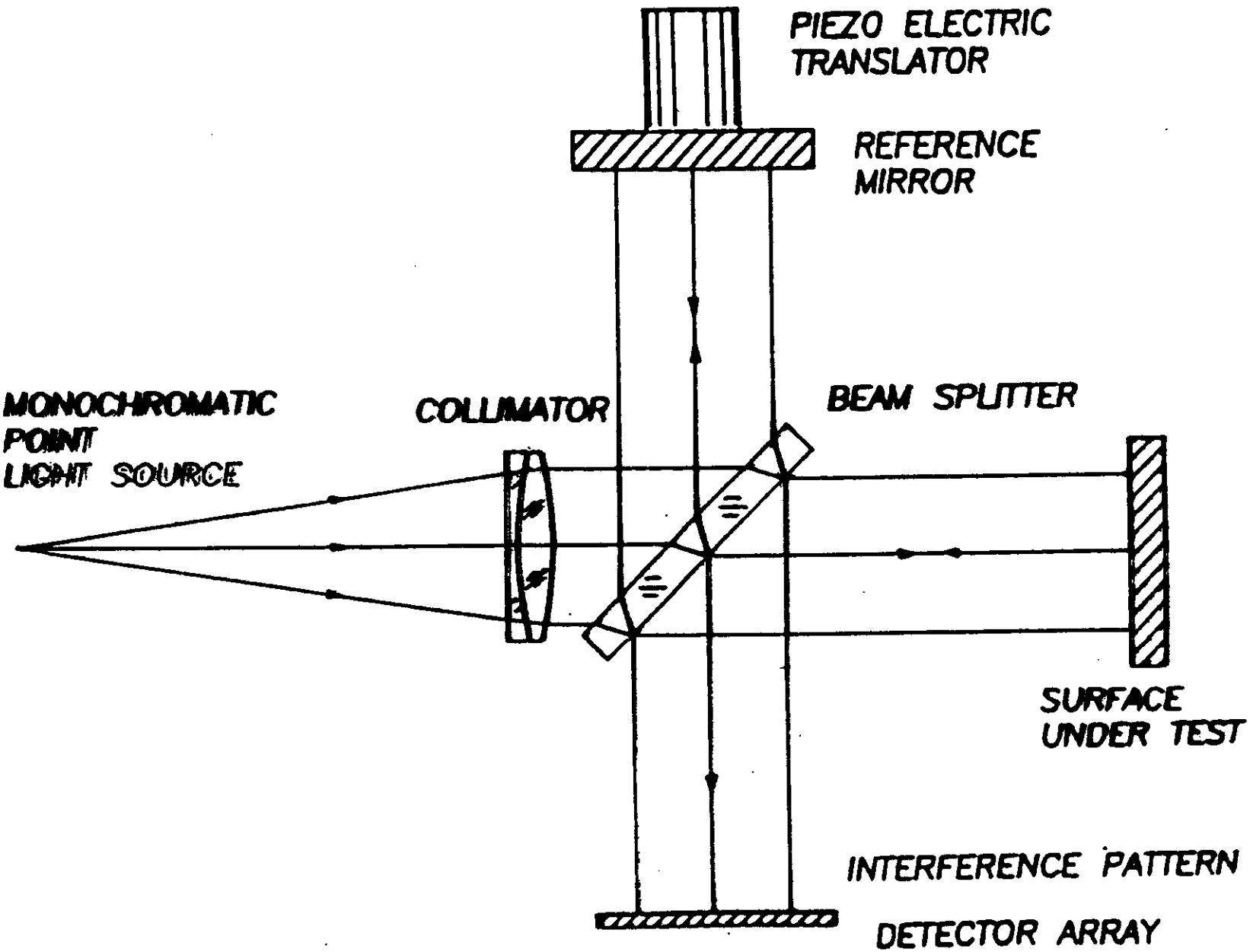

Figure 14.- Twyman-Green interferogram adapted to do phase shifting.

MOVING MIRROR

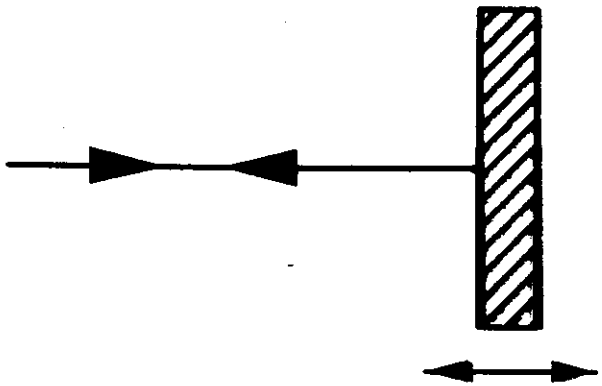

(a)

ROTATING GLASS PLATE

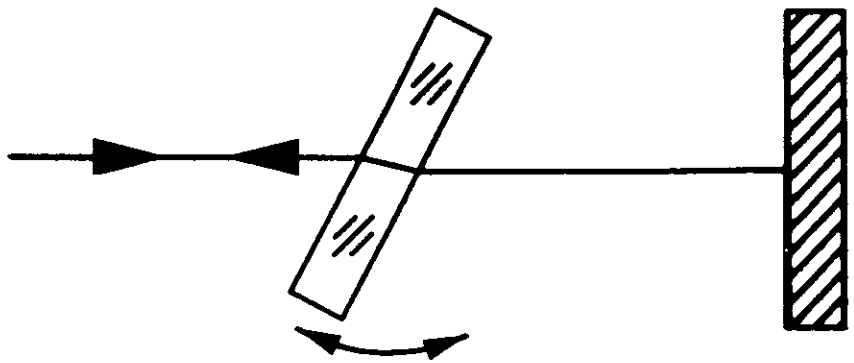

(b)

MOVING GRATING

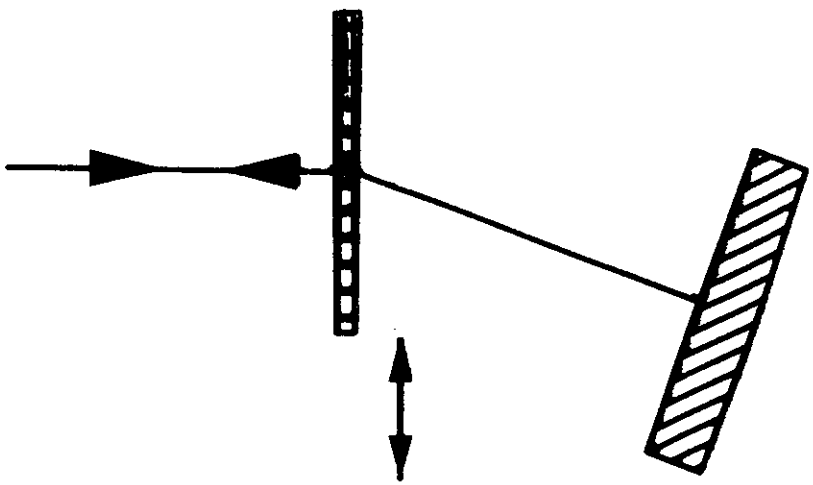

(c)

BRAGG CELL

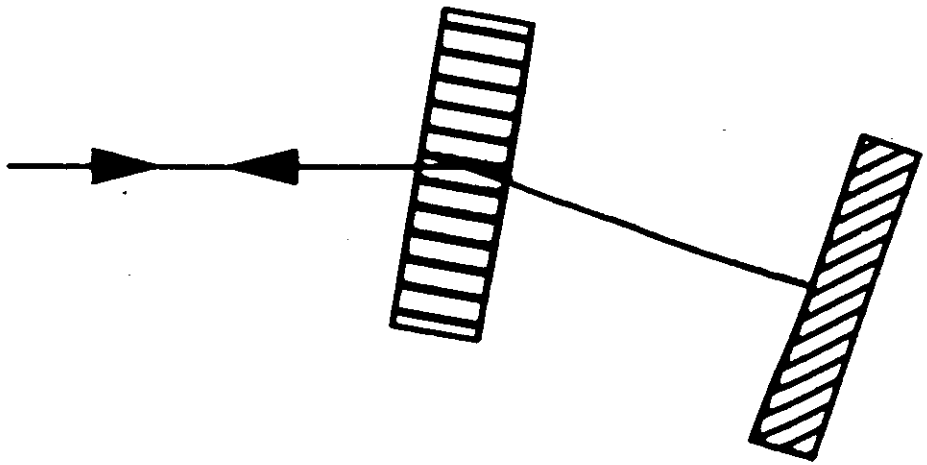

(d)

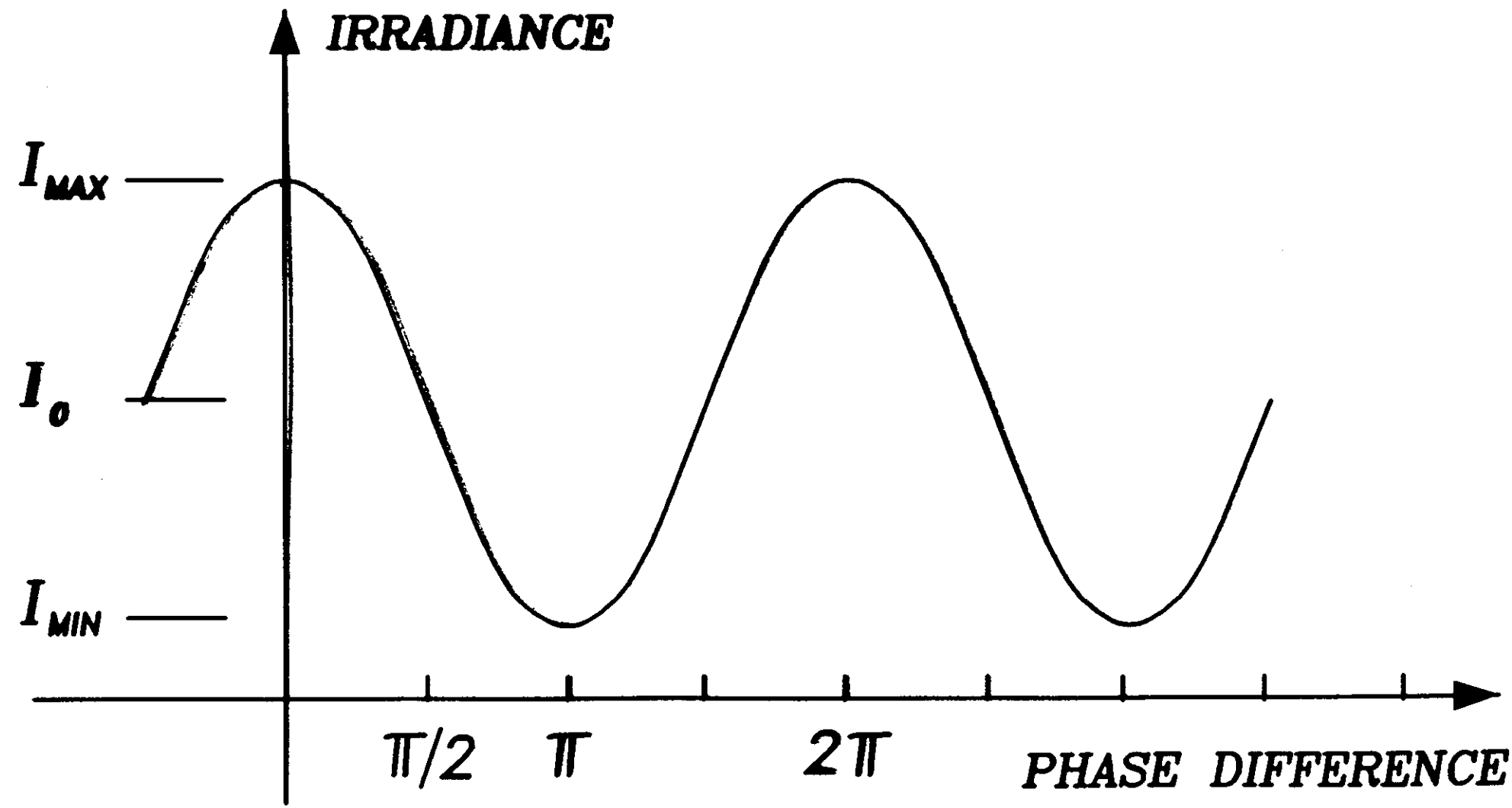
IRRADIANCE
I_{MAX}
I_0
I_{MIN}
π/2
π
2π
PHASE DIFFERENCE

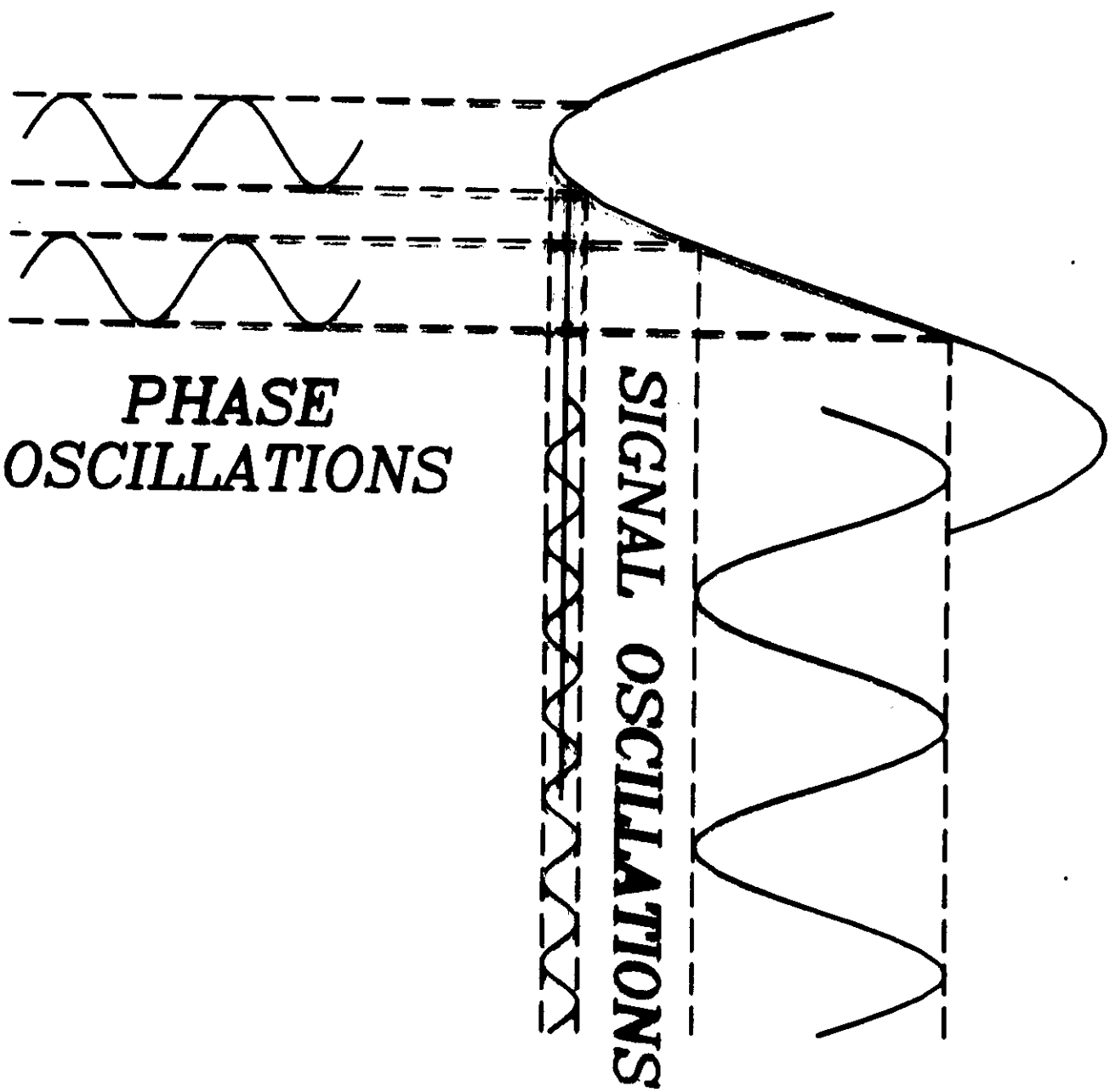
PHASE
OSCILLATIONS
SIGNAL OSCILLATIONS

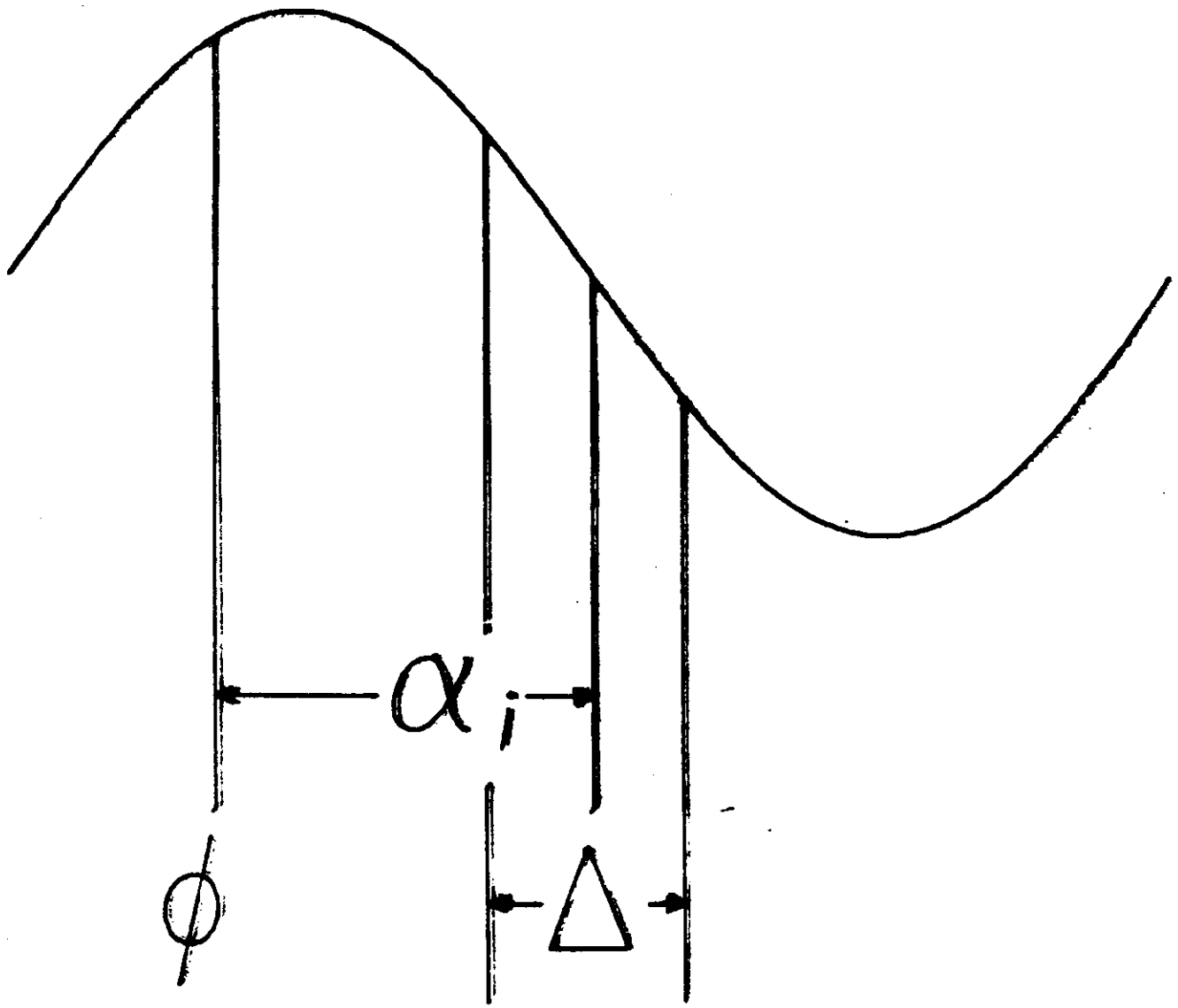

Figure 19.- Averaged signal measurements with the integrating phase shifting method.

DIRECT INTERFEROMETRY (ANALYSIS)

The phase-modulating function is the wavefront shape $\underline{W(x, y)}$.

If ϕ_0 is a multiple of 2π, this expression may be rewritten as

$$I = I_1 + I_2 + 2\sqrt{I_1 I_2}\cos(kx \sin\theta + kW)$$

Multiplying this phase modulated function by a signal $\sin(kx \sin\theta)$ a signal $\underline{S}$ is obtained, and multiplying by a signal $\cos(kx \sin\theta)$ a signal $\underline{C}$ is obtained. If high frequency terms in the signals $\underline{S}$ and $\underline{C}$ are removed with a low pass filter, they become

$$S(x,y) = -\sqrt{I_1 I_2}\sin kW(x,y)$$

$$C(x,y) = \sqrt{I_1 I_2}\cos kW(x,y)$$

then, the wavefront $\underline{W(x,y)}$ is given by

$$W(x,y) = -\frac{1}{k}\tan^{-1}\left[\frac{S(x,y)}{C(x,y)}\right]$$

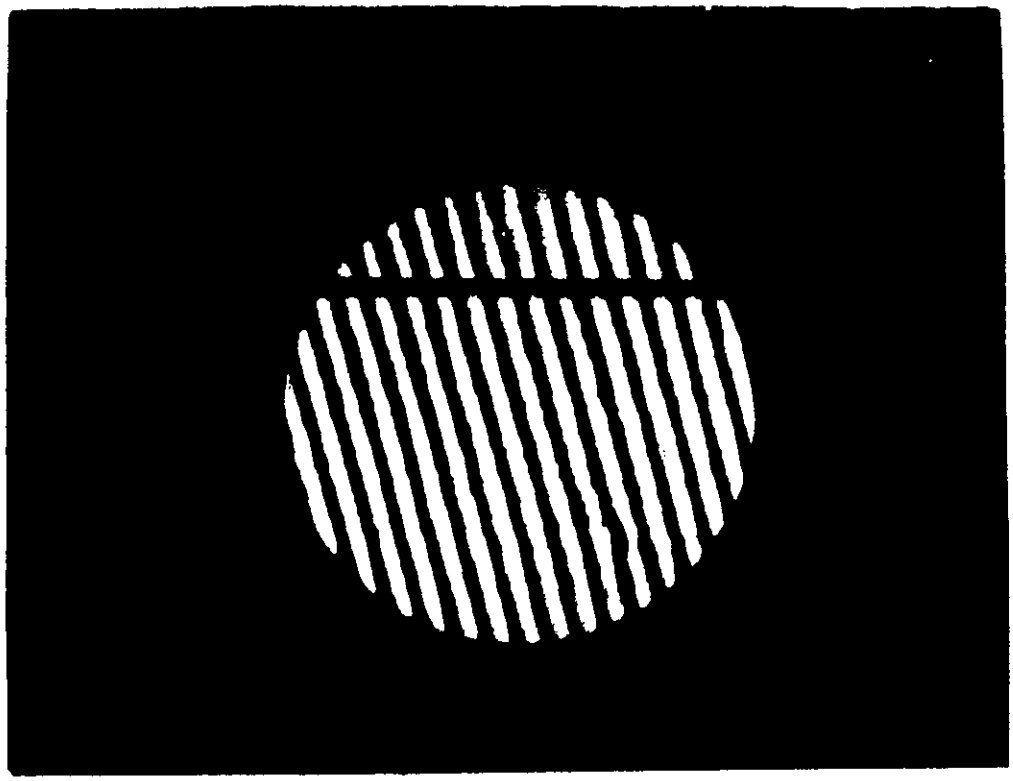

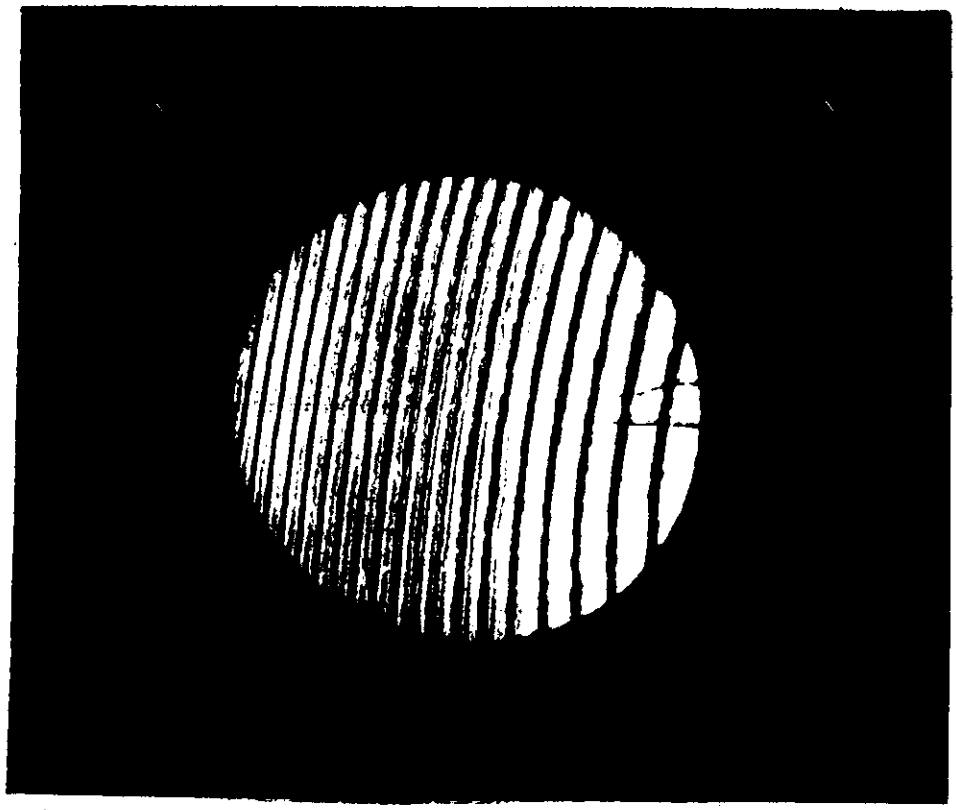

INTERFEROGRAM INTERPRETATION:

a) As a hologram of the wavefront $W(x, y)$, with a reference wavefront. The interferogram with a flat reference wavefront W_R at an angle θ_R given by

$$E_r(x, y) = \exp(i\, k\, x \sin\theta_R) \tag{5}$$

Thus we obtain:

$$E_R(x, y) \cdot I(x, y) = K(x, y) \cdot \exp(i\, k\, x \sin\theta_R) =$$

$$(I_1 + I_2) \exp(i\, k\, x \sin\theta_R)$$

$$- \sqrt{(I_1\, I_2)} \exp\, i\, k\, [\, x \sin\theta_o + x \sin\theta_R + W(x, y)] \tag{6}$$

$$- \sqrt{(I_1\, I_2)} \exp - i\, k\, [\, x \sin\theta_o - x \sin\theta_R + W(x, y)]$$

FOURIER INTERFEROMETRY

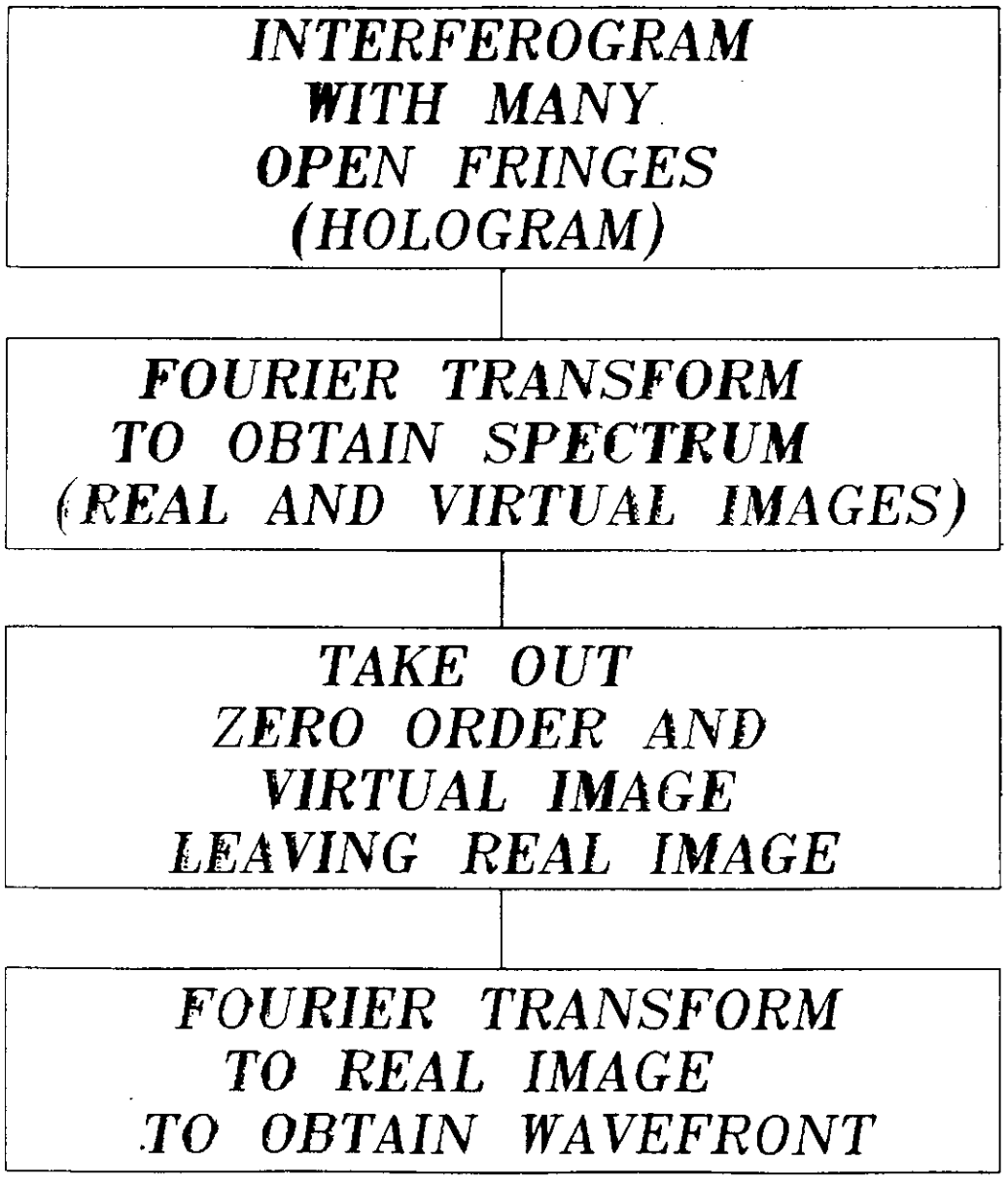

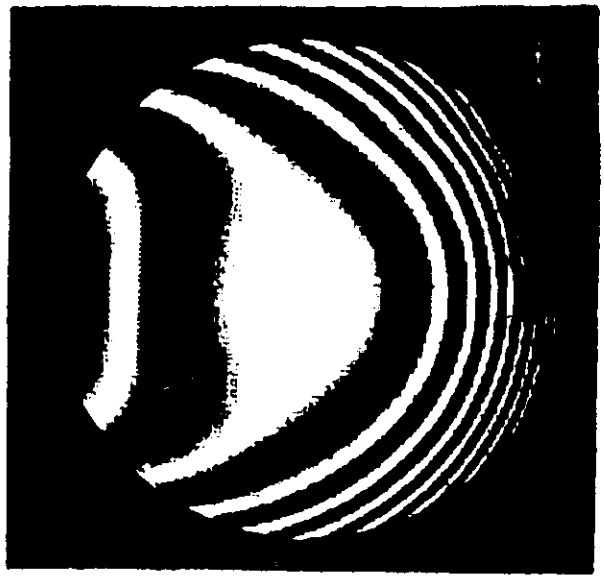

(a)

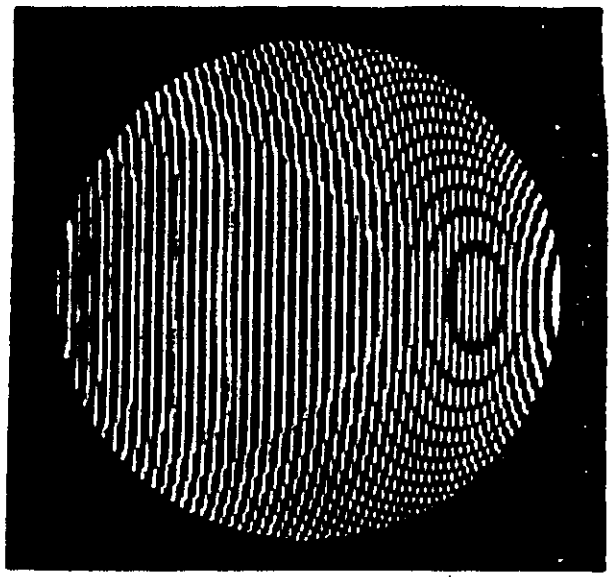

(b)

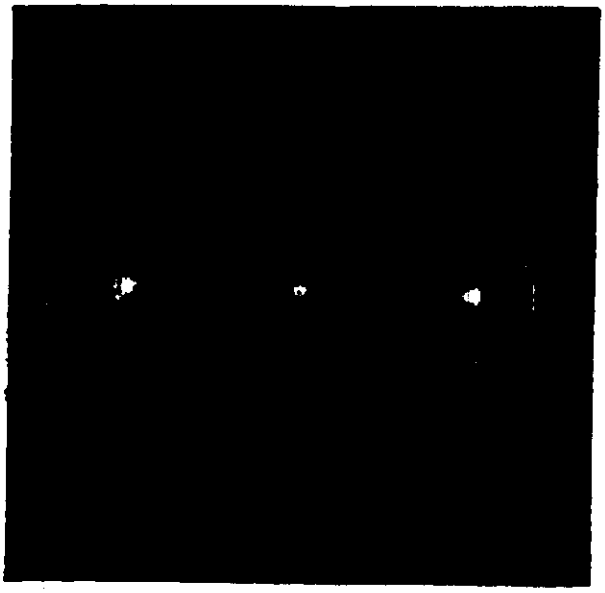

(c)

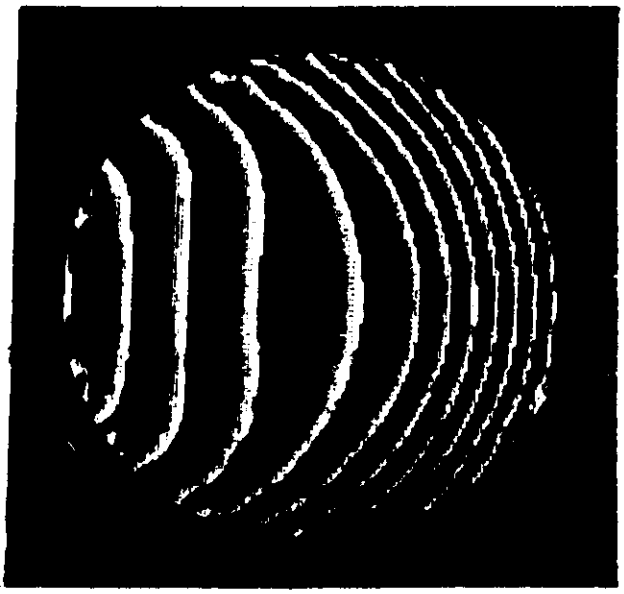

(d)

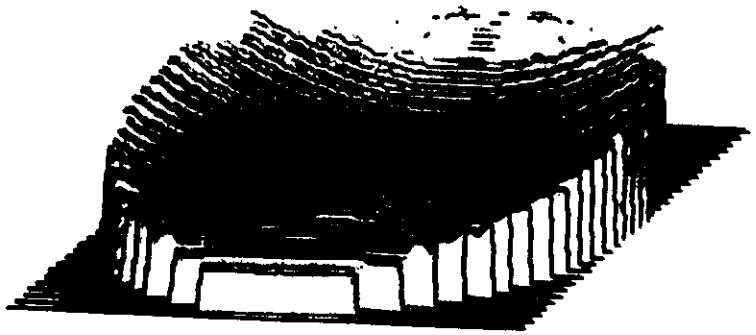

(e)

TESTING ASPHERICAL WAVEFRONTS:

Null tests:

Use Compensators

Perfect wavefronts produce straight, parallel and equidistant fringes

Defocusing, there is no maximum fringe period

Non Null tests:

Do not use any compensator

Perfect wavefronts produce non-straight fringes with variable separations

Defocusing, there is a maximum fringe period

Daniel Malacara

COMPENSATORS:

Compensators are used to eliminate the spherical aberration of aspherical surfaces under test

Compensator types:

- a) Refractive
  - Dall (single lens)
  - Offner (two lens)
  - Shafer (three lens)
  - Special configuration (Meinel)
- b) Reflective
  - Burch (two mirror)
  - Offner (two mirror)
- c) Diffractive
  - Photographic hologram
  - Computer generated hologram
- d) Moire
  - Computer generated pattern

Daniel Malacara

REFRACTIVE COMPENSATORS:

Dall (single lens)

- Very critical position
- High order aberrations are introduced

Offner (two lens)

- Critical position and spacing of elements
- High order aberrations are not introduced

Daniel Malacara

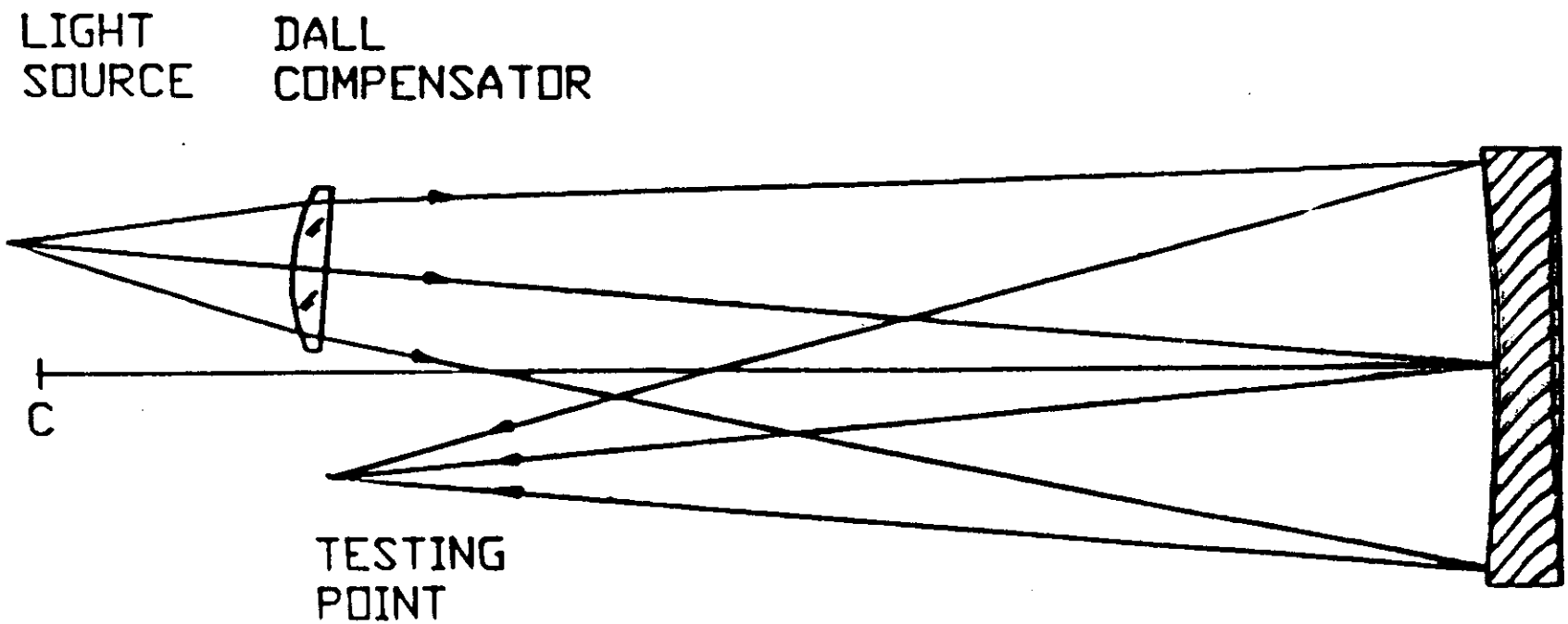

Figure 21.- The Dall compensator.

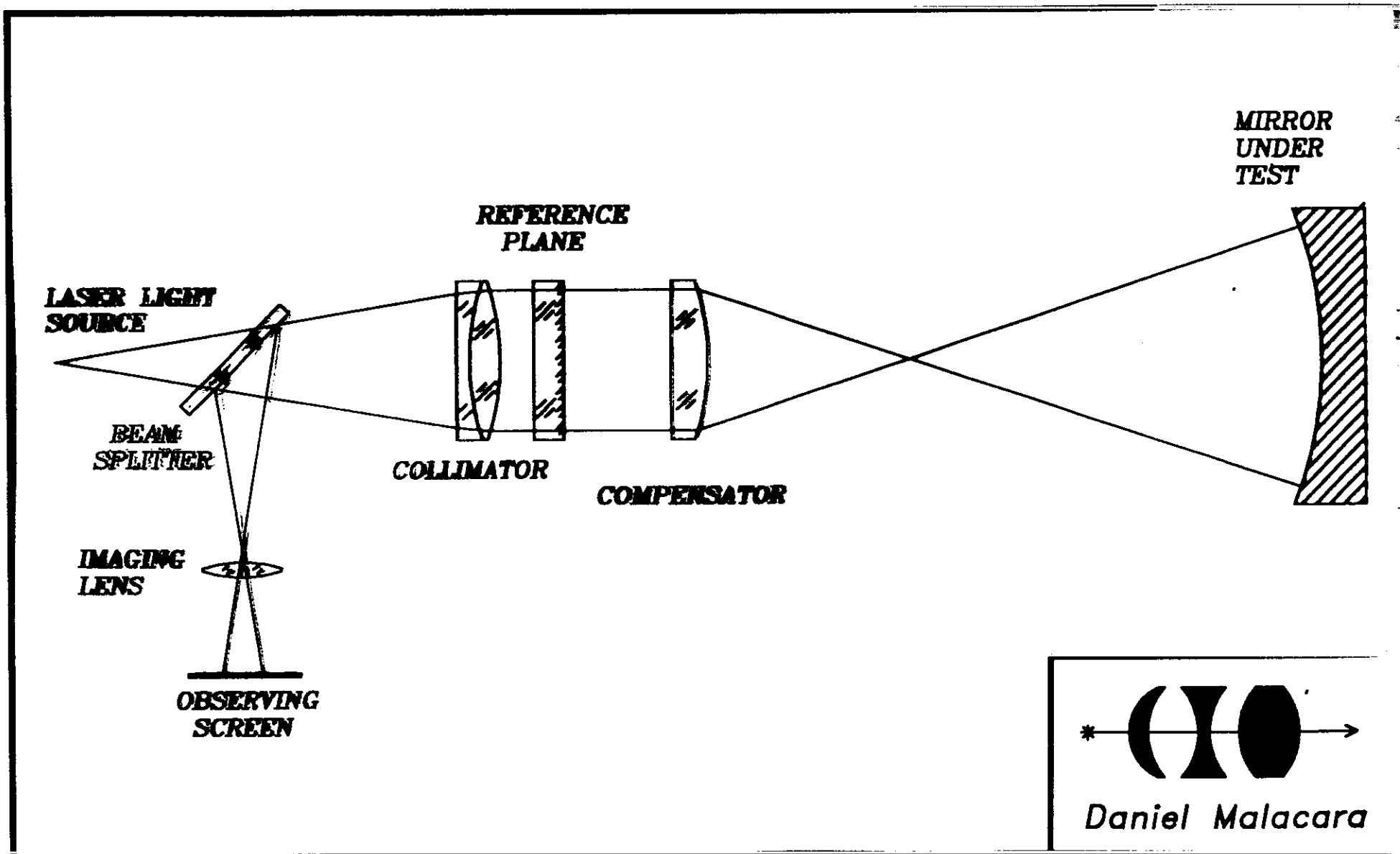
MIRROR
UNDER
TEST
REFERENCE
PLANE
LASER LIGHT
SOURCE
BEAM
SPLITTER
COLLIMATOR
COMPENSATOR
IMAGING
LENS
OBSERVING
SCREEN
Daniel Malacara

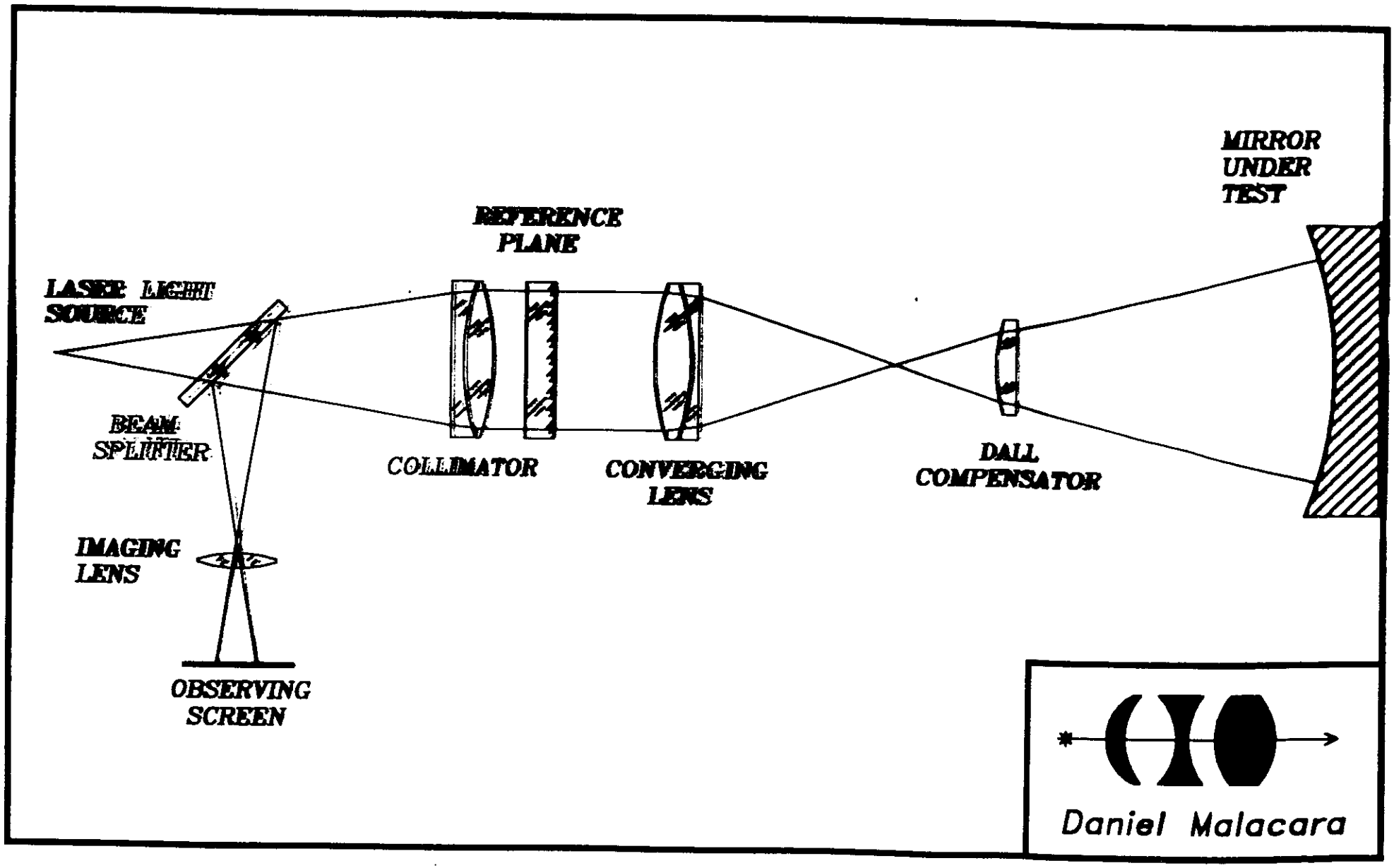
MIRROR
UNDER
TEST
REFERENCE
PLANE
LASER LIGHT
SOURCE
BEAM
SPLITTER
COLLIMATOR
CONVERGING
LENS
DALL
COMPENSATOR
IMAGING
LENS
OBSERVING
SCREEN
Daniel Malacara

SOME NULL TEST CONFIGURATIONS:

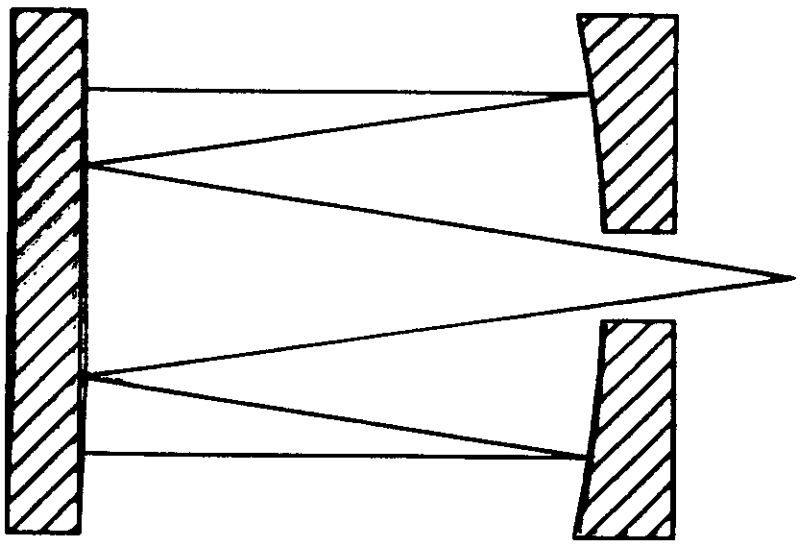

Autocollimation test for paraboloids

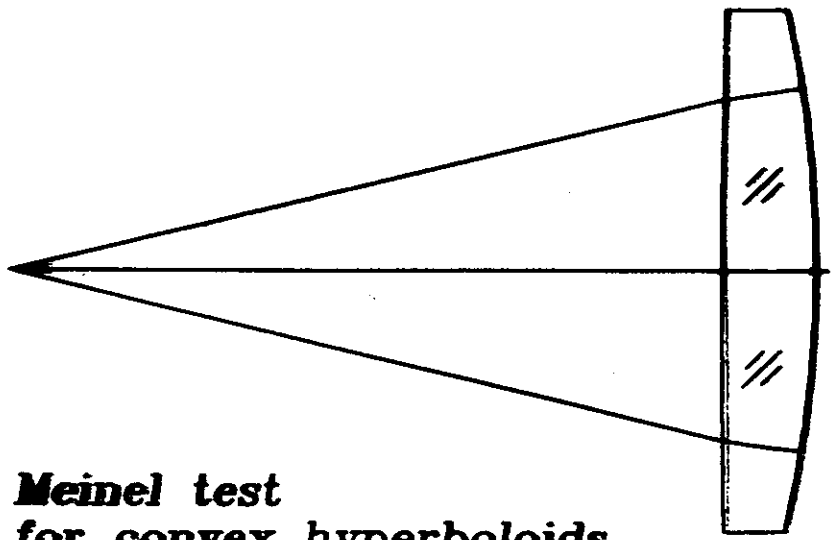

Meinel test for convex hyperboloids

Daniel Malacara

DIFFRACTIVE COMPENSATORS:

Low light efficiency

First diffraction order must be isolated

Photographic hologram

An initial perfect system is necessary to make it

Easy to manufacture

Computer generated hologram

No initial perfect system necessary

Manufacture not so simple

Daniel Malacara

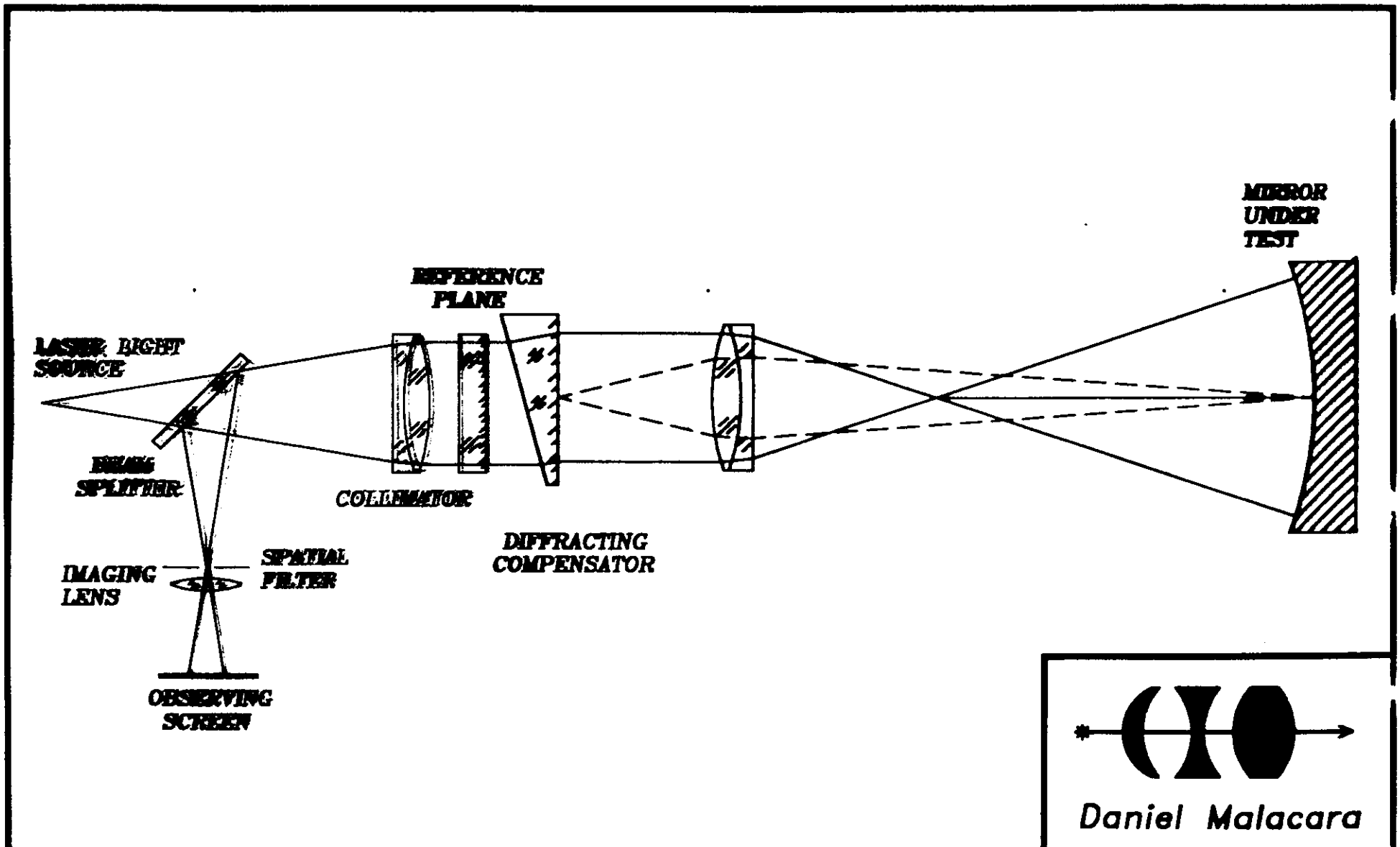
MIRROR
UNDER
TEST
REFERENCE
PLANE
LASER LIGHT
SOURCE
BEAM
SPLITTER
COLLIMATOR
DIFFRACTING
COMPENSATOR
IMAGING
LENS
SPATIAL
FILTER
OBSERVING
SCREEN
Daniel Malacara

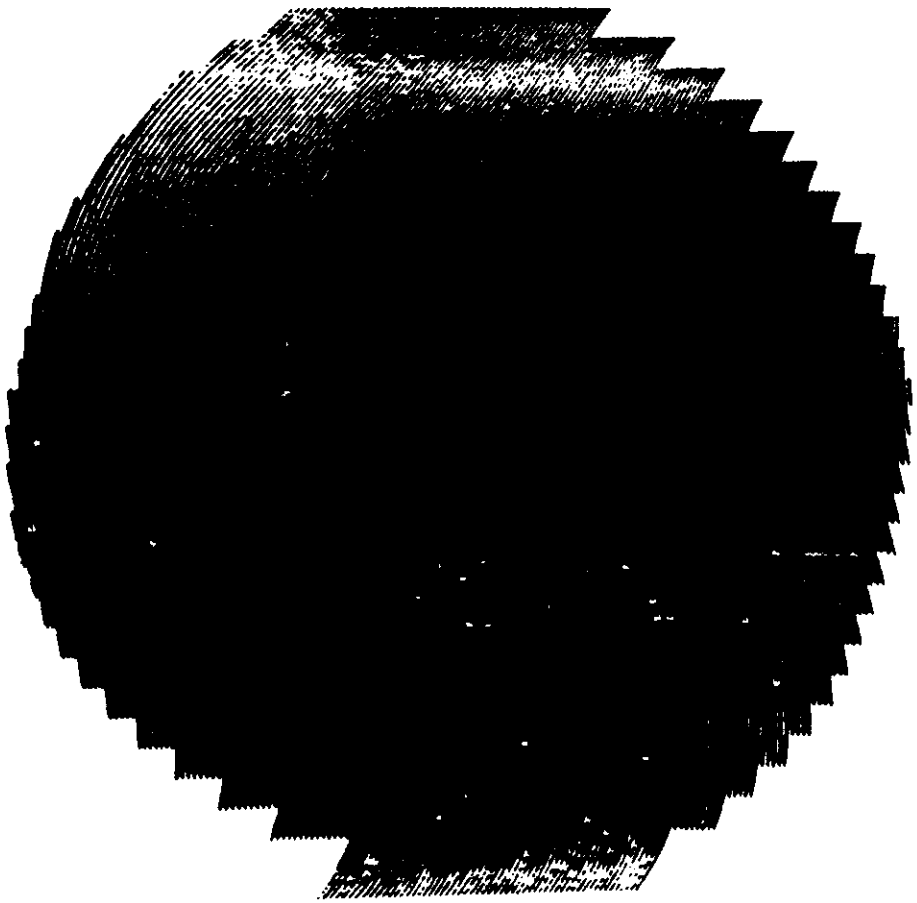

Figure 23.- Computer generated hologram for testing an aspherical wavefront. (From Wyant, 1978).

INFRARED INTERFEROMETRY

A simple approach to reduce the number of fringes in the interferogram is to use a long infrared wavelength. Light from a CO_2 laser has been used.

It can be used when the surface is rough.

TWO WAVELENGTH INTERFEROMETRY

Two different wavelengths λ_1 and λ_2 are used simultaneously.

The group (equivalent) wavelength L is longer then λ_1 and λ_2

Asphericity magnitude limited by group wavelength L

Accuracy is limited by wavelength of components

$$L = \frac{\lambda_1 \lambda_2}{\lambda_2 - \lambda_1} \qquad \lambda = \frac{2\lambda_1 \lambda_2}{\lambda_2 + \lambda_1}$$

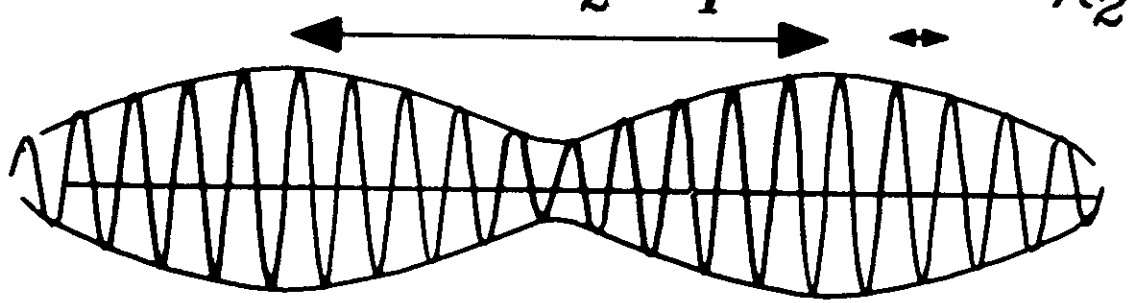

Daniel Malacara

SUB-NYQUIST INTERFEROMETRY

Each detector must have a phase difference smaller than π from the closest neighboring detector, in order to avoid 2π phase ambiguities and ensure phase continuity. there should be at least two detector elements for each fringe. This condition is known as the Nyquist condition.

This condition may be relaxed (Greivenkamp 1987) if the wavefront and its slope are assumed to be continuous on the whole aperture. Then, optical surfaces with larger asphericities may be tested.

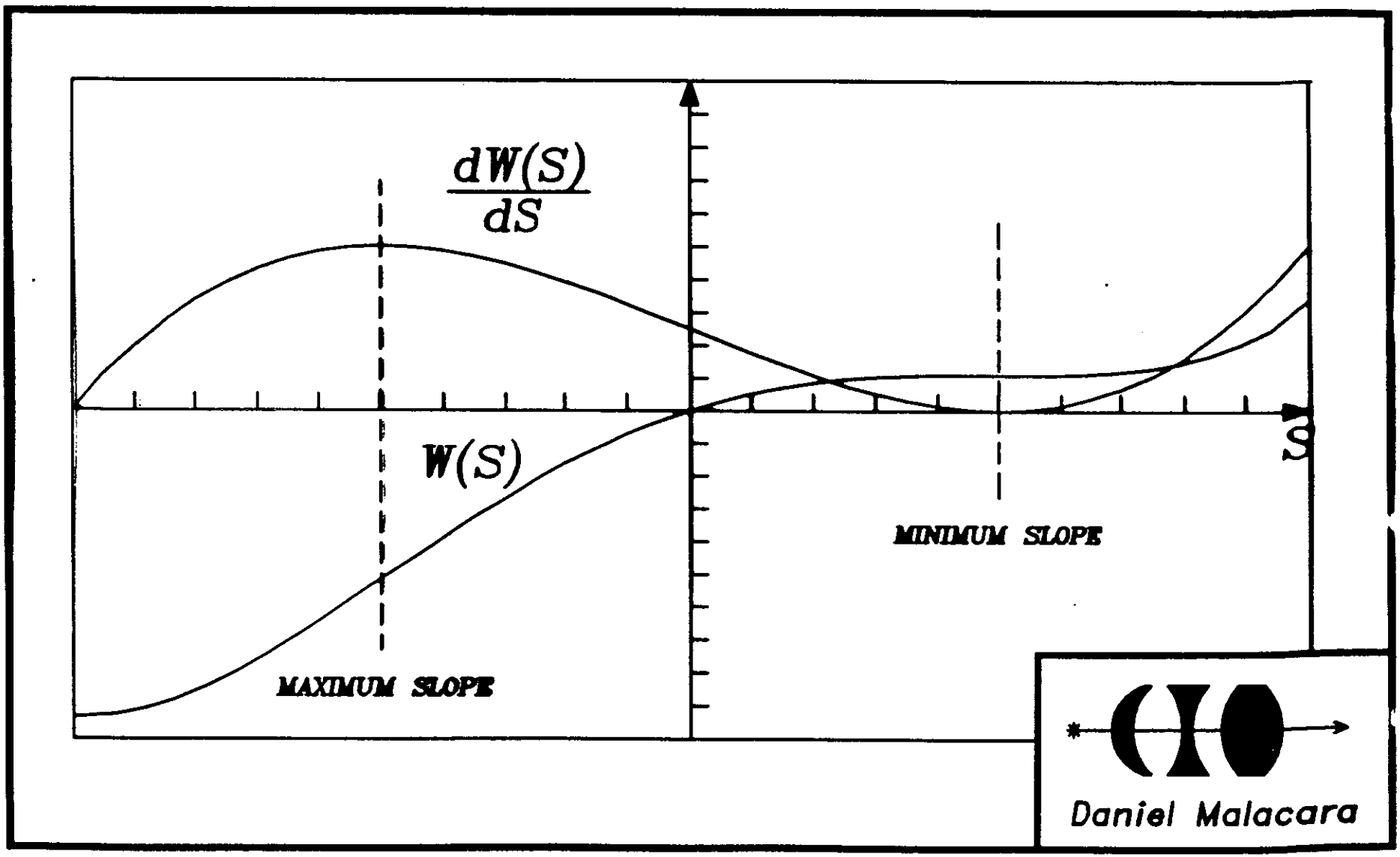
dW(S)
dS
W(S)
S
MAXIMUM SLOPE
MINIMUM SLOPE
Daniel Malacara

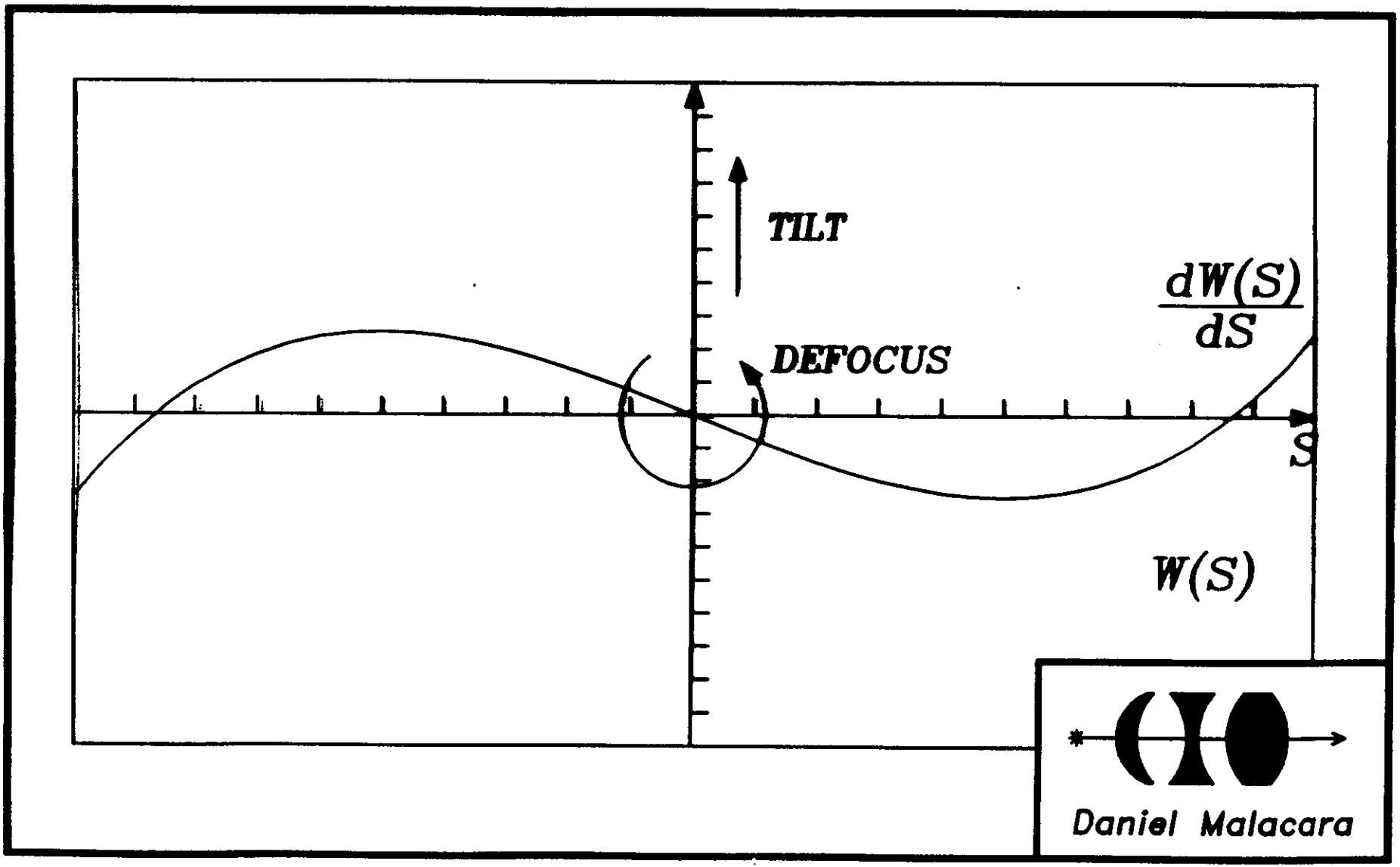
TILT
DEFOCUS
dW(S)
dS
S
W(S)
Daniel Malacara

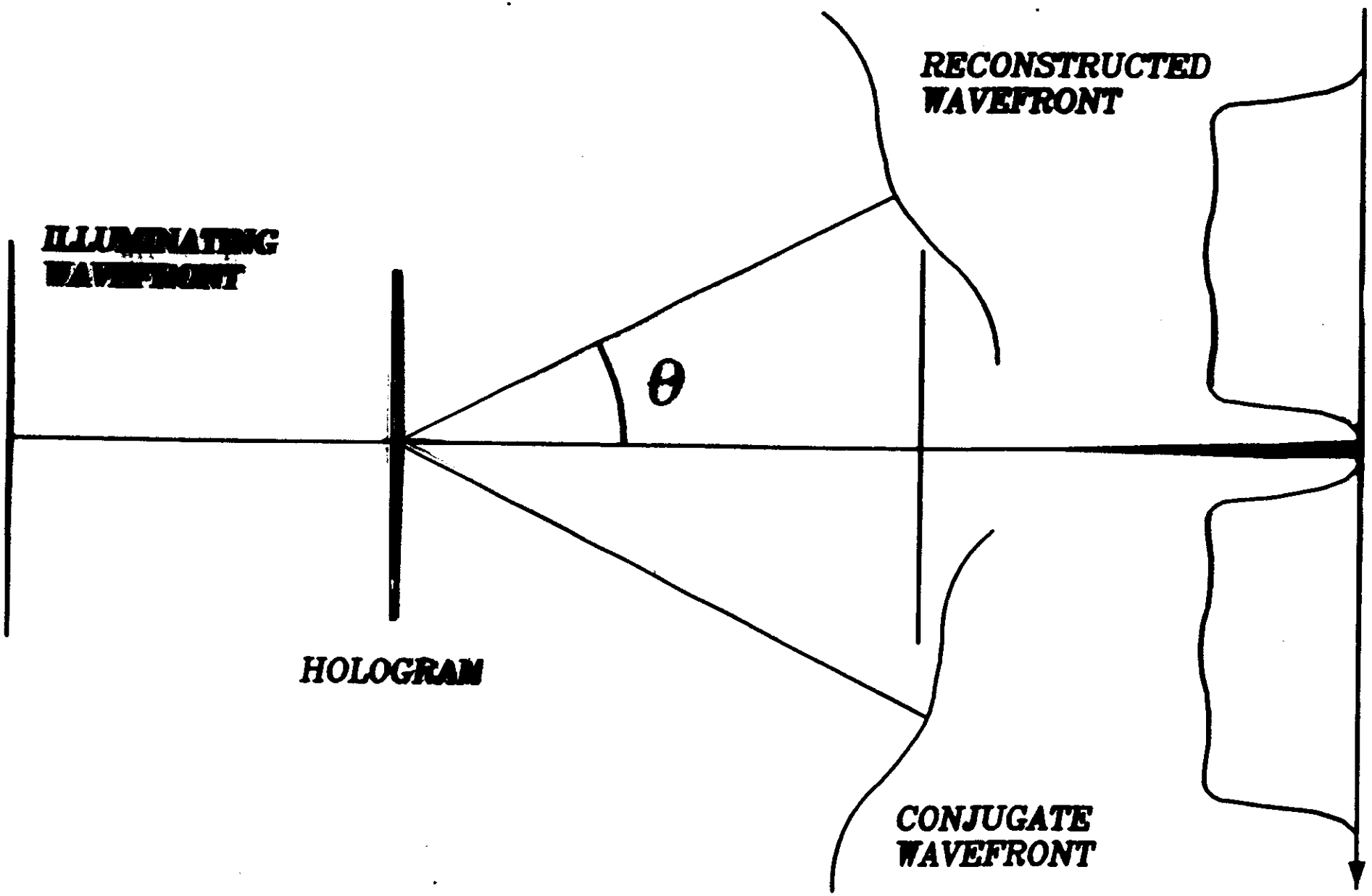
RECONSTRUCTED
WAVEFRONT
ILLUMINATING
WAVEFRONT
θ
HOLOGRAM
CONJUGATE
WAVEFRONT
f

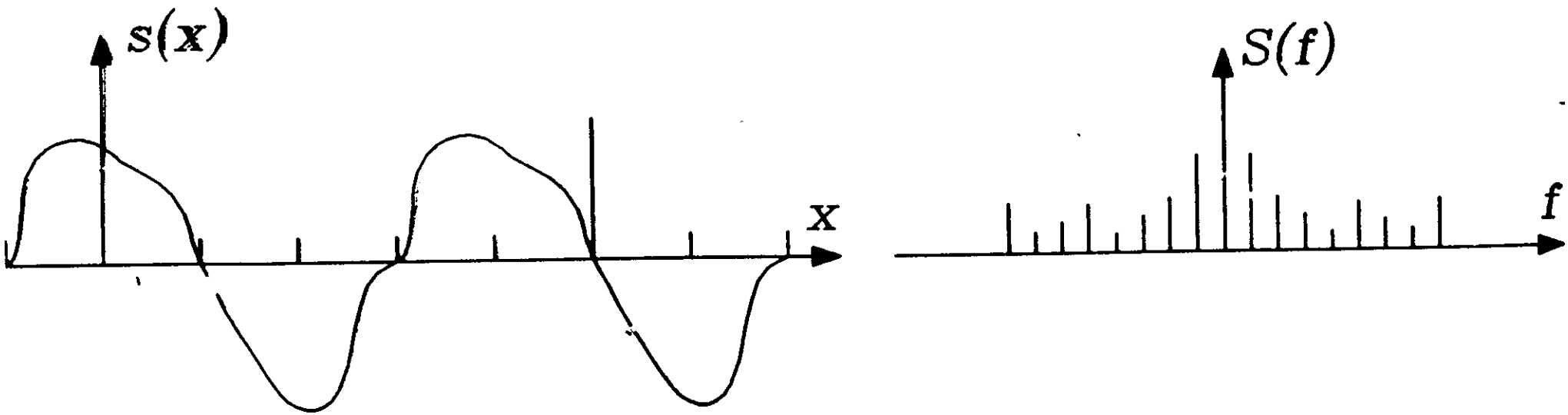
s(x)
x
S(f)
f

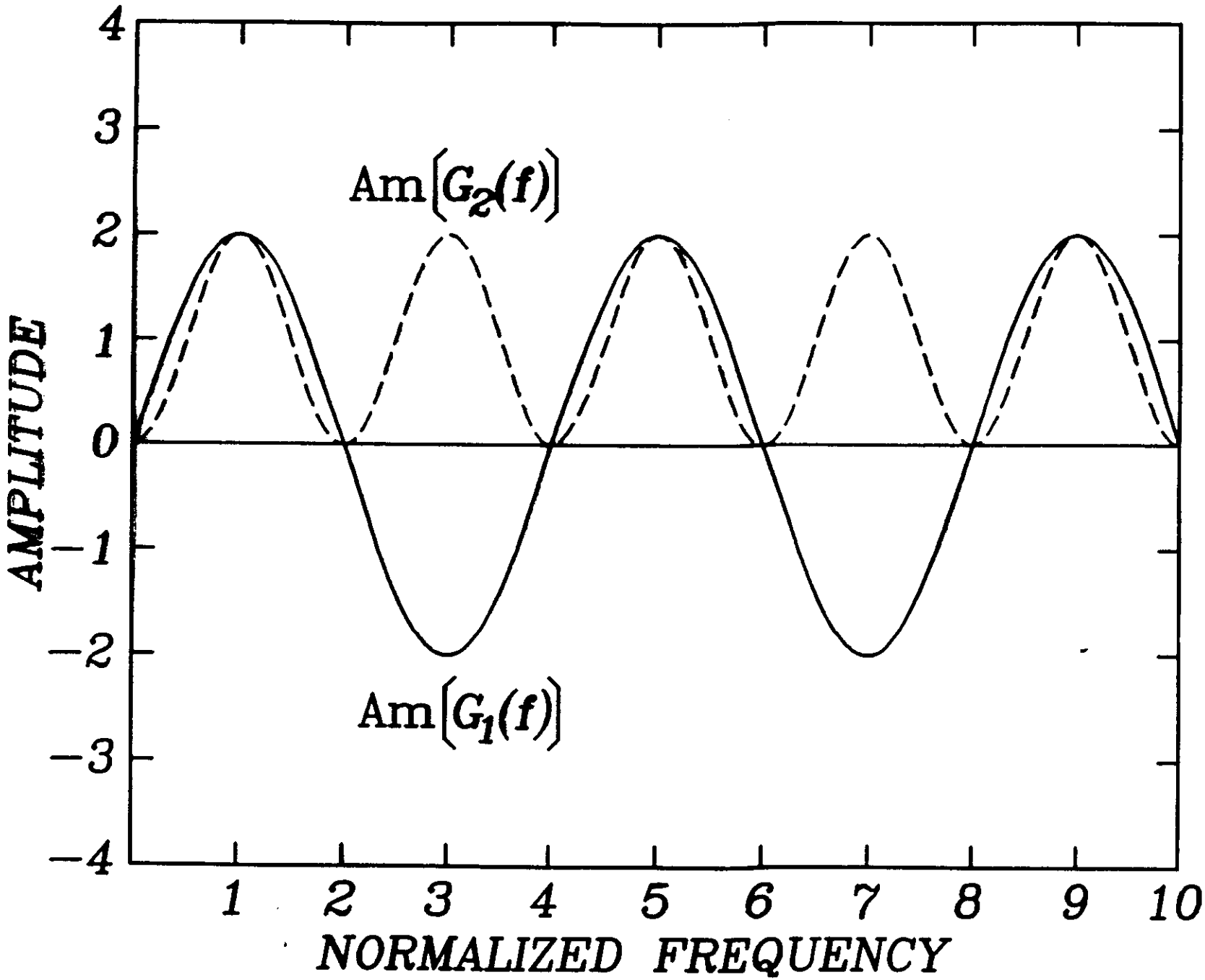
4
3
2
1
0
−1
−2
−3
−4
AMPLITUDE
Am[G2(f)]
Am[G1(f)]
1
2
3
4
5
6
7
8
9
10
NORMALIZED FREQUENCY

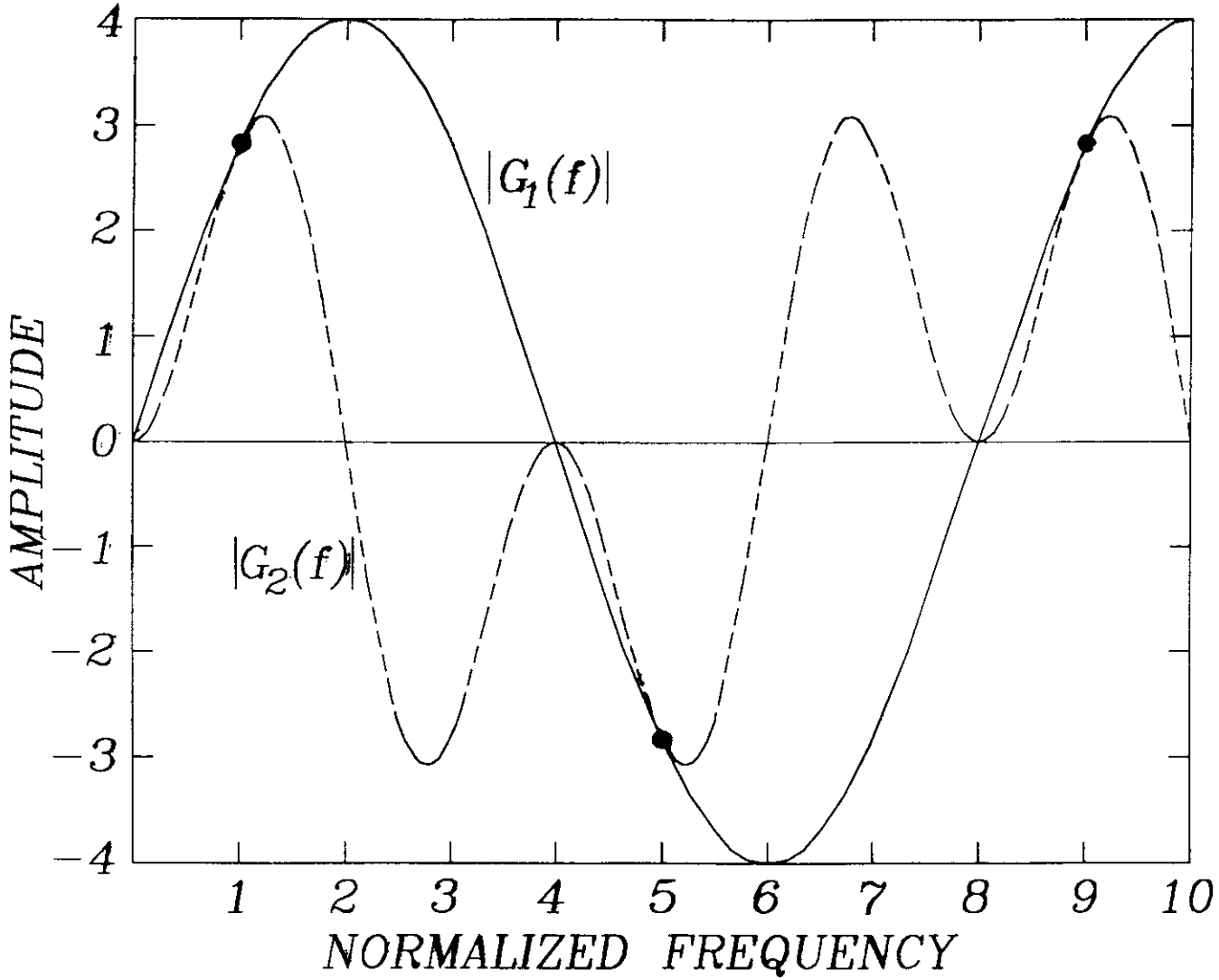

Fourier transforms of sampling reference functions for $\alpha=\pi/4$

AMPLITUDE
0
1
2
3
4
FREQUENCY
f_1
$|G_1(f)|$
$|G_2(f)|$
$|S(f)|$

ERROR δφ
-π
0
π
2π
φ
ψ(fr)
δ
2
1

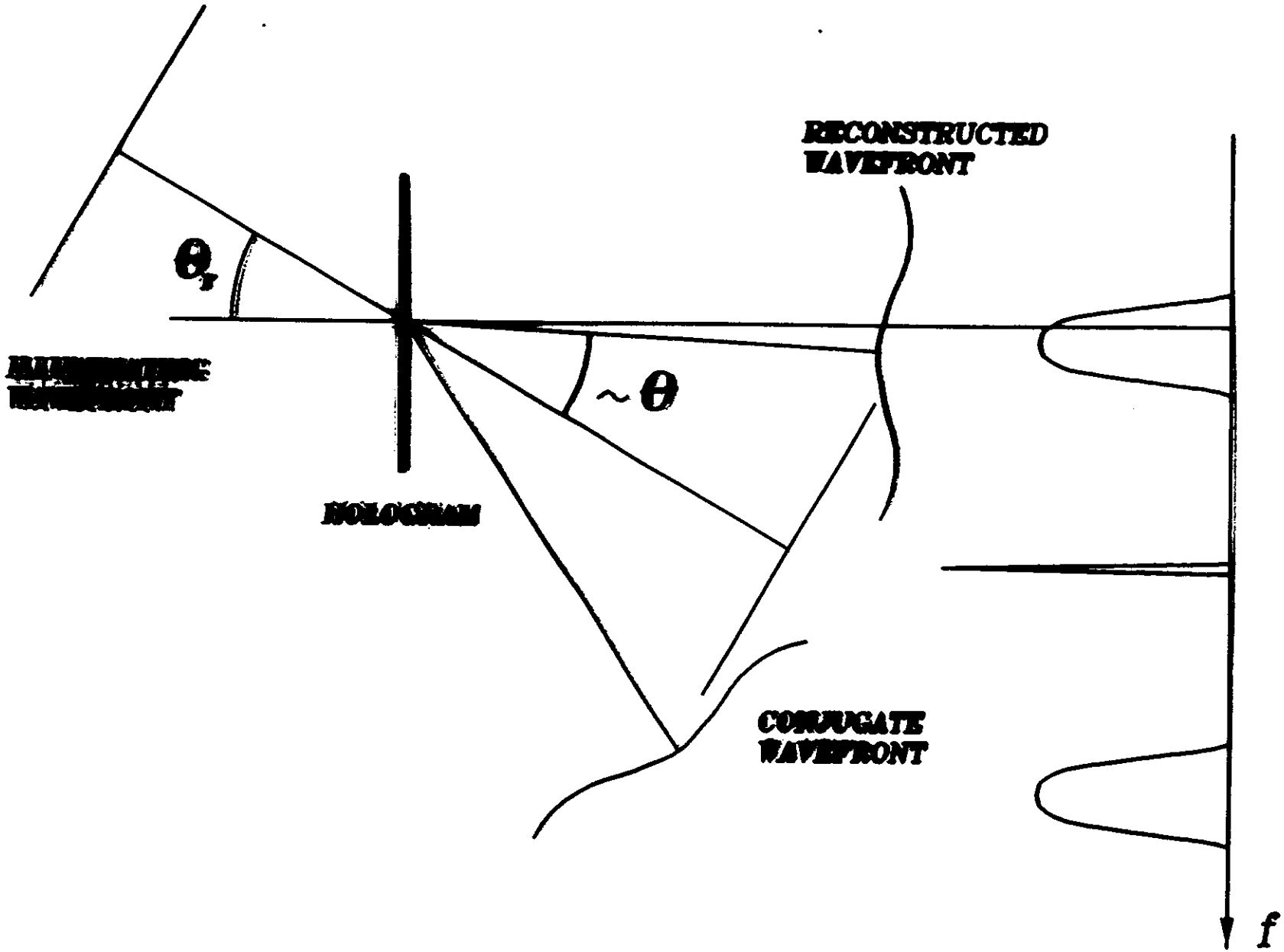
RECONSTRUCTED
WAVEFRONT
θ_r
$\sim\theta$
HOLOGRAM
CONJUGATE
WAVEFRONT
f

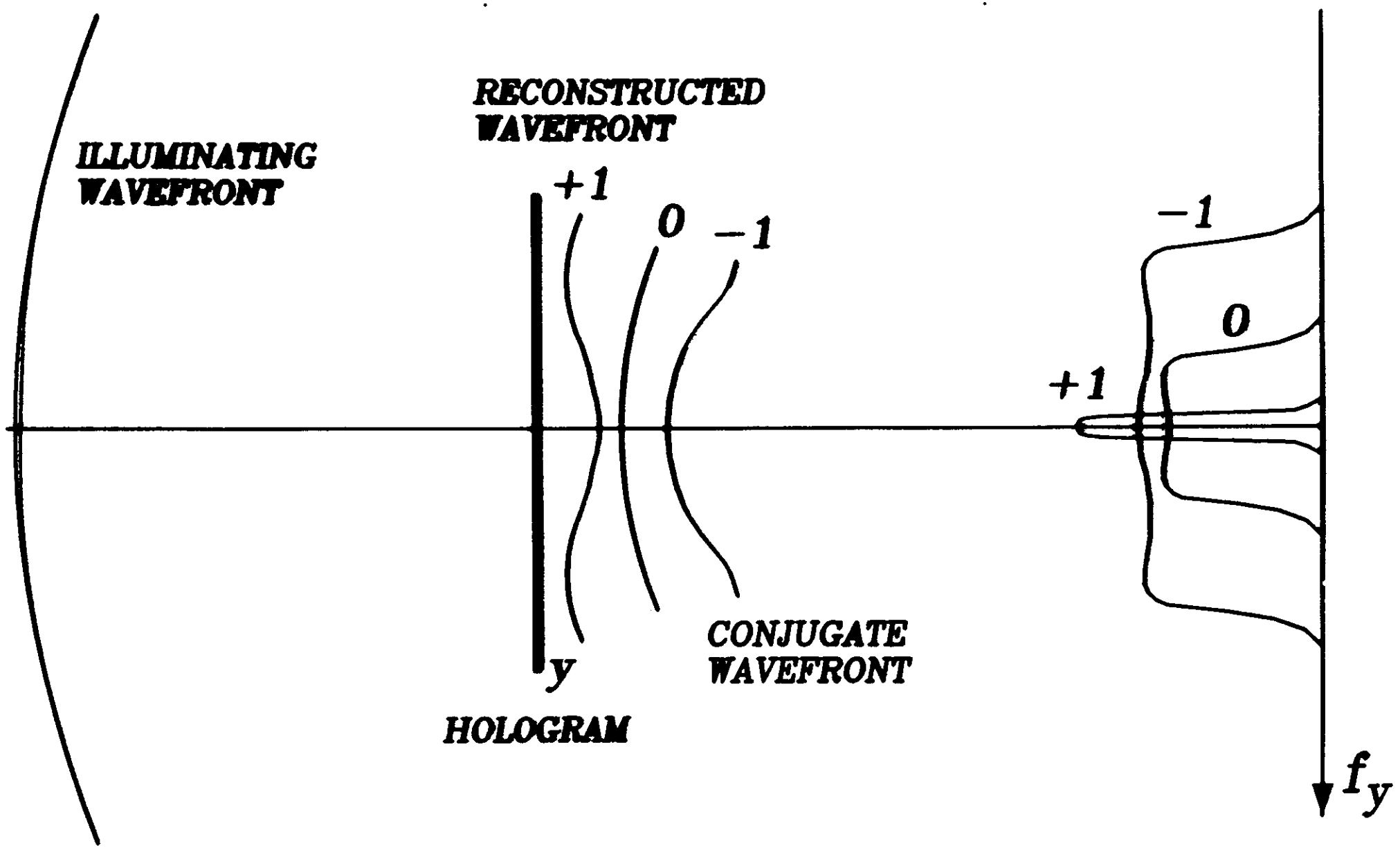
ILLUMINATING
WAVEFRONT
RECONSTRUCTED
WAVEFRONT
+1
0
−1
y
HOLOGRAM
CONJUGATE
WAVEFRONT
−1
0
+1
f_y

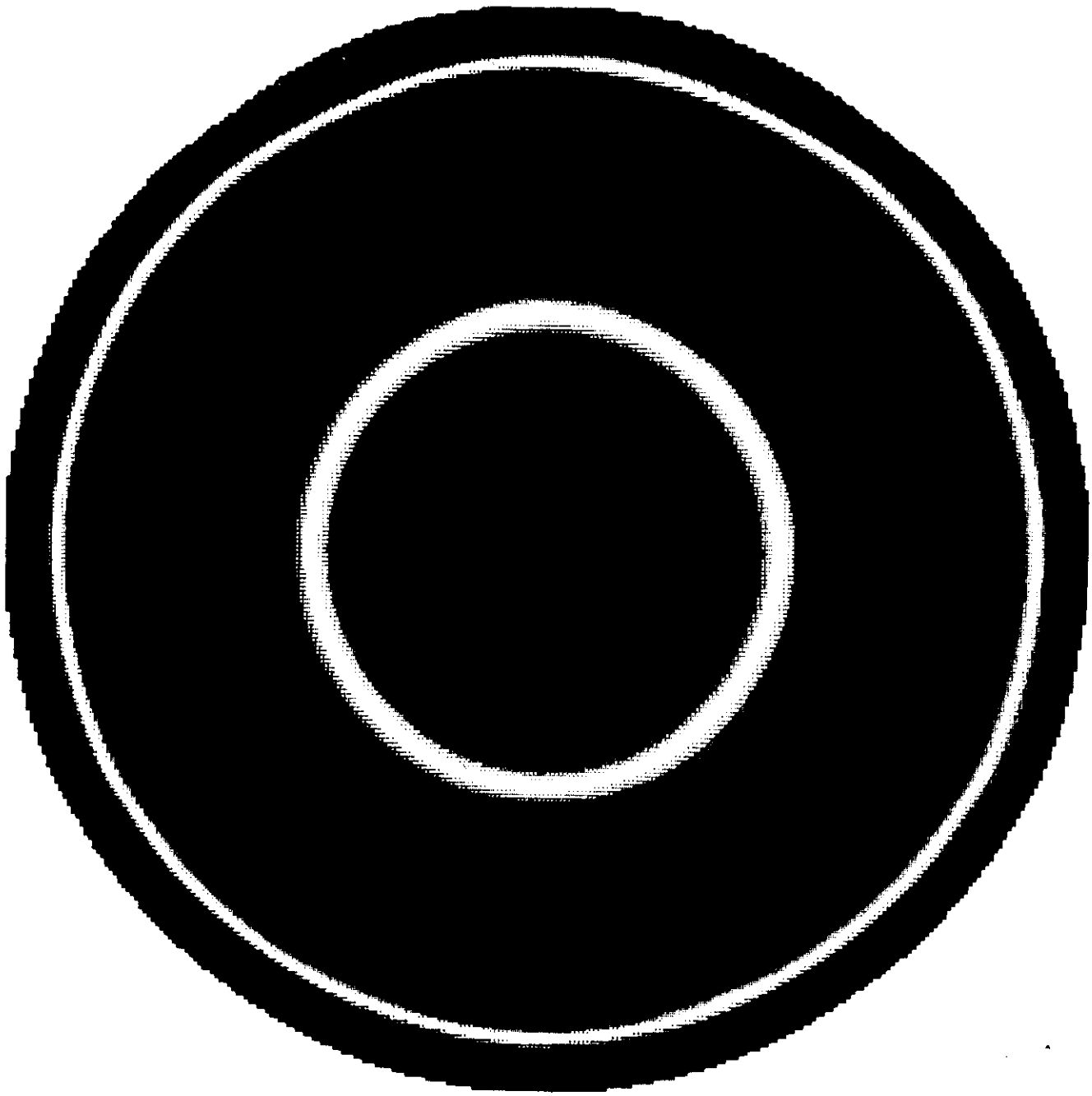

SPHERICAL ABERRATION
BEST FOCUS

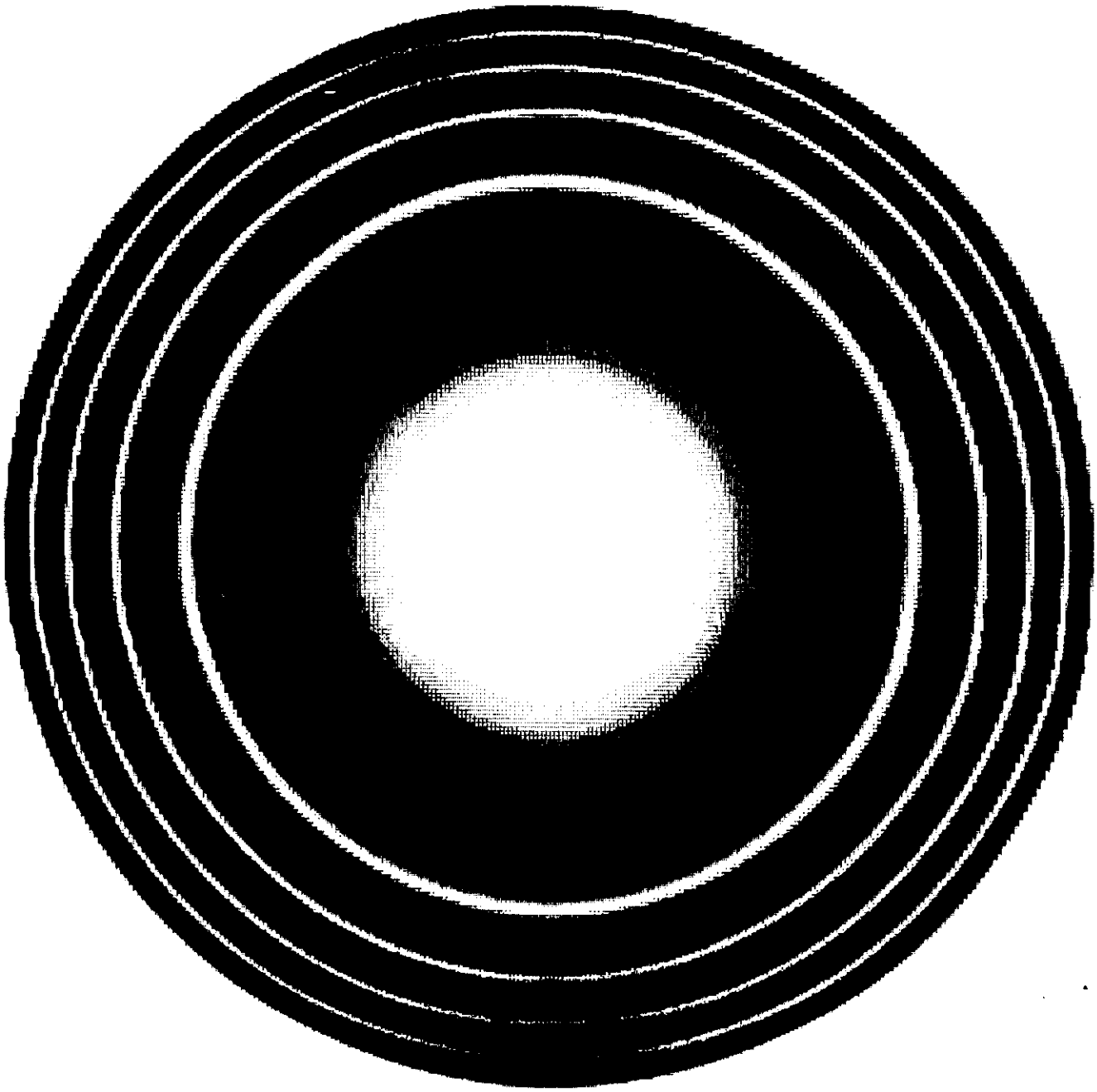

SPHERICAL ABERRATION
PARAXIAL FOCUS

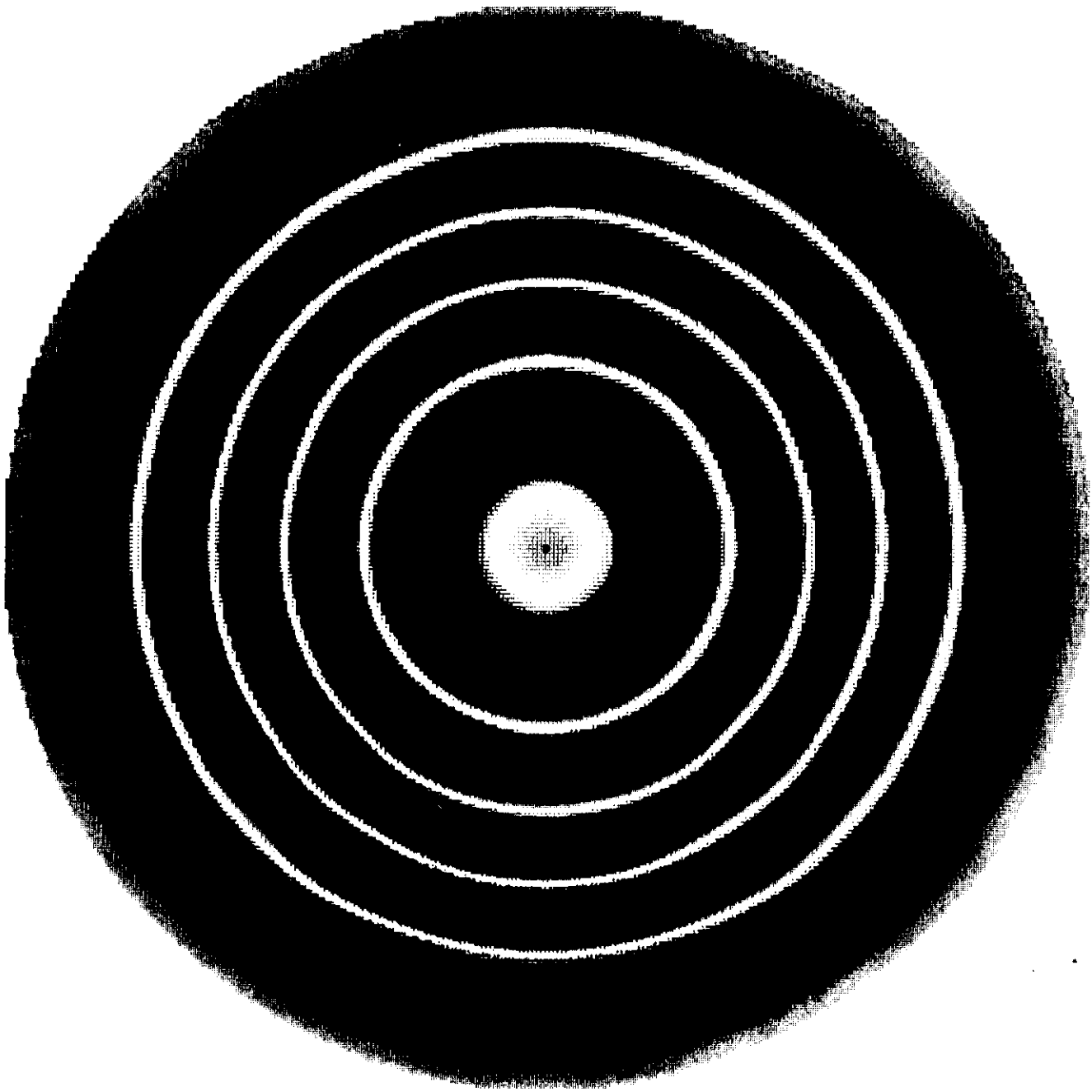

SPHERICAL ABERRATION
MARGINAL FOCUS

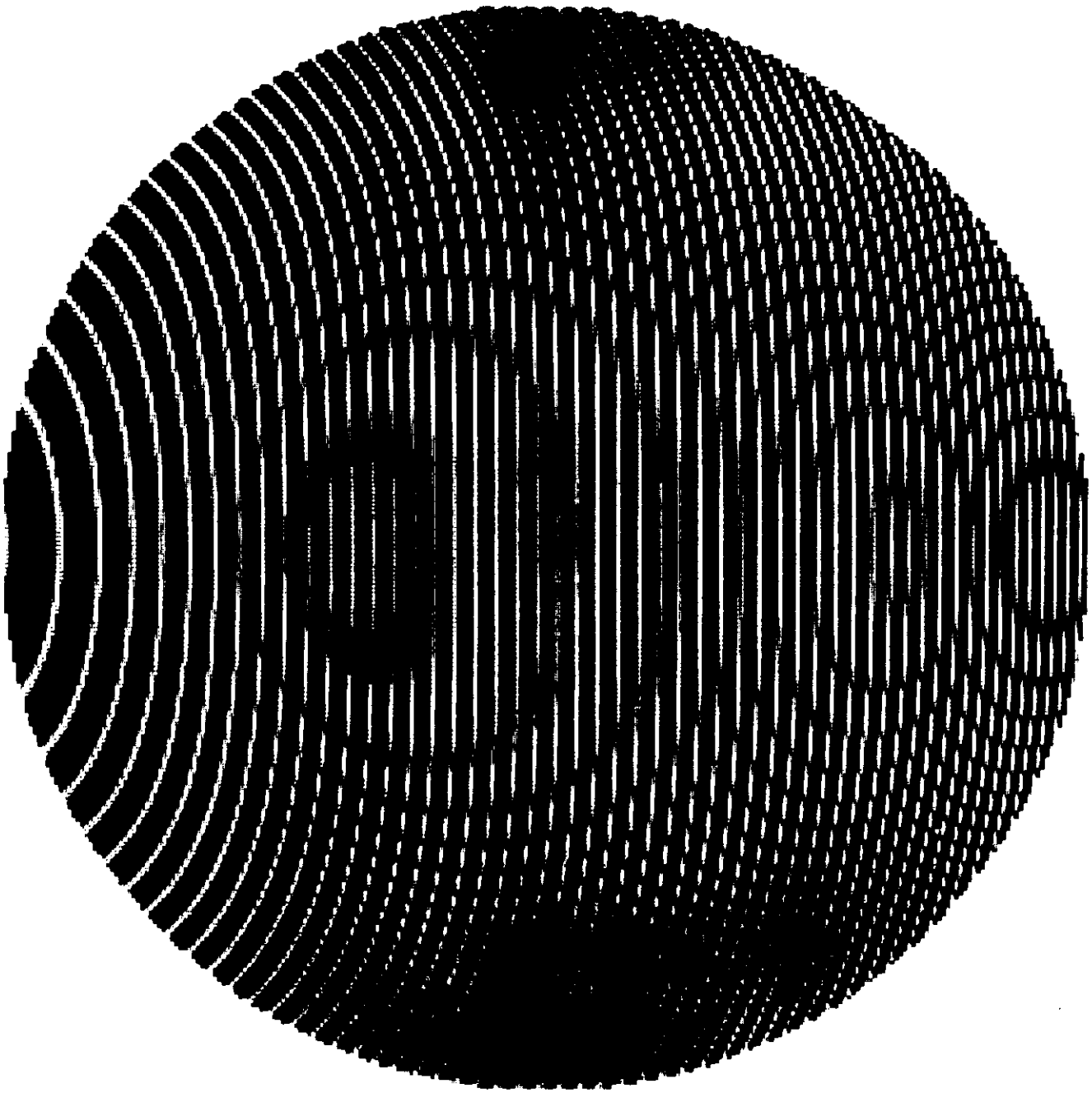

SPHERICAL ABERRATION
PARAXIAL FOCUS
TILT (LINEAR CARRIER)

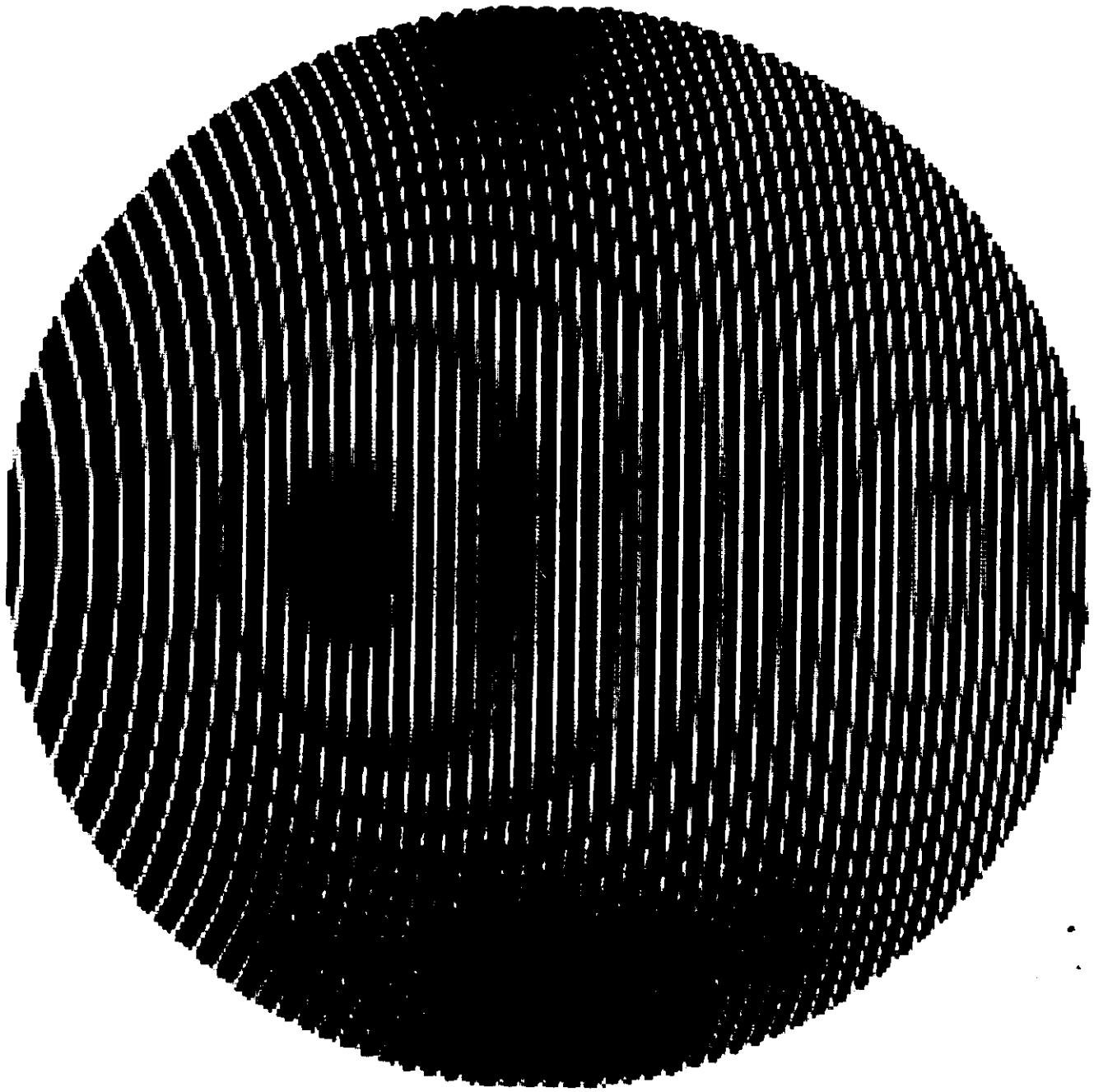

SPHERICAL ABERRATION (–)
PARAXIAL FOCUS
TILT (LINEAR CARRIER)

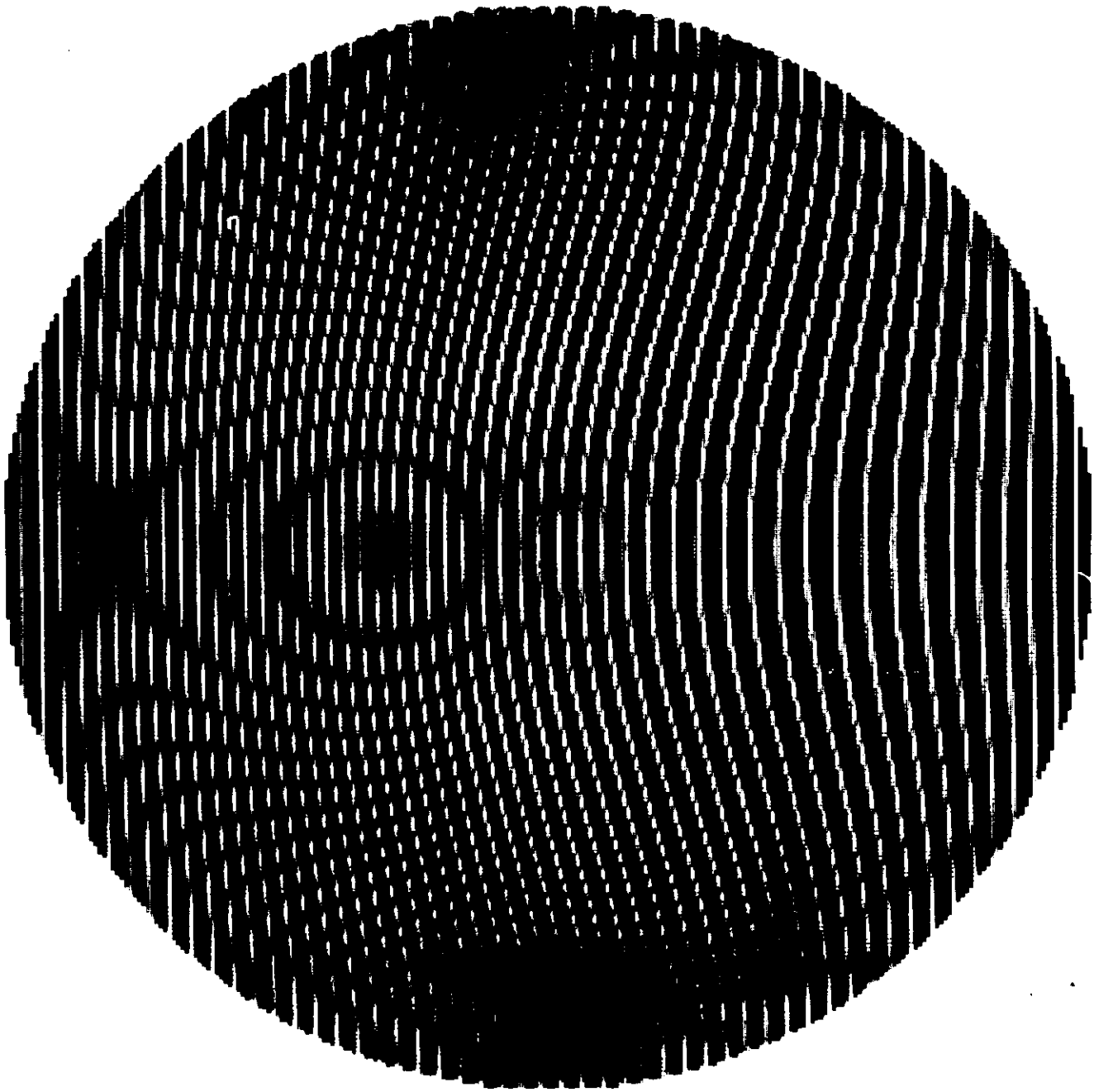

SPHERICAL ABERRATION
MARGINAL FOCUS
TILT (LINEAR CARRIER)

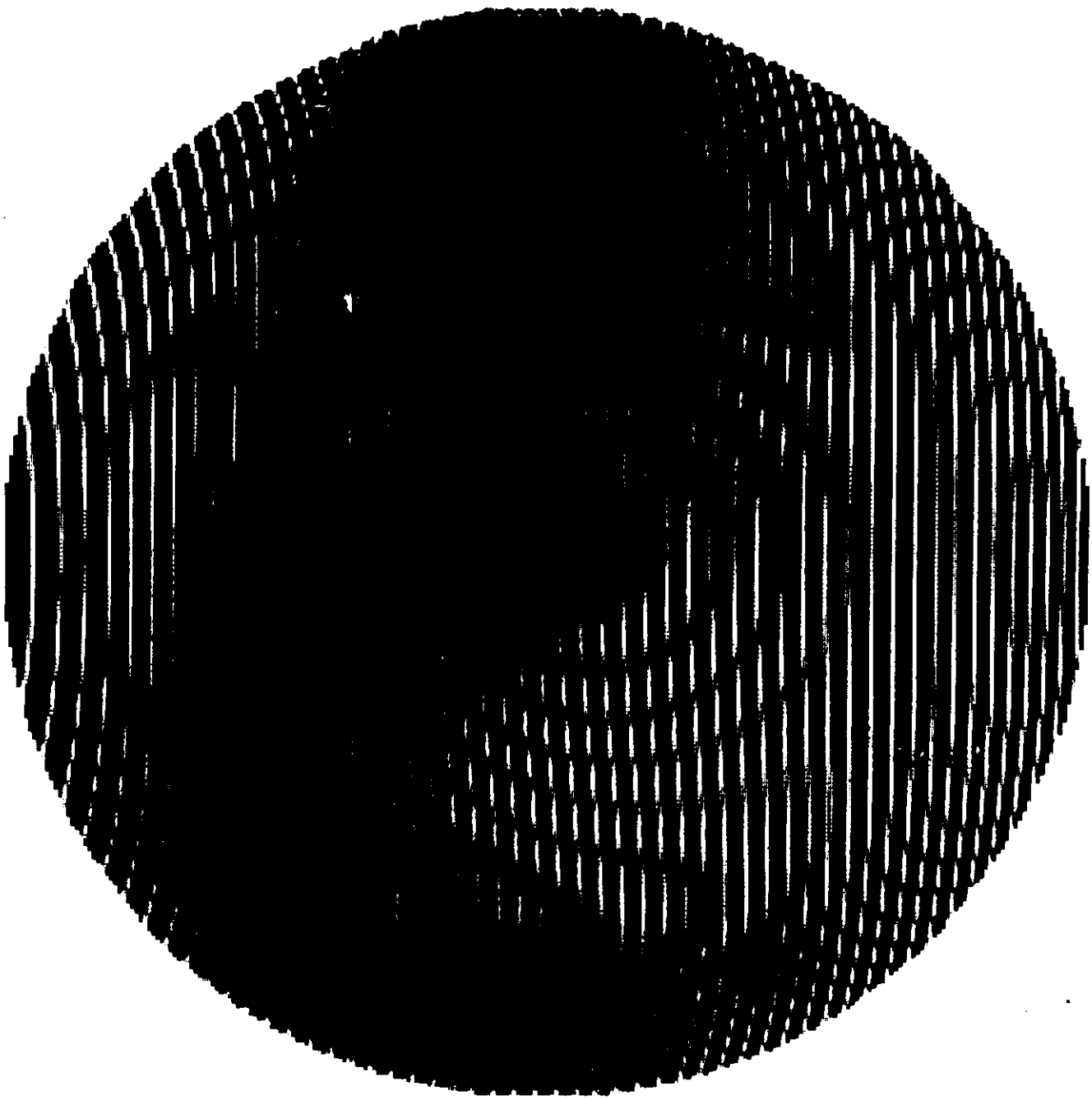

SPHERICAL ABERRATION
BEST FOCUS
TILT (LINEAR CARRIER)

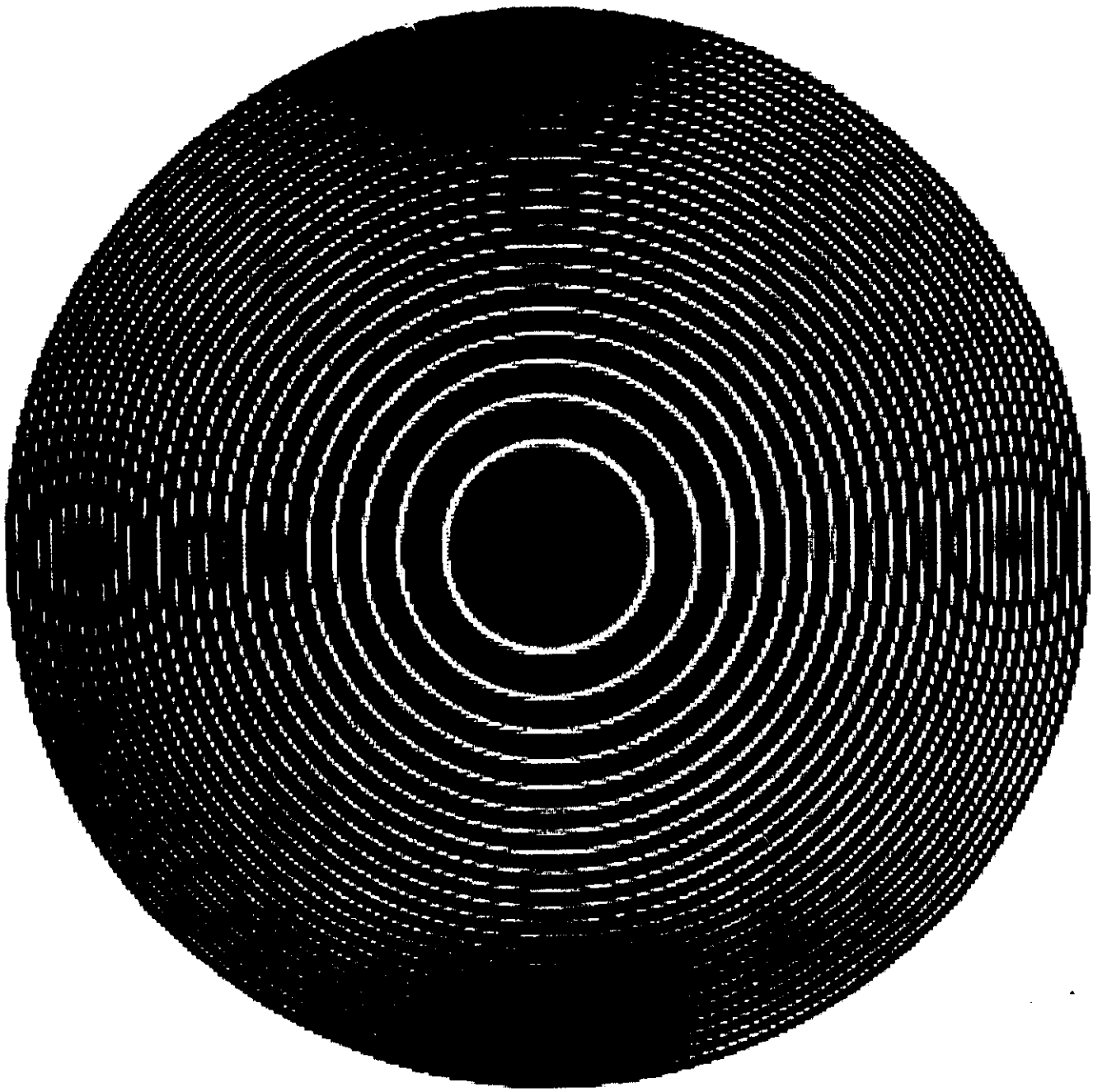

DEFOCUSING

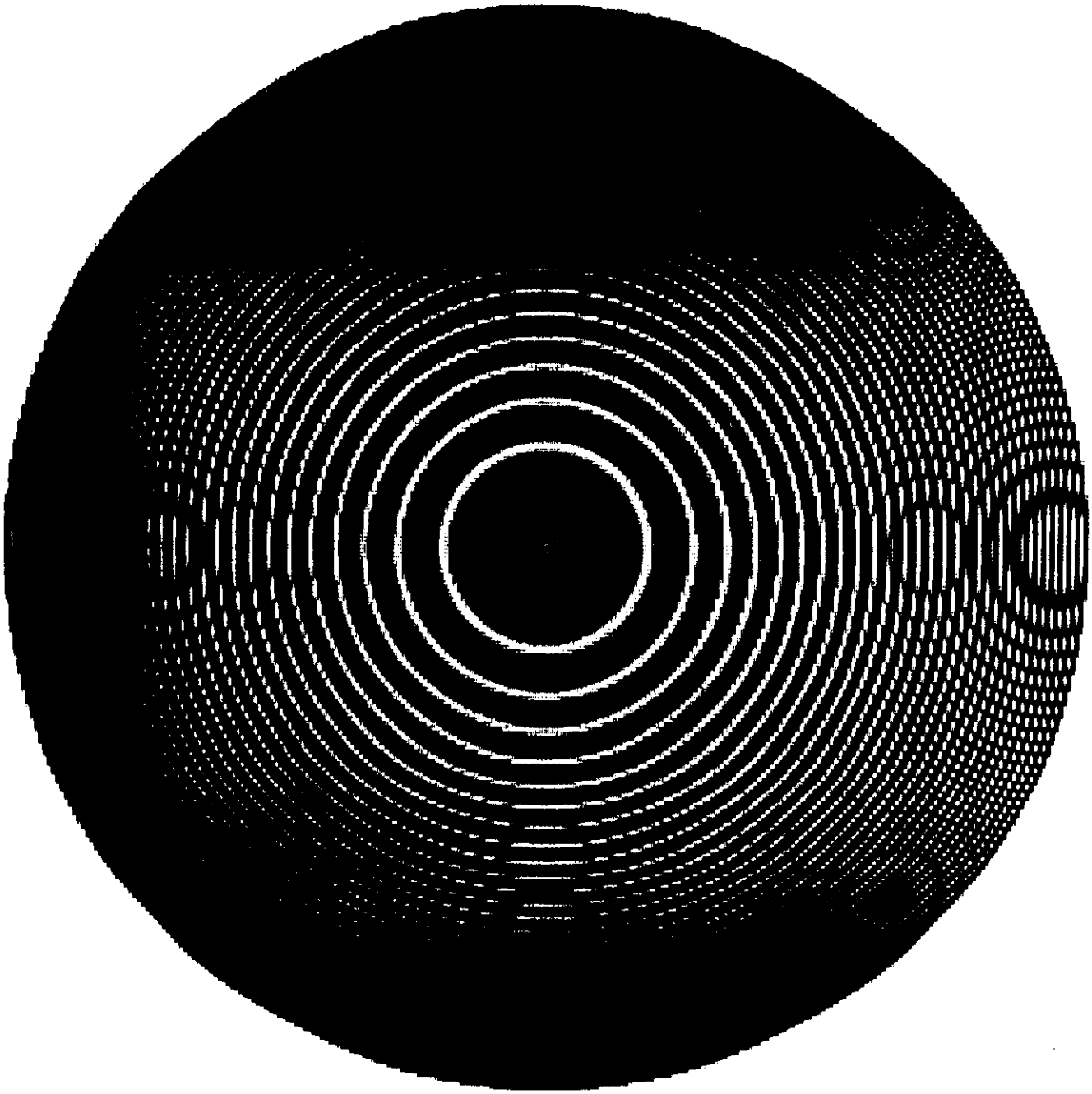

SPHERICAL ABERRATION

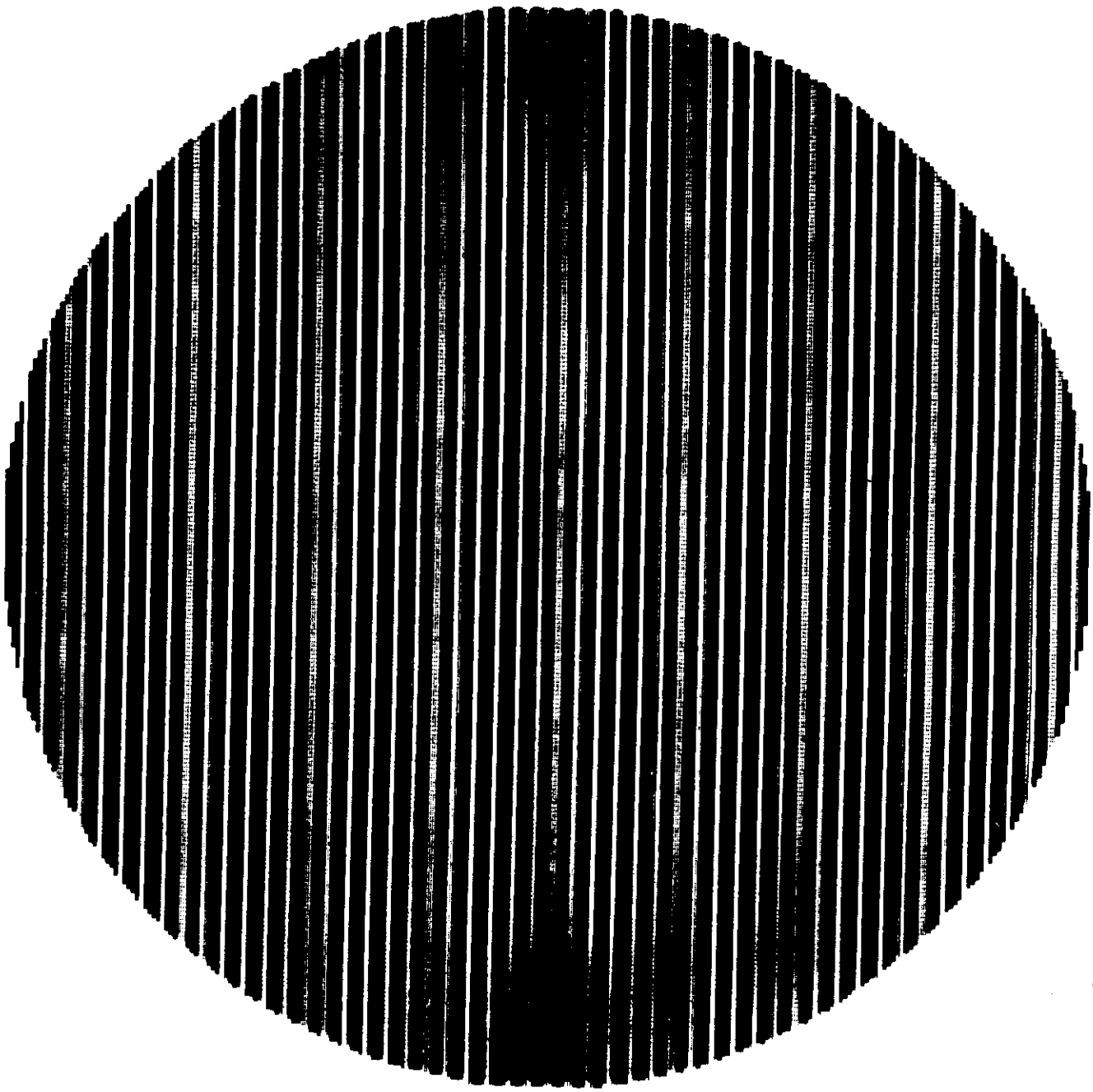

TILT (LINEAR CARRIER)

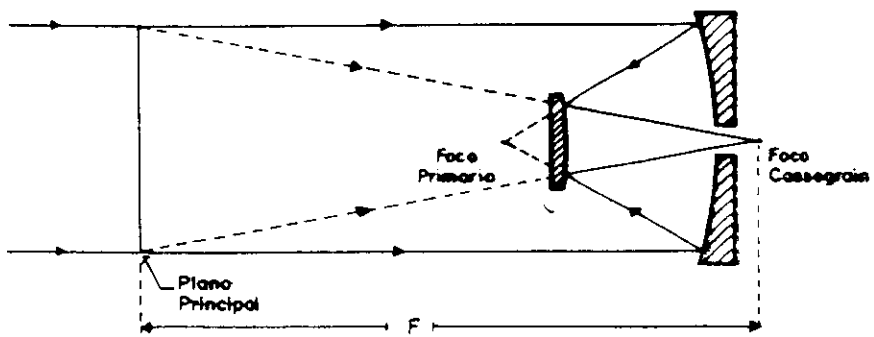
Foco
Primario
Foco
Cassegrain
Plano
Principal
F

(a)

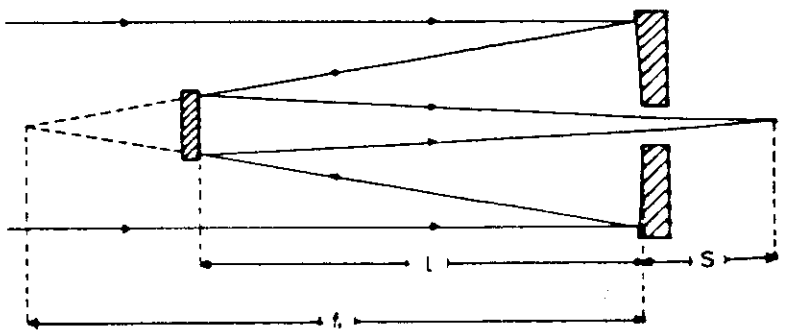
l
S
f

(b)

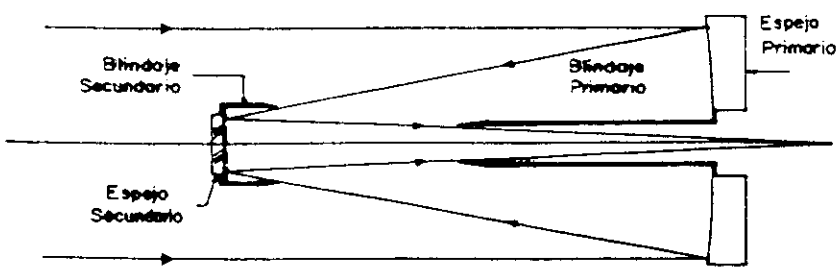
Espejo
Primario
Blindaje
Secundario
Blindaje
Primario
Espejo
Secundario

(c)

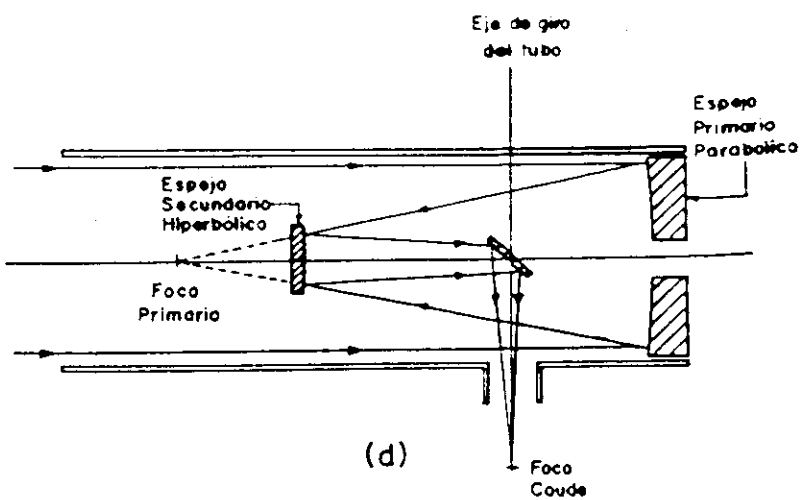
Eje de giro
del tubo
Espejo
Primario
Parabolico
Espejo
Secundario
Hiperbolico
Foco
Primario
Foco
Coude

(d)

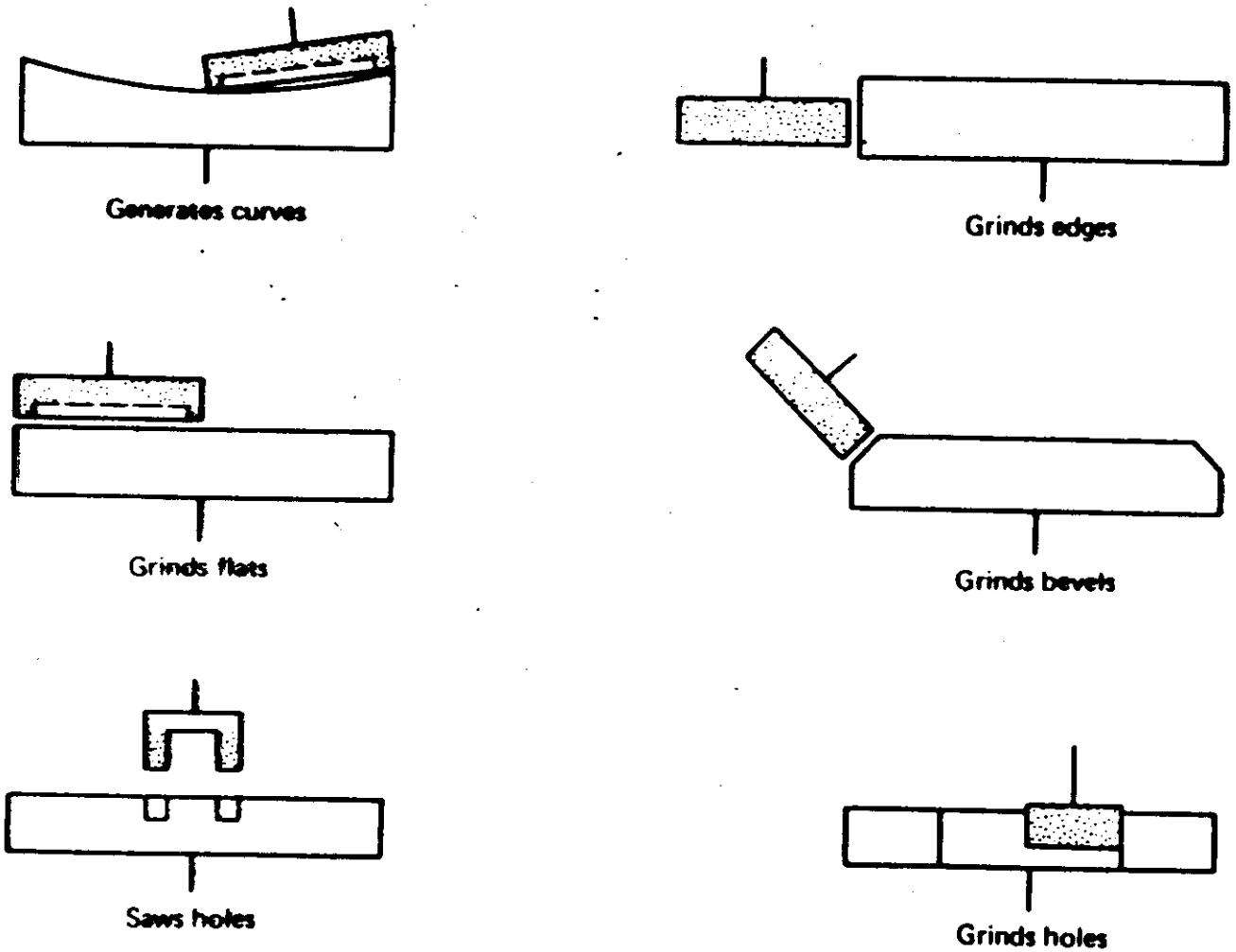

Various operations that can be performed with the Strabaugh Model 7-M generator. Special vacuum chucks are required for drilling and sawing central holes.

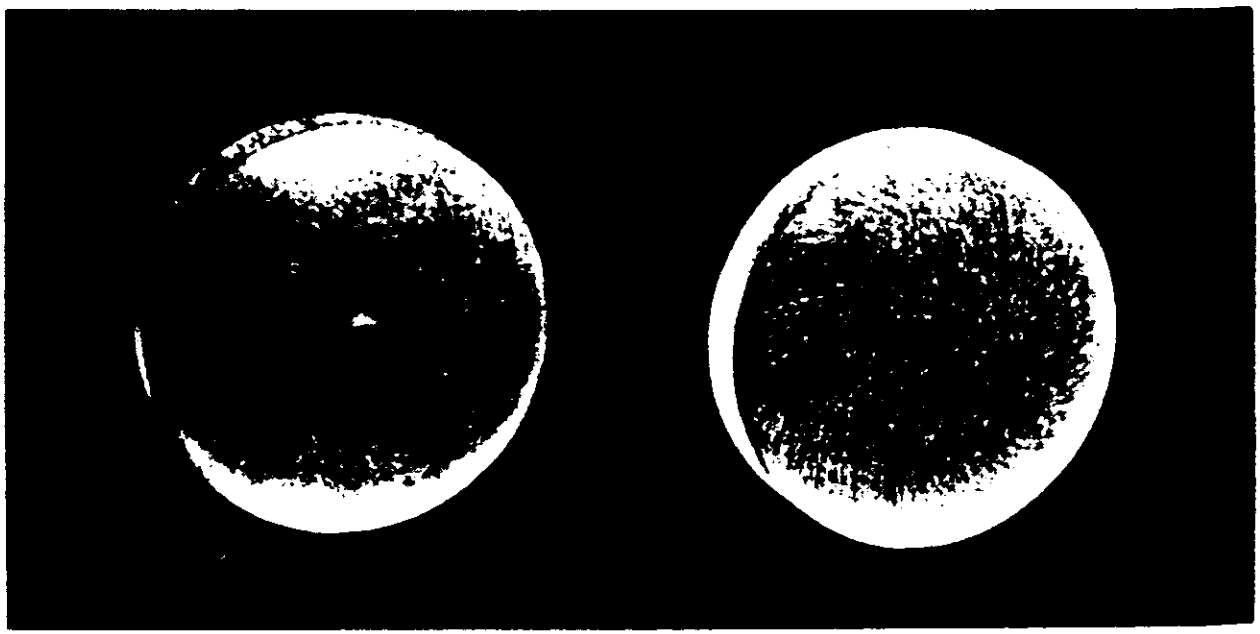

(*a*) (*b*)

Appearance of surfaces roughed on the lens-grinding machine
(*a*) Incorrect (*b*) Correct

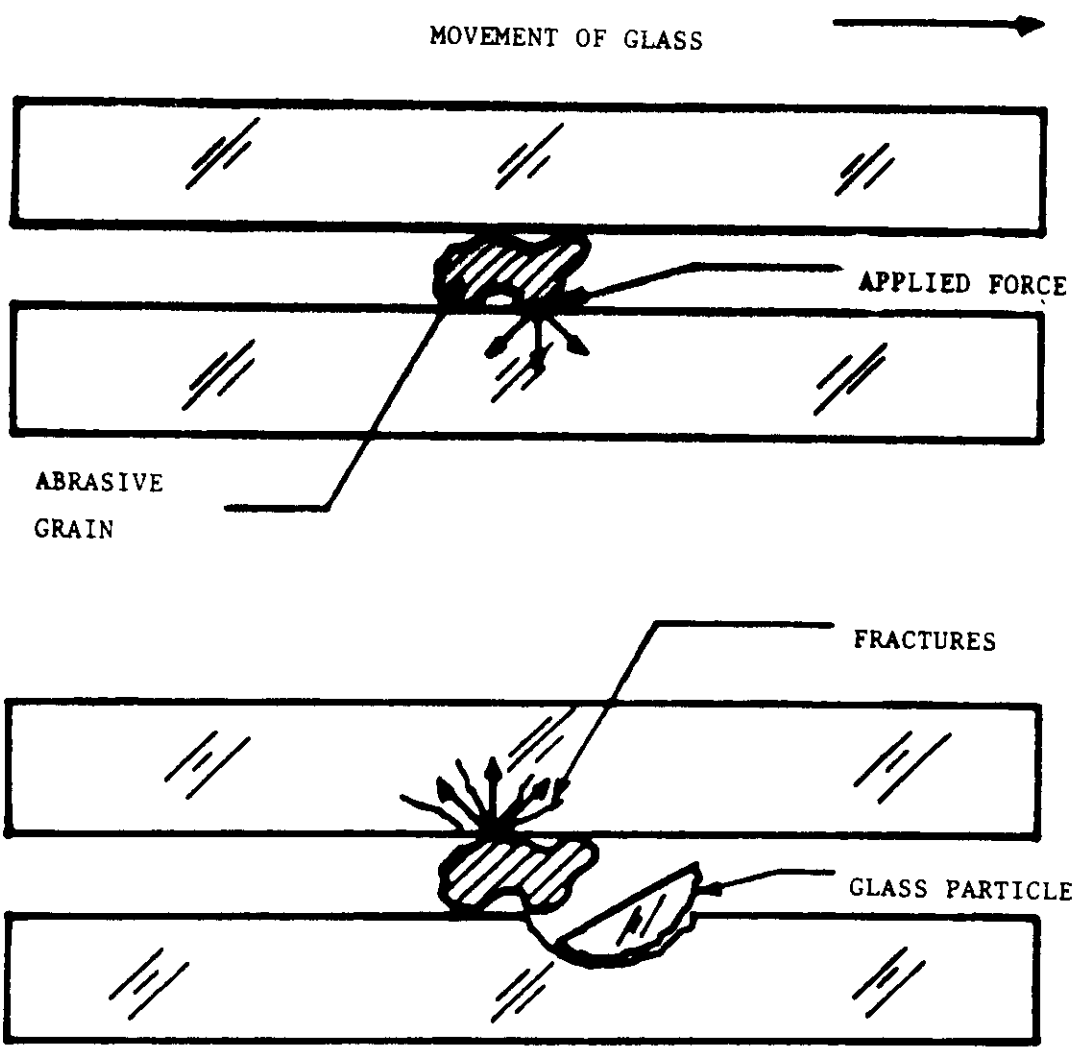
MOVEMENT OF GLASS
APPLIED FORCE
ABRASIVE
GRAIN
FRACTURES
GLASS PARTICLE

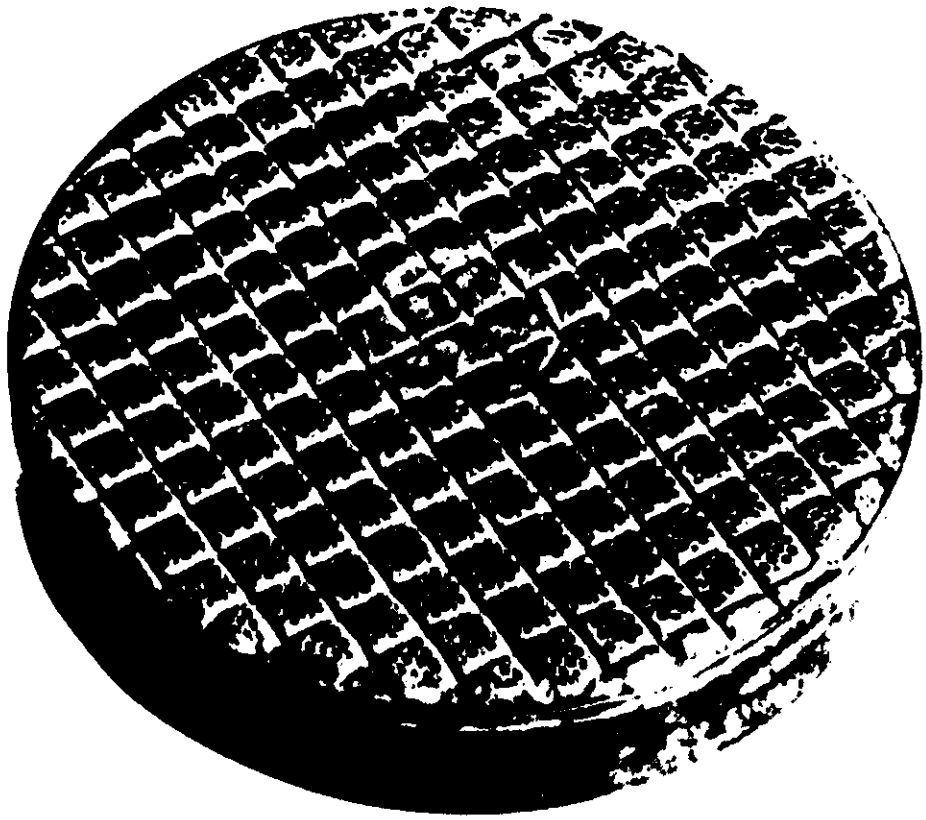

Pitch polisher—reticulated and netted.